To

Jennifer

Mum • Dad

FOOTPRINTS IN THE SAND

'One night a man had a dream. He dreamed he was walking along the beach with the Lord. Across the sky flashed scenes from his life. For each scene he noticed two sets of footprints in the sand. One set belonged to him, the other to the Lord.

'When the last scene of his life flashed before him, he looked back at the footprints in the sand. He noticed that many times along the path of his life there was only one set of footprints. He also noticed it happened at the very lowest and saddest times in his life.

'This really bothered him and he questioned the Lord about it. "Lord, You said that once I decided to follow You, You would walk with me all the way. But, I have noticed that during the most troublesome times in my life, there is only one set of footprints. I do not understand why in the times I needed You most, You would leave me".

'The Lord replied, "My precious, precious child I love you and I would never leave you. During your times of trial and suffering, when you saw only one set of footprints, it was then that I carried you"'.

THE OXIDATIONAL WEAR OF DIESEL ENGINE MATERIALS

BY

CLIVE BRUCE ALLEN, B.Sc.

A thesis submitted for the degree of

DOCTOR OF PHILOSOPHY

THE UNIVERSITY OF ASTON IN BIRMINGHAM

MAY 1982

THE OXIDATIONAL WEAR OF DIESEL ENGINE MATERIALS

By CLIVE BRUCE ALLEN

A thesis submitted for the degree of

DOCTOR OF PHILOSOPHY

1982

Summary

The valves and valve seats in the exhaust of the diesel engine operate in hostile conditions at temperatures of up to 700°C. A material combination commonly used is that of 21 - 4N (valve) and Brico 65 (valve seat). The present work isolates the fundamental wear mechanisms of this material couple, under various conditions of load, speed and elevated temperatures. Sliding experiments were carried out on a wear machine of pin-on-disc geometry, in which friction and wear were continuously monitored during each test. The wear debris, and the worn pin (Brico 65) and disc (21 - 4N) specimens were examined using numerous physical methods of analyses (X-ray Diffraction, Scanning Electron Microscopy etc.).

Three wear mechanisms were identified, namely, (1) Oxidation and (2) Transfer followed by Abrasion. At medium temperatures and heavy loads the mechanisms of transfer during 'running-in', followed by abrasion during the equilibrium wear regime were prevalent. The abrasive wear rates appear to be dependent on the amount of silicon which is transferred from the pin material to the disc. For other conditions of sliding the predominant wear mechanism is oxidation.

Heat flow analysis shows that there is significant correlation between the bulk surface temperature, the contact temperature of the sliding members and the wear rate. Activation energy (Q_p) values deduced from the wear and heat flow results suggest that in the case of tribo-oxidation Q_p is much lower in comparison to static oxidation.

Diesel Engine Materials/Friction/Wear/Oxidation

ACKNOWLEDGEMENTS

I am indebted to my supervisor, Dr. T.F.J. Quinn (Physics Department, Aston University) for his help and continued encouragement during the work contained in this thesis. Thanks are due to Dr. M.H. Wharton (Perkins Engines Limited) for the provision of materials and his interest in the research work. I am extremely grateful to Mr. J.L. Sullivan (Physics Department, Aston University) for his thorough reading and constructive criticisms of the thesis, whilst in manuscript form. Thanks are also due to my colleague, Mr S.S. Athwal (Physics Department, Aston University), for the numerous discussions we had during the course of this work.

I acknowledge the staff of the Physics Workshop, in particular, Mr. Howard Arrowsmith, for his considerable practical assistance in the commissioning of the wear machine. Gratitude is also extended to the Metallurgy and Production Engineering Departments for the liberal use of facilities. Finally, I would like to thank Professor S.E. Hunt, Head of the Department of Physics, in whose laboratories, the majority of the work was carried out.

Financial assistance for the project was jointly funded by the Science Research Council and by Perkins Engines Limited.

I extend sympathy and thanks to my fiancee, for the many sacrifices made, which enabled the completion of this thesis possible.

CONTENTS

FIGURES

TABLES

CHAPTER 1

INTRODUCTION

1.1 Technical Background to Problem

Valve sinkage in the exhaust, and to a lesser extent in the inlet, of the typical diesel engine is a problem which the co-operating body (Perkins Engines Company) has been studying for some time (1).

Under conditions of high temperatures and a hostile environment, found particularly in the exhaust gases, the material commonly used for the valve seat (Brico 65) is found to wear preferentially to the valve material (21 - 4N). Brico 65 is a ferritic steel, containing mainly iron and chromium with a significant amount of silicon. In contrast, 21 - 4N is an austenitic steel containing mainly iron, chromium, manganese and nickel (see Section 3.5).

The exhaust gases will contain CO_2, NO_2, CO and water vapour, hence the wear process is most likely to be oxidational. There are added complexities in the form of trace elements from the fuel and lubricating oil such as sulphur, leading to the formation of sulphides etc.

In previous analyses there have been discrepancies between metallographic indications (2) of high temperatures and theoretical predictions (3) of lower temperatures at which valve seat wear occurs. This is a situation where there is a gap in the knowledge of wear at elevated temperatures. These valves operate at temperatures of up to 700°C.

It is hoped that the present work will successfully

bridge the gap in the knowledge of the wear behaviour of these valve and valve seat materials at elevated temperatures.

1.2. Unlubricated Wear

In any practical wearing situation (eg valve seat wear) the understanding and subsequent identification of the mechanisms which lead to wear is of fundamental importance.

Wear can generally be defined as the removal of material from rubbing surfaces. However, wear is a complex phenomena, consisting of many diverse mechanisms. The main variables which affect the magnitude and type of wear which occurs are load, speed, temperature and material properties such as hardness and composition (4). In addition, structural changes in the subsurface of the material due to the effect of load, speed and temperature; and the interaction of the rubbing surfaces with the environment add further complications (5, 6).

The unlubricated wear rates of common engineering materials range over about 5 orders of magnitude (7), whereas the corresponding friction coefficients are within a factor of 10 (8). Archard (7) offers the explanation that all mating asperities are involved in the friction process while only a fraction (K) are involved in the wear process. For clean metal surfaces $.01 < K < .1$ and for surfaces protected by oxide or lubricant films $10^{-7} < K < 10^{-6}$ (8).

1.3. Classifications and Mechanisms of Wear

The major classifications of wear were first proposed by two groups of workers in the early 1950's, namely, Archard and

Hurst (9) and Burwell and Strang (10).

Archard and Hurst proposed that wear could be classified into two main categories, namely, "mild and severe wear". Mild wear is characterised by small debris particles size with linear dimensions from 0.01 to 1.0 μm, smooth wear surfaces and high contact resistance. In contrast, severe wear is characterised by large metallic debris particles of dimensions from 10 to 100 μm, occasionally increasing to 1 mm. In the latter, rubbing caused roughening and the surfaces were low in contact resistance (9).

Burwell and Strang (10) and Burwell (11) classified wear in terms of the mechanisms giving rise to material removal, namely, (1) Adhesion, (2) Corrosion, (3) Surface Fatigue, (4) Fretting, (5) Abrasion and (6) Erosion.

1.3.1. Adhesive Wear

When strong adhesion (8,12) occurs between mating asperities of two sliding bodies, wear by adhesion is believed to occur. The subsequent shearing and fracture in and around the contact regions can lead either to the formation of loose wear particles or transferred fragments to one of the sliding members.

In general, adhesion can be regarded as a severe wear mechanism (9,13).

1.3.2. Corrosive Wear

In a gaseous or liquid environment the products of corrosion form a film on the interacting surfaces of the sliding members, which may appreciably reduce the corrosion rate. The film may be partially or wholly removed due to the action of sliding.

Rupture of the film results in the exposure of virgin metal, allowing further corrosion. It is the mechanism of repeated removal and formation of the film in this way which constitutes corrosive wear.

If the corrosion products result in the development of a protective film, in a manner similar to protective oxide film formation; then the resulting wear surfaces are smooth, of high contact resistance and the wear particles are of small dimensions. Clearly, all the symptoms of Archard & Hurst's mild wear classification are present and corrosion (in this case) is a mechanism giving rise to mild wear.

In some cases corrosion gives rise to no surface protection and rapid loss of material. The contact resistance is high but the wear surfaces may be roughened or smoothed and the wear debris is larger in dimensions than in the former case. This does not completely come under the original classifications of mild or severe wear. However, Quinn (13) maintained that the problem can be reconciled by classing this form of corrosion as severe wear.

1.3.3. Surface Fatigue

Wear by surface fatigue occurs when an element of a surface under rolling contact is repeatedly stressed, due to cyclic loading. The stresses induced in the substrate (found to be greater than at the surface) as a result lead to the nucleation and subsequent propagation of subsurface cracks to the surface leading to large scale surface damage and pitting (11). The useful life of the rolling mechanism is terminated after pitting occurs (11). Large scale damage commonly found at the surfaces of roller bearings, in the presence of a lubricant, is generally considered to be the result

of surface fatigue. Under conditions where the surface damage is heavy, surface fatigue is a mechanism leading to severe wear.

Under mild wear conditions, for example, protective oxides developed on the surfaces of a continuous sliding pin-on-disc system which become detached as oxide wear particles could be as a result of a fatigue mechanism.

Mild or severe wear could therefore be as a result of a fatigue mechanism.

1.3.4. Fretting Wear

Fretting wear occurs when there is relative tangential displacement between a pair of tightly fitted surfaces, in the form of low-slip amplitude oscillations. Under these conditions of reciprocating sliding, the oxide wear particles become trapped between the sliding surfaces, thereby inducing severe stresses within the constrained geometries of the components. In addition, the oxide particles can act as a third body cutting agent (12) producing abrasion of the surfaces or may form a protective surface layer (14).

1.3.5. Abrasive Wear

This form of wear occurs when a rough hard surface, or a soft surface containing hard particles, slides on a softer surface, and ploughs a series of grooves in it. The material from the grooves is displaced in the form of wear particles, generally loose ones. Abrasion can occur in a 2 or 3 body system (as above), at different stages of the mild or severe wear process.

1.4. Concepts, Theories & Laws of Friction & Wear

1.4.1 Real Area of Contact

A concept of fundamental importance in the study of friction and wear is that of the "true" or real area of contact.

Since any surface can never be perfectly smooth, on an atomic scale, the real area of contact of two surfaces pressed together under a given load is always considerably less than the apparent area, whether the mode of deformation is plastic or elastic.

For surfaces deforming plastically (8) the real area of contact (A_r) is given by

$$A_r = \frac{W}{P_m} \quad \ldots . \quad (1.1.)$$

where W is the normal load and P_m is the penetration hardness (flow pressure) of the softer material.

In the case of purely elastic deformation there is a much greater contact area. For a spherical asperity (e.g. tip of a ball bearing) resting on a relatively smooth plane (softer metal) surface the contact area is given by Hertz's equation (8):

$$A_r = 1.21\pi \left\{ \frac{Wr}{2} \left(\frac{1}{E_1} + \frac{1}{E_2} \right) \right\}^{\frac{2}{3}} \quad \ldots . \quad (1.2.)$$

where r is the radius of curvature of the asperity, and E_1, E_2 are Young's moduli for the asperity and the surface respectively.

1.4.2. Friction

Friction is expressed in quantitative terms as a force, being the force (F) exerted by either of two contacting bodies tending to oppose the relative tangential displacement of the other. When the applied force is insufficient to cause motion there is static friction between the bodies. When sliding occurs the friction is said to be

kinetic.

The two basic laws of friction are as follows:

1. The friction force F is directly proportional to the normal load W, i.e.

$$F = \mu W \quad . \quad . \quad . \quad . \quad (1.3.)$$

where μ is the coefficient of friction. In general, μ is greater in the case of static friction compared with kinetic friction.

2. The friction force is independent of the apparent area of contact (for most materials excluding elastomers).

Law 1 is in fact an oversimplification. There is a slight variation of the static friction coefficient with time (stick-slip) (16, 17), whereas the kinetic friction coefficient is a function of velocity, throughout the range of sliding speeds (12, 16). Law 2 is only strictly applicable to relatively hard materials.

According to the Bowden and Tabor theory of friction the main resistance to sliding arises from the need to shear strongly adherent surface asperities of the contacting materials. It would appear that adhesion accounts for the greater portion of the friction force (12).

The other main factors contributing to the overall friction are (a) ploughing and to a lesser extent (b) surface roughness (8,12). The ploughing component arises if a hard surface with a sharp end is slid over a soft surface. During sliding the harder material will tend to dig into the softer material, producing a groove. The energy of deformation represented by the groove must be supplied by the friction force, which will therefore be larger than if no such groove was produced.

The roughness component arises from the need, during

the sliding of rough surfaces to lift one surface over the roughnesses of the other.

If the latter term is neglected in the friction process, then the overall friction force is given by the sum of the adhesive and ploughing components, namely:

$$F = sA_r + P^*A_p \quad . \quad . \quad . \quad (1.4.)$$

where s is the average shear strength of the junctions, A_r is the real contact area, P^* is a hardness term of the same order as the flow pressure P_m (8) and A_p is the penetrated area which is swept out.

Under conditions where the friction is almost entirely due to adhesion, the ploughing term in equation (1.4.) can be neglected.

$$\therefore \quad F = s\,Ar = s\,\frac{W}{P_m}$$

$$\mu = \frac{F}{W} = \frac{s}{P_m} = \frac{\text{shear strength of the softer metal}}{\text{flow pressure of the softer metal}} \quad \ldots \quad (1.5)$$

The friction coefficient (as predicted by equation (1.5.)) is similar for a wide range of materials, since s and P_m depend in the same way on such material properties as bond strength and nature of dislocations (12).

An alternative to traditional friction theories has recently been proposed by Rigney and Hirth (18). Their ideas are based on the work required for plastic deformation in the near surface region, described in terms of work hardening, recovery, and the cellular microstructure existing during steady state sliding.

When one of a pair of sliding bodies is much harder than the other the deformation occurs in the near-surface region of the softer material. Rigney and Hirth (18) derived an expression for the friction coefficient as follows. The total plastic work is given

by the product of the deformed volume (V), the shear stress (τ) in the cellular region and in the sliding direction, and the strain per cycle (ϵ) in that region. For a virtual displacement δx the frictional work is given by the product of the friction force (F) and δx. The frictional work must be equal to the total plastic work.

$$\therefore V\tau\epsilon = F\delta x \quad . \quad . \quad . \quad (1.6)$$

The volume is equal to $wt\delta x$, where w is the width of the highly deformed region and t is the thickness.

$$\therefore wt\delta x\tau\epsilon = F\delta x \quad . \quad . \quad . \quad (1.7)$$

$$\therefore \mu W = F = wt\epsilon\tau$$

$$\therefore \mu = \frac{wt\epsilon\tau}{W} \quad . \quad . \quad . \quad (1.8)$$

where W is the normal load.

In order to determine μ , τ and ϵ must be estimated. The authors (18) suggest that the shear stress can be estimated from appropriate tests on severely cold-rolled material with similarly textured cell microstructure. To determine the average net strain per cycle (ϵ), a chemical marker technique in tandum with Auger analysis to measure the variation of gross strain with depth in the near surface region, is suggested.

1.4.3 The Archard Wear Law

Consider the simple model in which individual metallic junctions are formed and sheared. Suppose a junction has a radius 'a', so that its area is πa^2, it supports a normal load $l = P_m \pi a^2$ where P_m is the yield pressure (penetration hardness) of the metal. If a particle is produced when the junction is sheared its volume will be proportional to a^3, ignoring junction growth effects (8). If the fragment is roughly hemispherical (12) its volume is $2/3\pi a^3$.

Since the wear fragment is formed in a sliding distance 2a the wear per unit sliding distance is

$$z = (2/3\pi a^3) \div 2a = \pi a^2 /3$$

But $\pi a^2 = 1/P_m$

$$z = 1/3P_m \quad . \; . \; . \; (1.9)$$

If there is a distribution of junction sizes the same relation will hold for each junction. Since only a fraction K will contribute to wear (19), the total worn volume w per unit sliding distance (assuming geometrically similar wear fragments) will be given by the expression

$$w = \frac{KW}{3P_m} \quad . \; . \; . \; (1.10)$$

where W is the total normal load. The result shows that wear is directly proportional to the load.

The factor '3' arises in equation (1.10.) because it was assumed at the outset that the junctions were circular and the wear fragments hemispherical. The factor arising in the denominator therefore depends on the shape of the junctions and the wear fragments. Using the same argument a similar expression may be derived for wear fragments of other geometries (eg. platelets).

In its more general form the Archard wear law can be written as

$$w = K A_r \quad . \; . \; . \; (1.11.)$$

where A_r is the real area of contact. The parameter K can be interpreted as the probability of producing a wear particle at each asperity - asperity interaction. Inversely, K^{-1} encounters are necessary to form a wear fragment (13).

1.4.4. Wear Theories

Recent theories of wear include (1) the Oxidational

Theory of Mild Wear, originally proposed by Quinn (20), (2) the Theory of Oxide "Glazes" due to Stott and his co-workers (14), (3) the Delamination Wear Theory, proposed by Suh (21), and (4) a wear model due to Rigney and Glaeser (22) which emphasizes plastic deformation near the surface.

For mild wear, the oxidational wear theory leads to the following expression for the wear rate (volume of oxide removed per unit sliding distance) w:

$$w = \left[\frac{d\, Ap \exp - (Qp/R\,(T_o + 273))}{\xi_c^2\, \rho_o^2\, f^2\, u} \right] A_r \quad . \; . \; . \; (1.12)$$

where the portion inside the brackets is the expression for the K-factor. ρ_o is the density of the oxide, f is the fraction of the oxide which is oxygen, ξ_c is the critical oxide film thickness, u is the linear sliding speed, d is the distance of a sliding contact during which oxidation occurs at a temperature T_o, Ap is the Arrhenius Constant for parabolic oxidation during wear, Qp is the Activation Energy for oxidation and R is the Gas Constant. Equation (1.12) only applies when the bulk surface temperature is less than about $300^{\circ}C$. For higher surface temperatures the out of contact oxidation has to be taken into account.

Stott et. al. (14) propose that an oxide "glaze" is formed from the grinding down and smearing due to thermal softening, of larger, compressed oxide particles, resulting from severe deformation and wear during the initial stages of sliding. Once formed, the "glaze" remains stable but is continuously disrupted and reformed during sliding.

The delamination theory of wear is a mechanism based on dislocation theory and the plastic deformation and fracture of metals near the surface (21). As proposed by Suh, it advances the idea of subsurface crack nucleation and crack propogation, leading subsequently

to the delamination of the surface into wear sheets parallel to the surface.

Suh (21) derives an expression for the total wear volume (V) for the case of a hard surface sliding against a soft surface, namely:

$$V = N_1(S/So_1)\, A_1 h_1 + N_2\,(S/So_2)\, A_2 h_2 \quad \ldots (1.13)$$

where A is the average area of the delaminated sheet, h is the thickness of the sheet, and S is the total distance slid. The subscripts 1 & 2 refer to the soft and hard metals. So is defined as the critical sliding distance required to remove a complete layer of material, consisting of N wear sheets. Consequently, the ratio (S/So) is equal to the number of layers removed.

Engel (23) shows that equation (1.13) can be written in the alternative form

$$\frac{V}{S} = w = \left[\frac{B_1\, h_1}{dc_1} + \frac{B_2\, h_2}{dc_2}\right] A_r \quad \ldots (1.14)$$

where the bracketed expression is the K-factor; dc_1 and dc_2 are the critical plastic displacements, B_1 and B_2 are dependent mainly on topography but are not very well defined.

Rigney and Glaeser (22) have described a wear model in which attention is focused on steady state wear. They emphasized plastic deformation near the surface, particularly in the highly deformed region which has a fine microstructure and a high degree of preferred orientation. In metals and in some ceramics, this near-surface microstructure consists of dislocation cells developed during the initial run-in period of sliding. Under steady state conditions the average cell structure at a given distance from the surface remains constant, and the average thickness t of the cell region is a constant that depends on material properties and on the details of the sliding wear test. The ideas are

applied to friction as well (18).

1.5 Thermal Aspects of Sliding

Nearly all the energy dissipated by friction appears as heat. The temperature of the sliding bodies is raised appreciably at all but the lowest speeds of sliding. The highest temperatures occur in the regions of real contact between the sliding members. These temperatures can have a considerable influence on friction and wear, and an estimate of their magnitude is usually required (24).

In some cases, theoretical estimates of such temperatures may be compared with the temperature range for certain oxide phases (25), the temperature for phase changes in metals (5), or with surface melting. Detailed theoretical analyses of the problem is available in the work of Blok (26) and Jaeger (27), with Archard (24) providing a simplified version.

There have been many attempts to directly measure the temperatures of the interfaces of sliding surfaces. These methods have tended to involve the dynamic thermocouple, eg. Shore (28), Herbert (29) and Furey (30). As regards the sliding material couple, these methods have tended to be restrictive and are insensitive to the rapid transients which occur during sliding.

An elegant method of deducing surface temperatures during steady state sliding is that of calculating accurately the heat flow rates, by means of thermocouple measurements of temperature at strategic points along one of the sliding bodies (31). The details of this method are discussed in Chapter 5.

1.6 Research Programme

The friction and wear behaviour of these diesel engine

materials (Brico 65 and 21 - 4N) under conditions promoting oxidational wear has not been previously studied. With this view in mind, the variables were limited to load, speed and temperature; wear tests being carried out using a machine of pin-on-disc geometry, under an open atmospheric environment. Numerous methods were used to examine the specimens and the wear fragments after testing (eg. X-ray diffraction, SEM), in addition to heat flow analysis (in the hope that a pattern between wear and heat flow would emerge).

In the present work the main objective is the understanding of the fundamental mechanisms by which these materials wear. It is hoped that this work will be further advanced in the future to include other operating variables such as different gas environments and a change from continuous sliding to one of impact. This will, of course, simulate the original problem to a greater degree.

CHAPTER 2

DESIGN OF THE PIN-ON-DISC WEAR MACHINE

2.1 Design Requirements

In the design of the wear test rig it was essential to ensure that experiments could be carried out over a wide range of loads, speeds and elevated temperatures. It was also necessary to calculate the maximum "stresses" which the component parts of the machine (shafts, bearings, motor, etc.) would be subjected to during running so that the rig would operate safely.

2.2 Speed Range

An efficient method of obtaining a wide range of sliding speeds is to use a variable speed drive, coupled with an external arrangement of pulleys and V-belts. The particular drive selected for this application consisted of a motor, variable speed pulley and a reduction gearbox (Figure 2.1). The variable speed drive had the following characteristics:

(a) Speed range : 120 - 720 RPM

(b) Shaft diameter : 30 mm

(c) Power rating : 2.24 kW (3 HP)

From the manufacturers catalogues on power transmission (32) the minimum pulley diameter with the above bore was 95 mm. The diameter of the wear disc was chosen to be 127 mm and the pin was positioned on the same horizontal level as the disc, about 50.8 mm from its centre.

If the minimum disc speed is 0.2 m/s then the minimum angular velocity at the top pulley (Figure 2.2) is

$$\omega_{min} = 0.2/0.0508 = 4 \text{ rads/sec} = 38 \text{ RPM}.$$

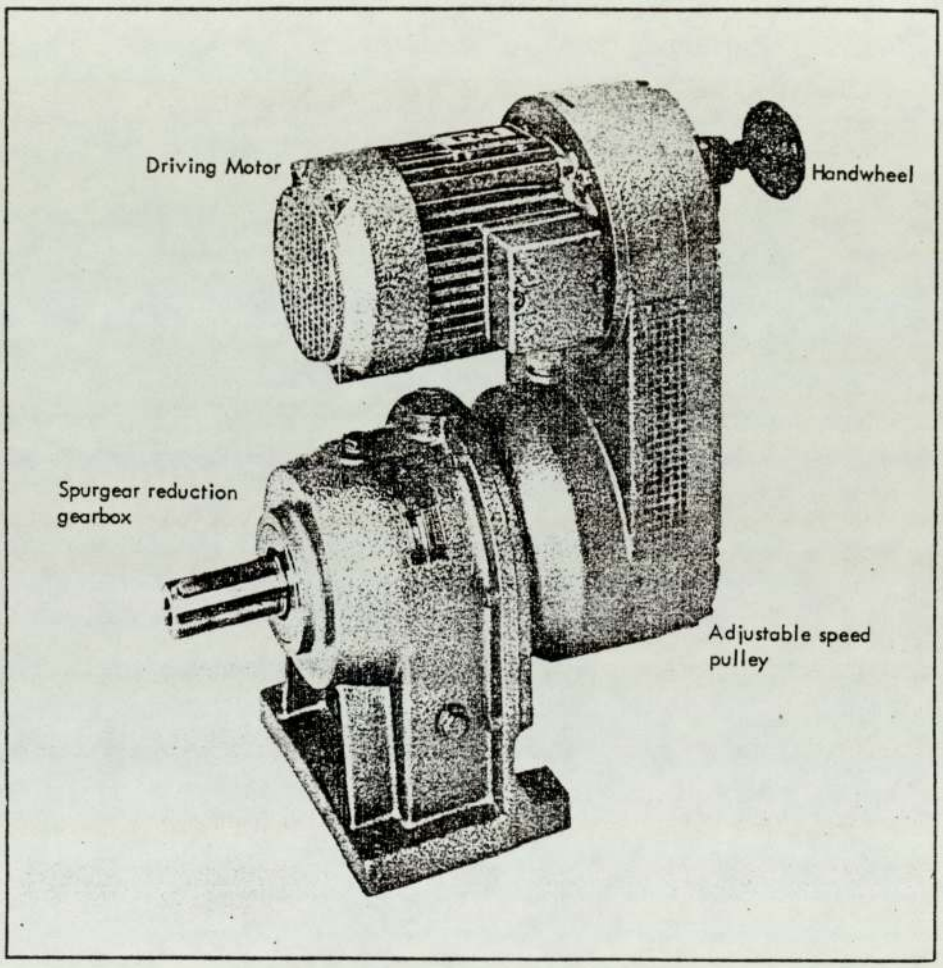

Figure 2.1

Variable Speed Drive .

For any two pulleys linked by a V-belt (Figure 2.2), the velocity along the belt must be continuous.

$$\therefore \quad \omega_1 d_1 = \omega_2 d_2$$

$$\therefore \quad \frac{\omega_1}{\omega_2} = \frac{d_2}{d_1} \qquad \ldots . 2.1$$

where ω_2 and ω_1 are the respective angular speeds at the top and bottom of the drive, d_1 and d_2 being the pulley diameters.

If ω_1 = 120 RPM and $\omega_2 = \omega_{min}$ = 38 RPM,

for d_1 = 95 mm, $d_2 = (\omega_1 / \omega_2)\, d_1 = (120/38)\, 95$ = 300 mm

From the manufacturers specifications a pulley 315 mm in diameter was selected. This size gave an output speed of

$$V_{min} = 2\pi\,(120 \times 95/315) \times 50.8/60 = 0.192 \text{ m/s}$$

For the higher end of the speed range the pulley diameters selected were, d_1 = 160 mm and d_2 = 80 mm. Hence when

$$\omega_1 = 720 \text{ RPM} \quad \omega_2 = 160 \times 720/80 = 1440 \text{ RPM}$$

Therefore the maximum output speed at a distance 50.8 mm from the disc axis is

$$V_{max} = (1440/60) \times 2\pi \times 50.8 \text{ mm/s} = 7.66 \text{ m/s}$$

Clearly with the two sets of pulley systems the range of speeds is from 0.19 - 7.66 m/s.

The angular speeds were measured by means of an optical digital tachometer which works on the stroboscope principle. In a typical measurement one or more pieces of light sensitive reflecting tape of approximately 3 mm square were attached to the flat surface of the rotating pulley. A light beam from the instrument was directed at the reflecting tape and when the digital readout from the tachometer was steady the value of the angular speed (in RPM) was taken. When two

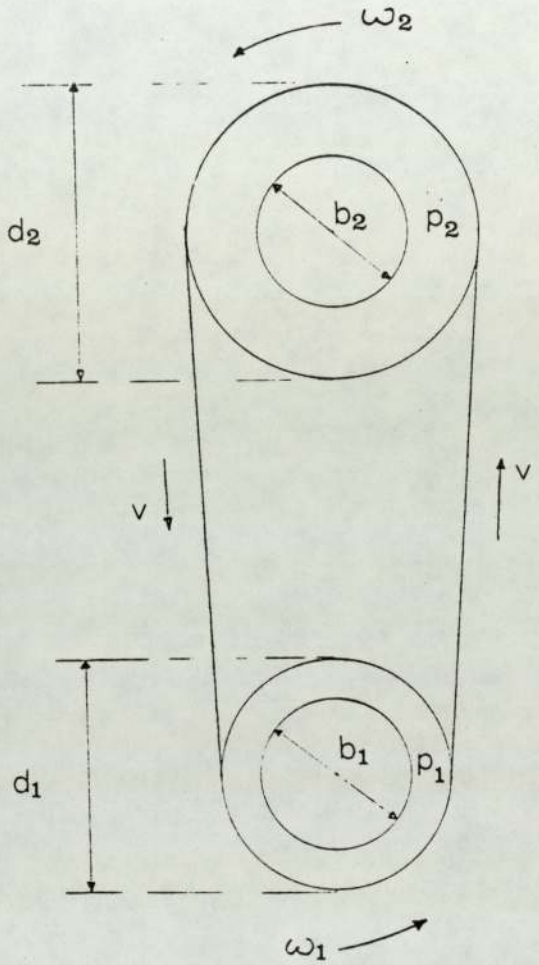

Figure 2.2

V-belt Drive .

pieces of tape were used the actual angular speed was one half the value recorded by the instrument, when three pieces of tape were used the angular speed was a third of the recorded value, etc.

2.3 Maximum Resistive Power

The maximum load that can be applied to the pin-disc system is limited by the maximum power which can be developed by the motor. Work has to be done by the motor in order to overcome the frictional torque produced at the pin-disc interface (Figure 2.3). The maximum values of the parameters used to calculate the resistive power were:

(a) Distance of pin from disc centre, r = 0.057 m

(b) Coefficient of friction at the pin-disc interface, $\mu = 1.0$.

(c) Normal load, W = 196.2N

The frictional torque about the disc axis is equal to the product of the friction force and the distance between the centres of the pin and disc (Figure 2.3). Hence

$$T = F \times r = \mu W r \quad \ldots \quad (2.2)$$

$$\therefore T_{max} = 1 \times 196.2 \times 0.057 \simeq 11.18 \text{ Nm}$$

For the set of pulleys with diameters d_1 = 160 mm and d_2 = 80 mm, the resistive torque at the gearbox is

$$T_{max}^{gb} = 11.18 \times 160/80 = 22.36 \text{ Nm}$$

The work rate at the gearbox is given by the product of the torque and the total angle of twist per second.

i.e. $$p = T \times \frac{d\theta}{dt} \quad \ldots \quad (2.3)$$

Hence at 720 RPM the power developed by the motor is :

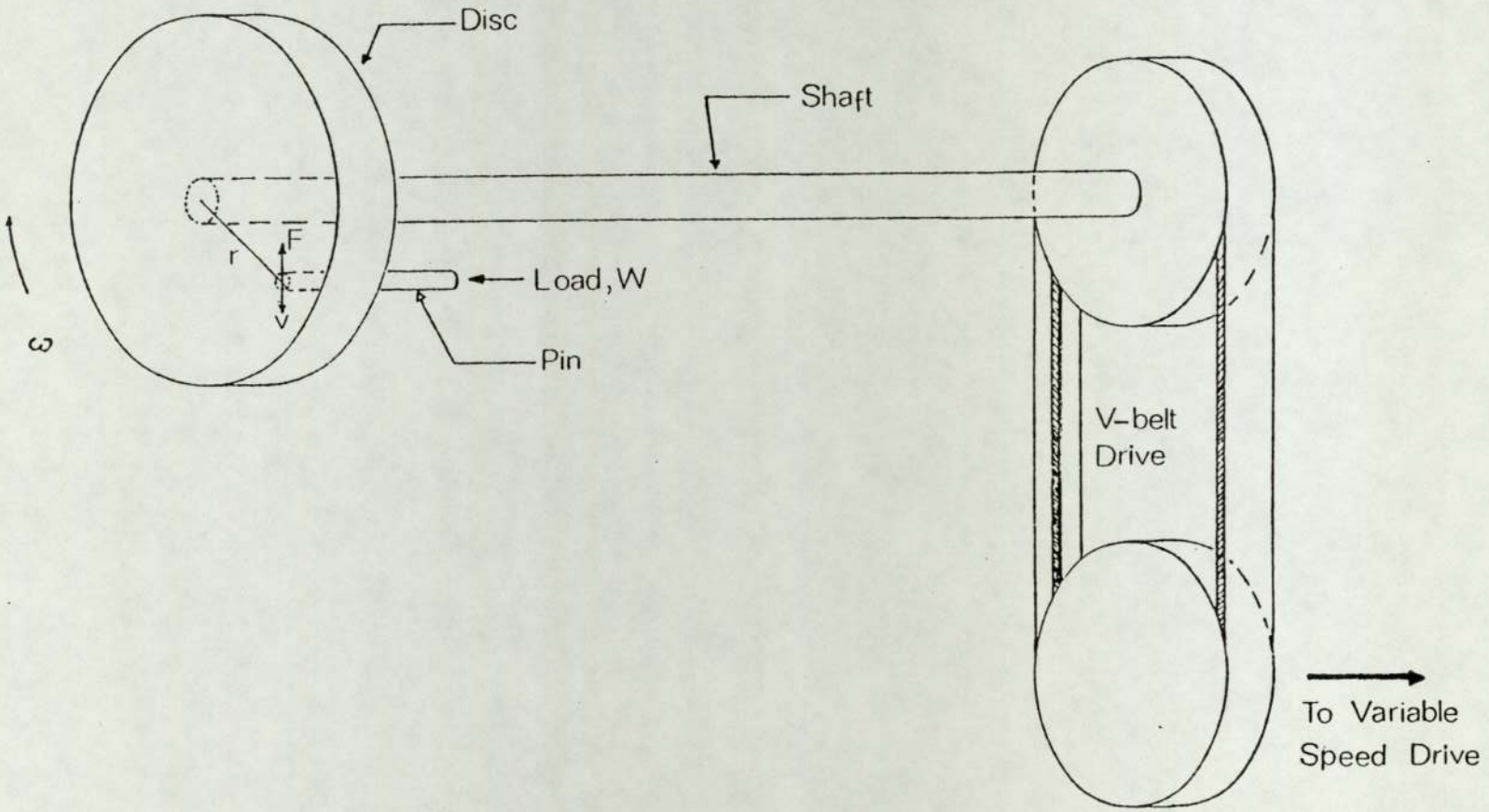

Figure 2.3

Generation of Frictional Torque at Pin-Disc Interface .

$P_{max} = 22.36 \times (720/60) 2\pi \simeq 1.7$ kW

At 120 RPM, with the pulley set $d_1 = 95$ mm and $d_2 = 315$ mm, the power developed is

$$P_{min} = (11.18 \times \frac{95}{315}) \times \frac{120}{60} \times 2\pi \simeq 0.04 \text{ kW}.$$

2.4 Pulley Belts

(a) Power Ratings

For the pulley combination of $d_1 = 160$ mm and $d_2 = 80$ mm, the manufacturers tables on power transmission for A-section V-belts gave a rated power per belt of 1.04 kW. Therefore, the number of belts required to transmit the maximum power of 1.7 kW is $n = 1.7/1.04 = 1.64$. A pair of A-section V-belts of the appropriate length were selected.

For the pulley set $d_1 = 95$ mm and $d_2 = 315$ mm tables gave a rated power of 0.12 kW per belt. A matched pair of V-belts were selected so that a maximum power of 0.24 kW could be transmitted, for the lower speeds.

(b) Belt Length

Shigley (33) has shown that the pitch length of a V-belt (Figure 2.4) is given by

$$L = \left[4C^2 - (D - d)^2\right]^{\frac{1}{2}} + \tfrac{1}{2}(D\,\theta_L + d\,\theta_s) \quad \ldots (2.4)$$

where

$$\theta_L = \pi + 2 \sin^{-1}\left((D - d)/2C\right) \quad \ldots \quad (2.4a)$$

$$\theta_s = \pi - 2 \sin^{-1}\left((D - d)/2C\right) \quad \ldots \quad (2.4b)$$

When deciding on the centre distance (C) for a V-belt drive it is necessary that C lies in the range

$$D < C < 3\,(D + d)$$

Long centre distances can cause excessive vibration of the slack side

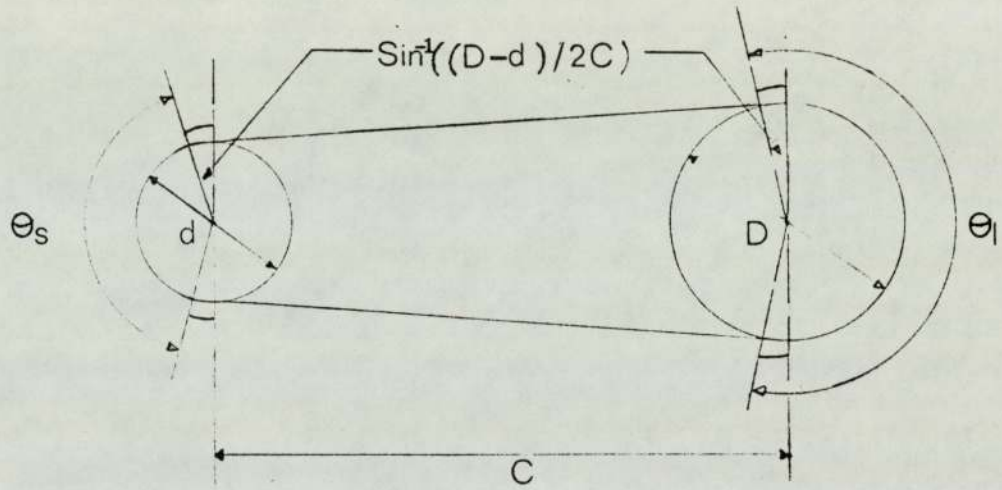

Figure 2.4

V-belt Geometry.

of the belt which will shorten the belt life. Due to limiting factors such as the machine frame dimensions a centre distance, C = 368 mm was selected.

For the pulley set D = 160 mm, d = 80 mm the contact angles are

$$\theta_L = \pi + 2 \sin^{-1} [(160 - 80) /2 \times 368] = \pi + 2 (.10891)$$

$$= 3.359 \text{ radians} \simeq 192^{\circ}27'$$

$$\theta_s = \pi - 2 \sin^{-1} [(160 - 80) /2 \times 368] = \pi - 2 (.10891)$$

$$= 2.924 \text{ radians} \simeq 167\tfrac{1}{2}^{\circ}$$

$$\therefore L = [4(368)^2 - (160 - 80)^2]^{\frac{1}{2}} + \tfrac{1}{2} [160 (3.36) + 80 (2.924)]$$

$$= \sqrt{535296} + \tfrac{1}{2} (771.5) = 1117.4 \text{ mm.}$$

From the manufacturers specifications on A-section V-belts, the nearest belt size was found to be A1120, therefore a matched pair of this size was selected.

For the pulley set D = 315 mm and d = 95 mm, the contact angles are

$\theta_L = \pi + 2 \sin^{-1} [(315 - 95) /2 \times 368] = \pi + 2 \sin^{-1} (.2989) =$

$3.75 \text{ radians} \simeq 214^{\circ} 47'$

$\theta_s = \pi - 2 \sin^{-1} [(315 - 95) /2 \times 368] = \pi - 2 \sin^{-1} (.2989) =$

$2.53 \text{ radians} \simeq 145^{\circ}13'$

$\therefore L = [4(368)^2 - (315 - 95)^2]^{\frac{1}{2}} + \tfrac{1}{2}[315 (3.75) + 95(2.53)] = 1413.2 \text{ mm}$

A pair of belts designated A1410 was selected.

2.5 Design of Shaft

2.5.1 Stresses due to combined bending and torsion

A very important application of the theory of combined stresses arises in the case of shafts subjected to both bending and torsion.

Consider a portion of a hollow shaft of circular cross-section (Figure 2.5) acted upon at its ends by bending couples M in the x-z plane and by twisting couples T about the x-axis. Under such loading, an element 'A' in the side surface of the shaft will be in the worse state of stress, carrying normal stresses σ_x due to bending and shearing stresses τ_{xy} due to torsion. It has been shown by Timoshenko (34) that the magnitude of these stresses are given by the equations:-

$$\sigma_x = \frac{32\ M d_o}{\pi(d_o^4 - d_i^4)} \quad \ldots (2.5)$$

and $$\tau_{xy} = \frac{16T\ d_o}{\pi(d_o^4 - d_i^4)} \quad \ldots (2.6)$$

where d_o and d_i are the external and internal diameters of the shaft, respectively (see Appendices 1 and 2).

The element A is seen to be in a state of plane stress and the principal stresses can be found by modifying the general equations (deduced from the Mohrs circle diagram) :

$$\sigma_{1,2} = \frac{\sigma_x + \sigma_y}{2} \pm \left(\left(\frac{\sigma_x - \sigma_y}{2}\right)^2 + \tau_{xy}^2\right)^{\frac{1}{2}} \quad \ldots (2.7)$$

$$\tau_{max} = \frac{\sigma_1 - \sigma_2}{2} = \pm\left(\left(\frac{\sigma_x - \sigma_y}{2}\right)^2 + \tau_{xy}^2\right)^{\frac{1}{2}} \quad \ldots (2.8)$$

Since there is no normal stress in the y-direction (Figure 2.5), $\sigma_y = 0$. Thus the principal normal and shear stresses are

$$\sigma_{1,2} = \sigma_x/2 \pm \left((\sigma_x/2)^2 + \tau_{xy}^2\right)^{\frac{1}{2}} \quad \ldots (2.9)$$

and

$$\tau_{max} = (\sigma_1 - \sigma_2)/2 = \pm\left((\sigma_x)^2 + \tau_{xy}^2\right)^{\frac{1}{2}} \quad \ldots (2.10)$$

In the design of a shaft to carry a given loading,

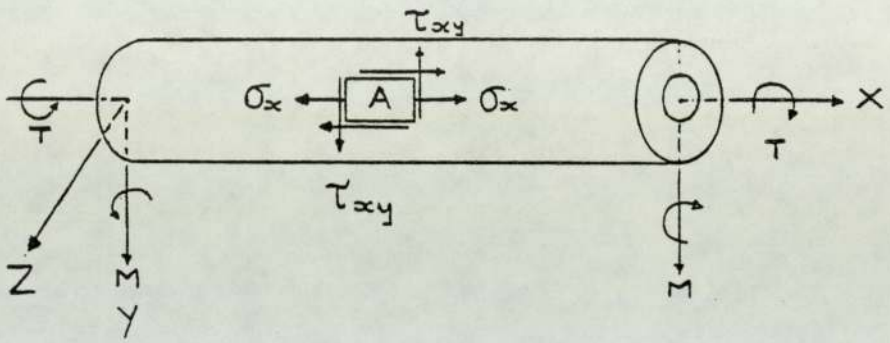

Figure 2.5

Shaft Subjected to Combined Bending and Torsion.

allowable working stresses in tension (or compression) and in shear will usually be prescribed. It then becomes necessary to decide which of these stresses governs the design and then select the required diameter of the shaft accordingly. For a brittle material like cast-iron, the maximum normal stress σ_1, should be used, while for a ductile material like structural steel, the maximum shear stress τ_{max} is most commonly used.

2.5.2 External Shaft Diameter

The material to be used for the shaft is mild steel, which is weaker in shear than in tension. Hence only the maximum shear stress requires consideration. An expression for the external diameter d_o, of the shaft can be found by substituting for σ_x and τ_{xy} from equations (2.5) and (2.6) into equation (2.10). On substitution,

$$\tau_{max} = \left[\left[\frac{16\ M\ d_o}{\pi(d_o^4 - d_i^4)} \right]^2 + \left[\frac{16\ T\ d_o}{\pi(d_o^4 - d_i^4)} \right]^2 \right]^{\frac{1}{2}}$$

$$\therefore \quad \tau_{max} = \frac{16\ d_o\ (M^2 + T^2)^{\frac{1}{2}}}{\pi\ (d_o^4 - d_i^4)} \qquad \ldots (2.11)$$

If τ_w is the prescribed allowable working stress the design criterion for the shaft is

$$\tau_w \geq \frac{16\ d_o\ (M^2 + T^2)^{\frac{1}{2}}}{\pi(d_o^4 - d_i^4)} \qquad \ldots (2.12)$$

where $\tau_w = 600$ p.s.i. (4.15×10^7 N/m^2) is a commonly used value. In equation (2.12) all the quantities, except the external diameter, can be calculated from other considerations. Clearly, any value of d_o which satisfies the inequality will be acceptable from a stress view point.

The greatest value of bending moment (M) can be found by calculating the tensions in the pulley belt when the largest power is being transmitted (see Figures 2.6 (i) and (ii)).

Due to friction between the pulley and the belt, on either side of the pulley the tensions in the belt will be different. Under conditions where centrifugal forces can be neglected (low belt mass and medium or low belt velocity) Shigley (33) has shown that the tensions are related through the equation

$$P_1 = P_2 \exp(\mu\theta) \quad \ldots (2.13)$$

where P_1 and P_2 are the tensions in the belt, μ the coefficient of friction between belt and pulley and θ the angle of contact.

The tensions are related to the torque through the equation

$$T = (P_1 - P_2)\, D/2 \quad \ldots (2.14)$$

where D is the pulley diameter. Equations (2.13) and (2.14) represent two equations in the unknowns P_1 and P_2 and hence they may be determined. The maximum bending moment to which the shaft will be subjected can then be determined from the expression

$$M_{max} = \tfrac{1}{2} (P_1 + P_2)\, x_{max} \quad \ldots (2.15)$$

where x_{max} is the distance between the centres of the pulley and supporting bearing B (see Figure 2.6).

Critical values for the parameters in the calculation were

Internal shaft diameter, d_i = 0.0167m (21/32")

Maximum torque (from Section 2.3.3), T_{max} = 11.18 Nm

Minimum pulley diameter, D_{min} = 0.08 m

Angle of contact between belt and pulley, θ = 2.924 radians

Minimum coefficient of friction between belt and pulley, $\mu \simeq 0.3$

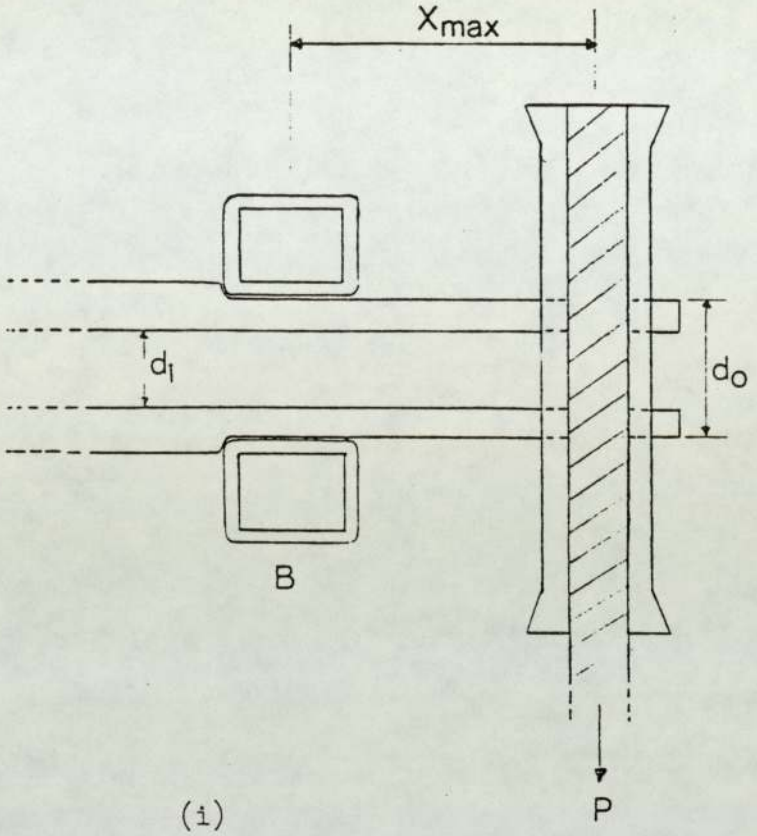

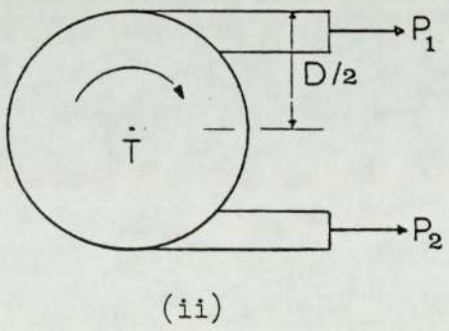

Figure 2.6

Belt Tensions giving rise to (i) Bending Moment and (ii) Torque .

Maximum distance between pulley and bearing centres x_{max} = 0.04445m ($1\frac{3}{4}$")

From equations (2.13) and (2.14) the tensions in the belt are given by

$$P_2 = \frac{2T}{D(\exp(\mu\theta)-1)} \quad \ldots \quad (2.16)$$

$$P_1 = \frac{2T \exp(\mu\theta)}{D(\exp(\mu\theta)-1)} \quad \ldots \quad (2.17)$$

Substitution yields

$$P_2 = 199.1N \qquad \text{and}$$

$$P_1 = 478.6N$$

$$\therefore M_{max} = \tfrac{1}{2}(199.1 + 478.6) \times .04445 = 15.06 \text{ Nm}$$

$$\therefore (M_{max}^2 + T_{max}^2)^{\frac{1}{2}} = (15.06^2 + 11.18^2)^{\frac{1}{2}} = 18.75 \text{ Nm}$$

If the external shaft diameter d_o = 0.0254 m then

$$\frac{16\, d_o\, (M^2 + T^2)^{\frac{1}{2}}}{\pi(d_o^4 - d_i^4)} = \frac{16 \times 0.0254 \times 32.13}{\pi(.0254^4 - (.0167)^4} = 0.72 \times 10^7 \text{ N/m}^2$$

This is less than the allowable working stress τ_w (4.15×10^7 N/m^2). Hence, an external shaft diameter of 25.4 mm would be acceptable. However, other factors had to be considered. For example, the size of pulley bores and bearings. In fact, a value of 28.575 mm ($1\frac{1}{8}$ ") was selected.

2.5.3 Selection of Bearings

A pair of tapered roller bearings of low K factor (ratio of radial load rating to thrust load rating) were selected to support thrust loads, caused by the loading of the pin-on-disc, and to ensure true shaft alignment during operation of the wear machine.

The bearings were selected on the basis of a maximum

required dynamic thrust load rating, given by the formula

$$CA(90) = \frac{F_a \times LF \times AF}{SF} \quad \ldots (2.18)$$

where F_a is the maximum thrust load to be applied, AF the application factor (depending on the conditions of use), LF the life factor and SF the speed factor. The life and speed factors are given by the equations (35)

$$LF = (\text{required life } /3000)^{.3} \quad \ldots (2.18a)$$

$$SF = (500/ \text{ maximum RPM})^{.3} \quad \ldots (2.18b)$$

where the required life is the time for 90% of the rollers to cease functioning. The following values for the parameters were used to calculate the dynamic thrust load.

Maximum thrust load, F_a = 110 lb (50N)

Maximum RPM = 1440

Required life $\simeq 10^8$ hours

Application factor, AF = 1

$$\therefore LF = (10^8/3000)^{.3} = 22.74$$

$$SF = (500/1440)^{.3} = 0.728$$

$$\therefore CA(90) = \frac{110 \times 22.74 \times 1}{.728} \simeq 3436 \text{ lbs}$$

On the basis of the above calculations a pair of tapered roller bearings each with a CA(90) rating of 4700 lbs, K factor of 0.7 and bore of $1\frac{5}{8}$" were selected from the manufacturers (35) specifications.

A cylindrical roller bearing of bore $1\frac{1}{8}$" (minimum shaft diameter) and load rating of 5050 lbs was selected to support radial loads.

The particular bearing assembly used in the design of the shaft is shown in Figure 2.7.

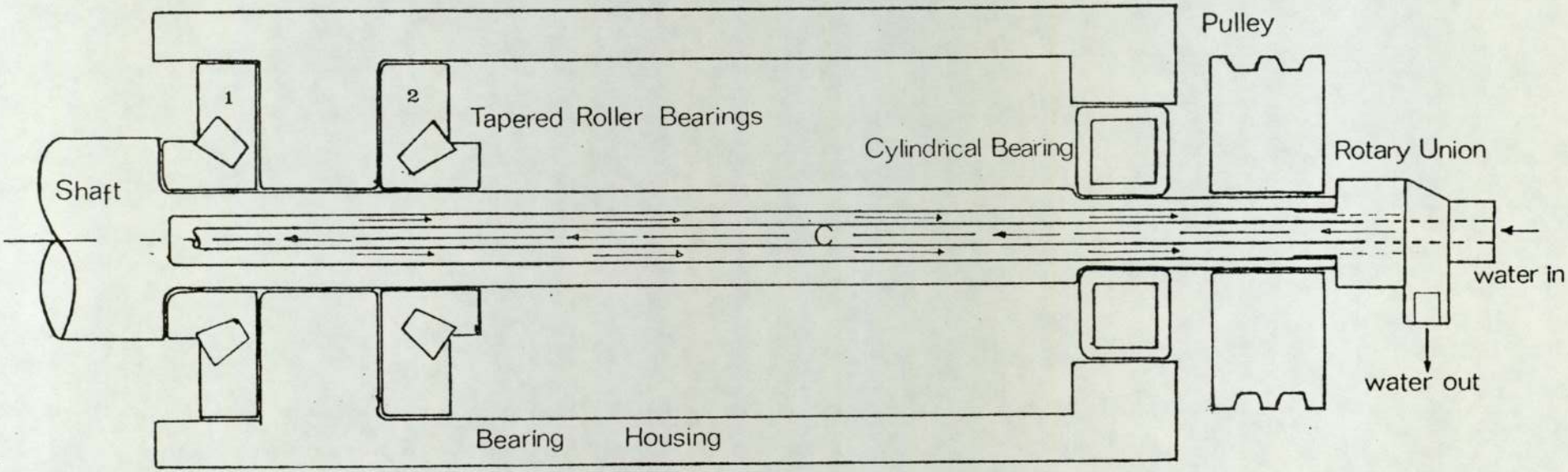

Key

C Centre Tube

Figure 2.7

Bearing Assembly and Water Cooling Facility .

2.5.4 Lubrication of Bearings

Since the wear machine had a maximum rotational speed of only 1440 RPM, grease lubrication was used, in which the spaces between the races and rolling elements of the bearings were filled with grease. Felt seals were used to ensure contact between grease and the rolling elements and also to prevent dirt contamination of the bearings.

CHAPTER 3

EXPERIMENTAL DETAILS

3.1 Introduction

In the present investigation the unlubricated friction and wear behaviour of Brico 65 sliding on 21 - 4N was studied under various experimental conditions.

The experimental conditions used were those of an air environment, a range of loads and sliding speeds, and elevated temperatures induced by external heating. The experimental work was divided into two main sections:-

(i) The friction and wear behaviour of Brico 65, with no external heating.

(ii) The friction and wear behaviour of Brico 65 at elevated temperatures.

3.2 The Wear Machine

The wear experiments were carried out on a continuous sliding pin-on-disc wear test rig. The pin-on-disc facility of the machine provided a flat-on-flat geometry test situation.

Brico 65 was used as the pin material, so that its wear could be continuously monitored.

At the start of the research project a wear test rig of the above type was designed. The essentials of the design were discussed in Chapter 2.

3.2.1 Main Features of the Wear Rig

Essentially, the machine consisted of a horizontal pin holder attached to a horizontal shaft, in rotary-linear bearings. This enabled the pin to be loaded pneumatically against the flat face of the disc

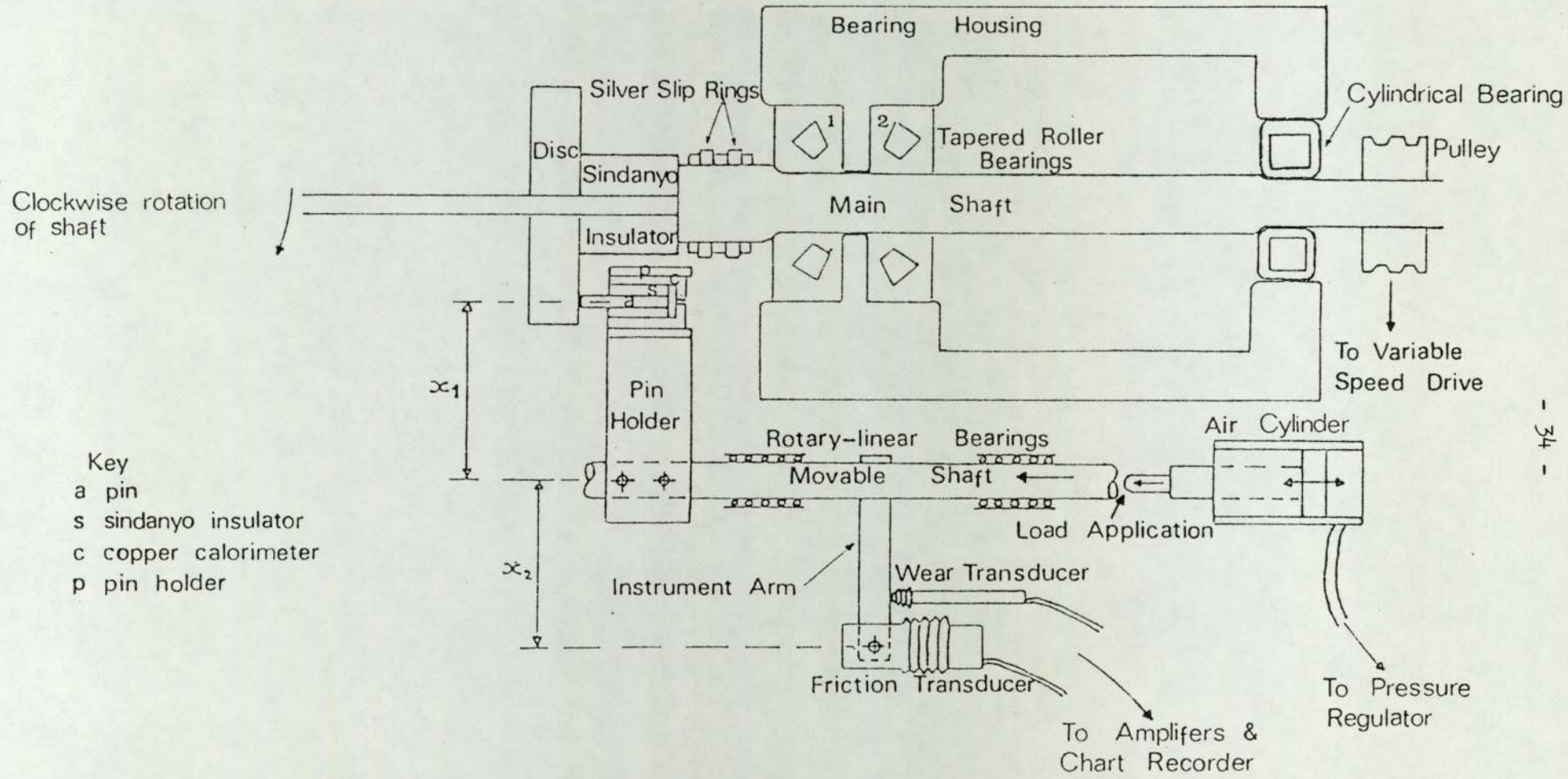

FIGURE 3.1 Main Features of the Wear Test Rig.

which was held in position on a horizontal shaft by three bolts threaded into the main shaft (see Figure 3.1). The main shaft assembly was then driven by a motor-pulley system of variable speed (as described in Section 2.3.2).

3.3 Load Application

The load was applied to the pin by means of an air cylinder (see Figure 3.1). In order to reduce the internal friction in the piston, silicone oil was applied to the rubber seal. With the friction reduced to a minimum, it was possible to accurately apply loads from 12.5 N to 200N. The load was controlled by means of a pressure regulator in conjunction with a pressure gauge (see Figure 3.2).

Using the manufacturer's (36) calibration factor for the air cylinder, which was checked experimentally, using strain gauges, it was possible to convert the load from pressure units (bars) to force units (newtons). The calibration factor given by the manufacturer was, 1 bar = 125.6N, and that found experimentally was 1 bar = 125 N. The latter calibration was used in all subsequent calculations.

3.4 Measurements of Temperatures

In all the test runs the temperatures at strategic points along the pin were monitored in order to obtain heat flow information. This was achieved by using a special calorimeter arrangement (see Figure 3.3). Chromel-alumel thermocouples were spot-welded at the points indicated along the pin. The pin was then fitted between two hollow cylindrical halves of sindanyo insulator (with grooves for the outward passage of the thermocouple leads). The assembly was then pushed into the calorimeter until the rear end of the pin was coincident with the copper disc. The

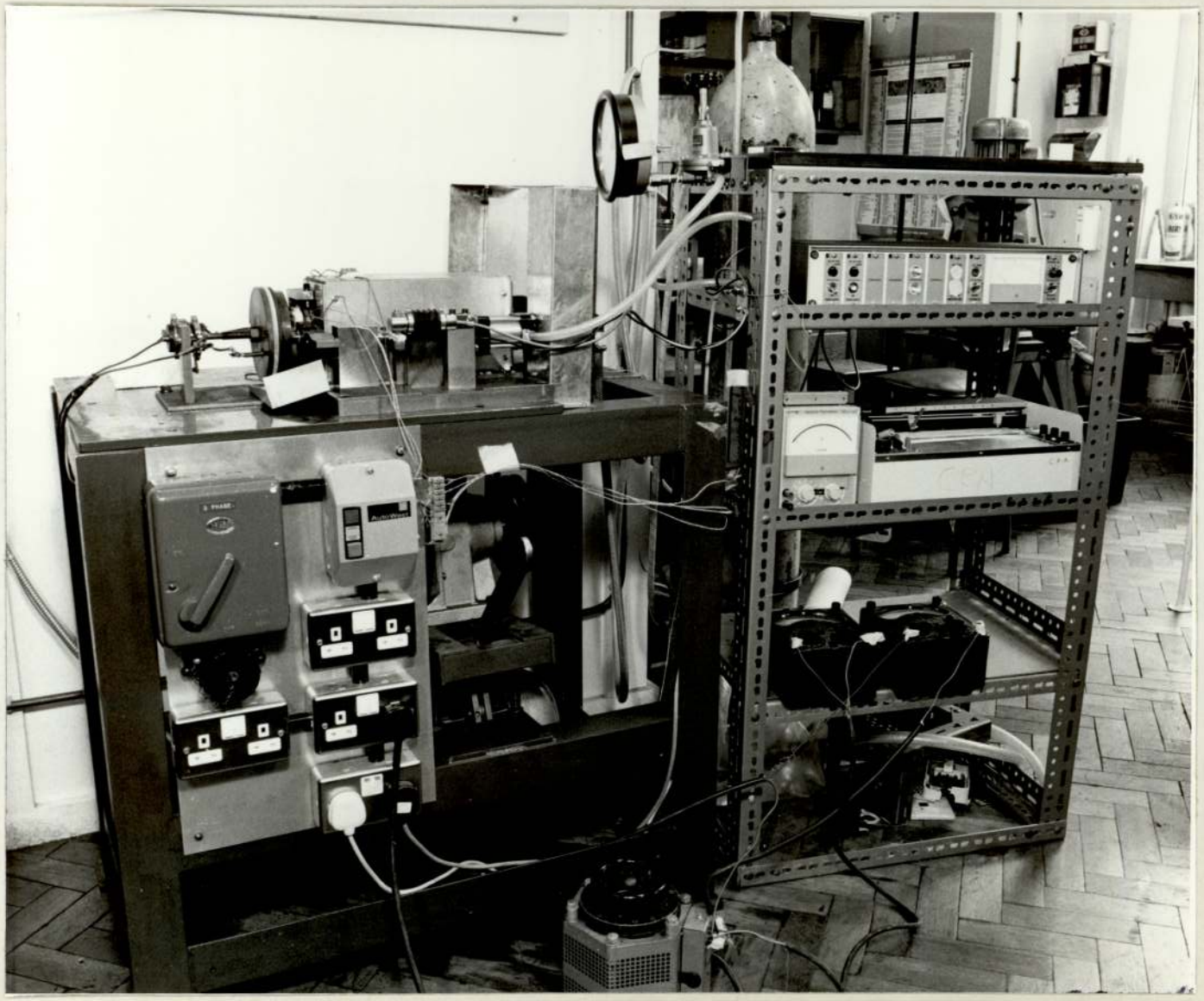

FIGURE 3.2 (a)
General View of the
Pin-on-Disc Wear Machine.

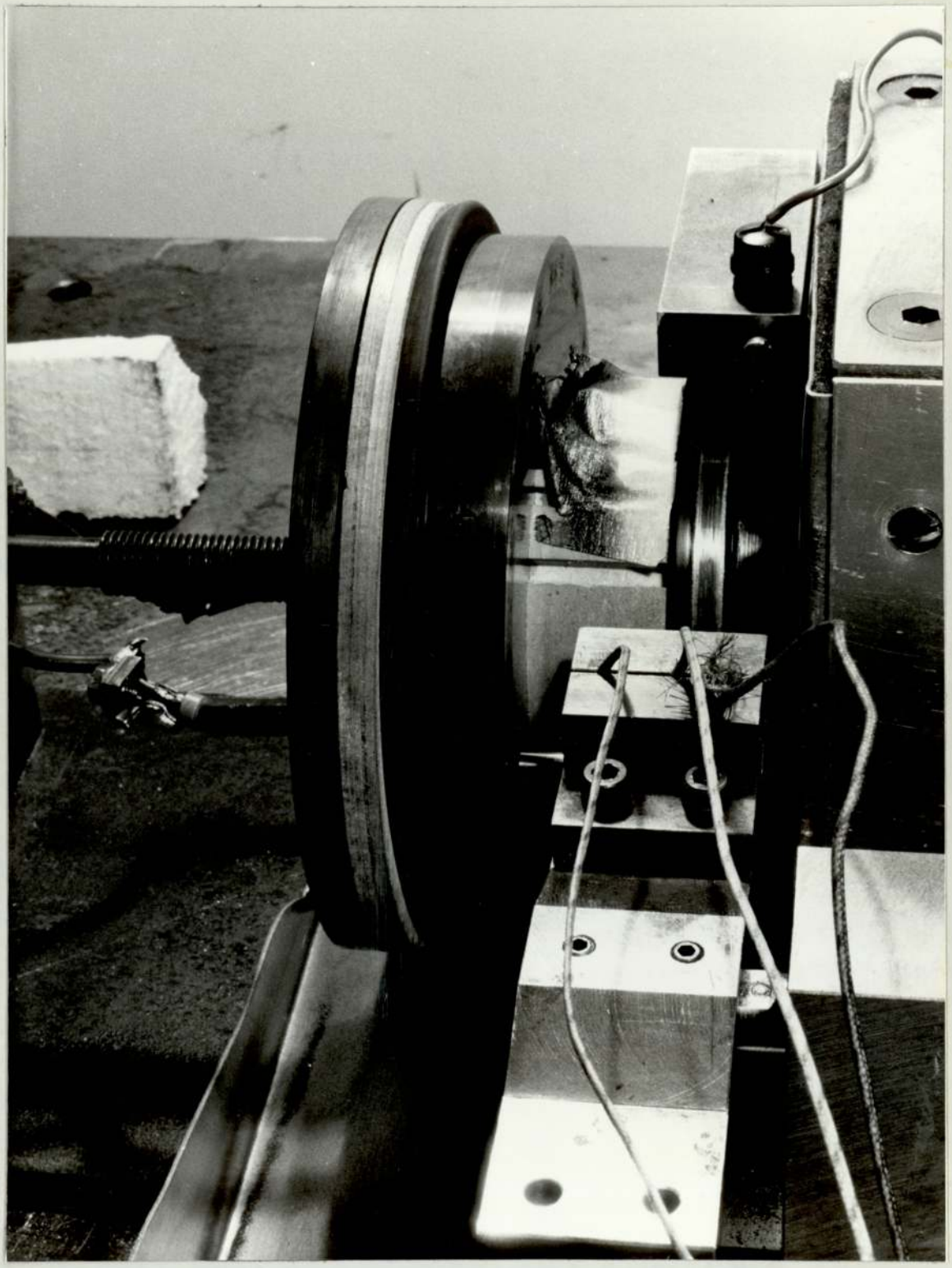

FIGURE 3.2 (b) Close-up view of wear-face with heater and thermocouples.

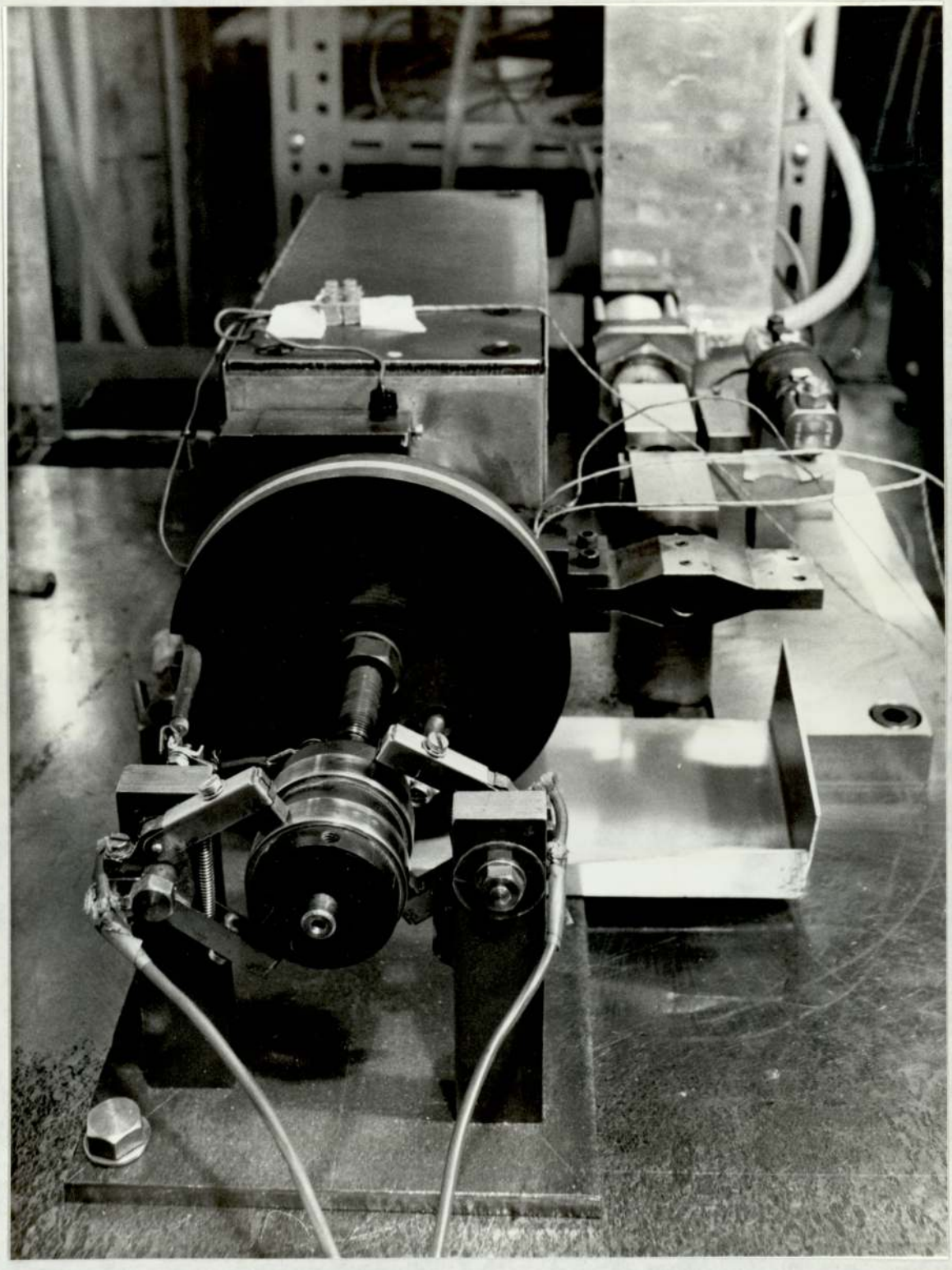

FIGURE 3.2 (c) Close-up view of slip-ring-brush assembly .

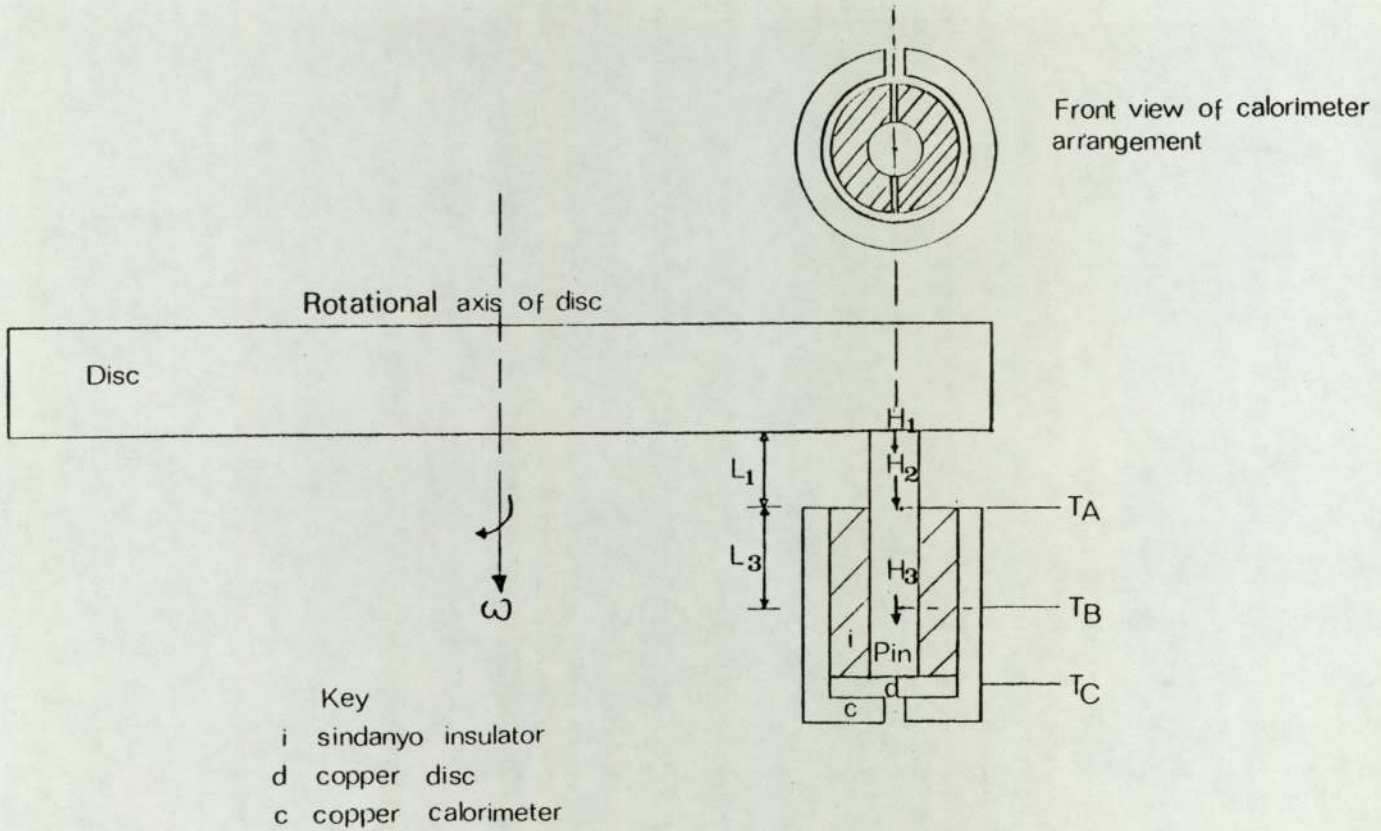

FIGURE 3.3 Calorimeter Arrangement for Heat Flow Measurement along Pin and Pin Position relative to Rotational Axis of Disc.

calorimeter was then pushed into the holder and the side screws tightened until the pin was rigidly clamped.

The temperature of the disc was measured by a thermocouple close to the wear track, the temperature being recorded on an electronic thermometer, via a silver slip-ring-brush assembly. (Figure 3.2 (b)).

3.5 The Specimens

Discs of diameter 127 mm and 14 mm in thickness were machined from 21 - 4N billets. Pins approximately 32 mm long and 6 mm in diameter were machined from castings of Brico alloy 65.

In order to facilitate analysis of 21 - 4N after the experimental investigations, studs of the material, 8 mm in diameter and approximately 10 mm in length, were inserted in the discs. Two studs were inserted in each disc at diametrically opposite positions, centred about the point where the middle of the wear track annulus would occur (see Figure 3.4).

Both pins and discs were ground to a surface finish of approximately 0.2 μm CLA. The surface roughness was checked using a talysurf profilometer. The specimens were degreased using detergent, washed in water, then in acetone, and dried.

The materials had the following compositions:-

	Fe	Cr	Mn	Ni	Si	C	Mo	P	S	N
BRICO 65(Pin)%	73-74	20-21	0.57	1.5	1.5-2.0	1.75	.04	Φ.04	.03	-
21 - 4N (DISC)%	65.5	21.0	9.0	4.0	.1	.5	-	.01	-	.4

The micrographs (Figure 3.5) show the microstructures of 21 - 4N (austenitic stainless steel) and Brico 65 (ferritic steel). The nominal bulk hardness of the specimens was found to be 360 ± 20 VPN, at room

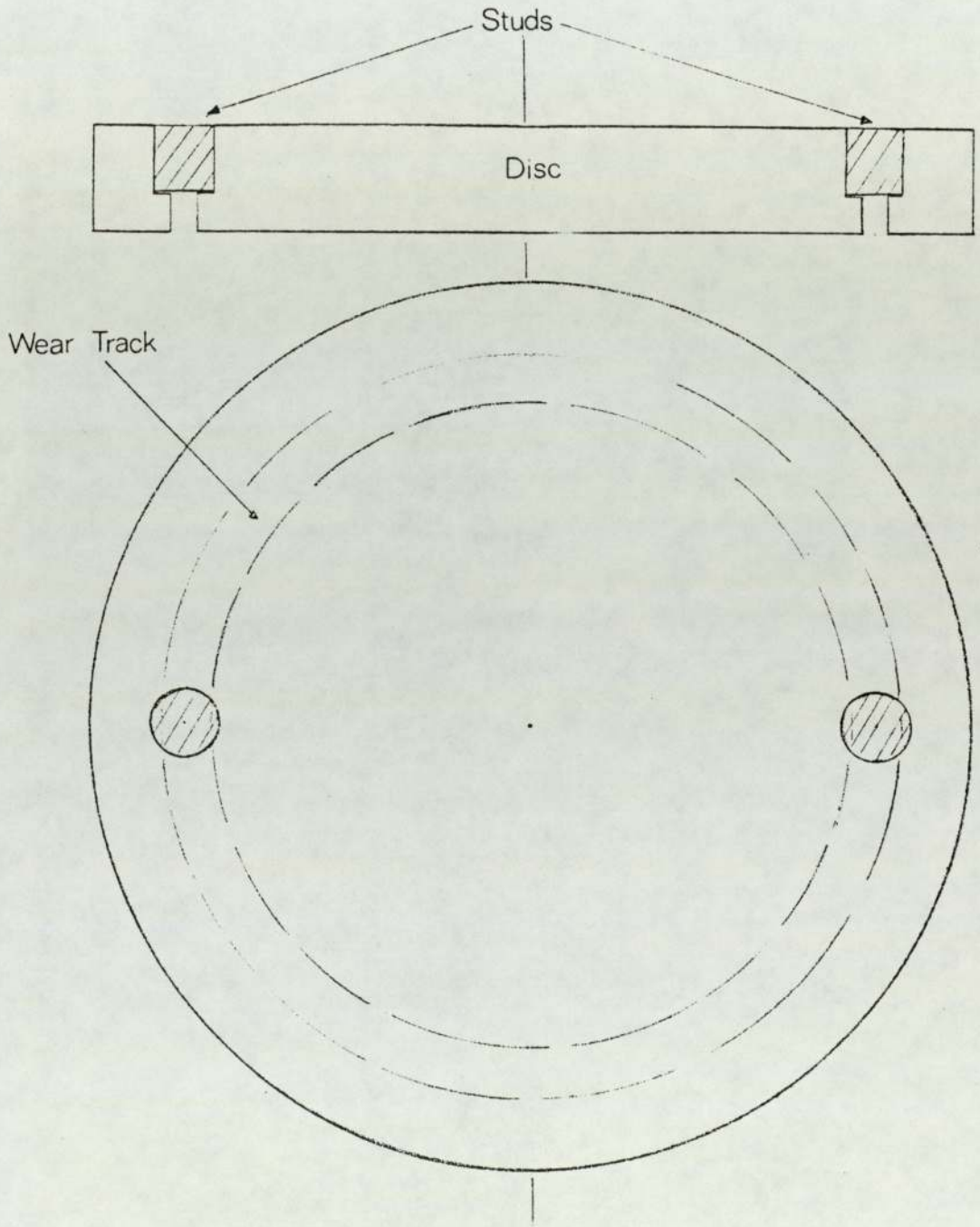

FIGURE 3.4 Studs at Diametrically Opposite Positions in Wear Track.

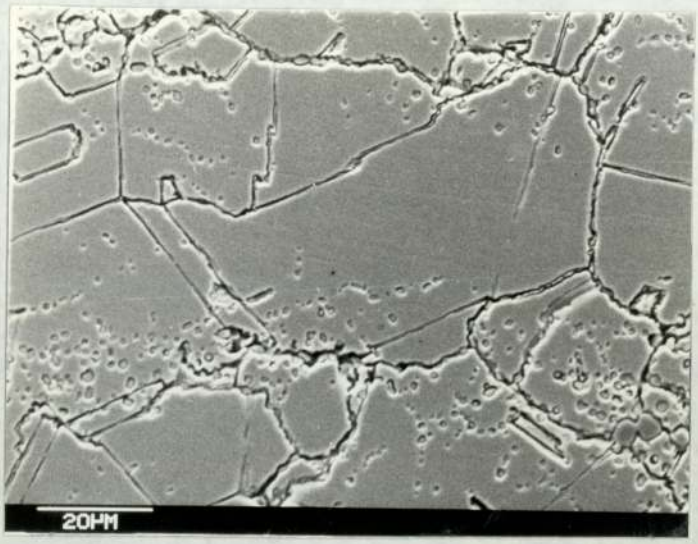

(a)

(b)

FIGURE 3.5 Microstructure of (a) 21 - 4N and (b) Brico 65 .

temperature (both 21 - 4N and Brico 65).

3.6 Wear Tests Without External Heating

In order to establish the wear patterns of Brico 65 sliding on 21 - 4N, experiments were carried out at nominal sliding speeds of 0.23 m/s, 1.00 m/s, 2.0 m/s and 3.3 m/s. The load ranges used for the experiments were:

(i) 12.5 N to 50 N at 0.23 m/s

(ii) 12.5 N to 87.5 N at 1.0 m/s

(iii) 12.5 N to 87.5 N at 2.0 m/s

(iv) 7.0 N to 75 N at 3.3 m/s

Before each wear test the alignment of the pin was checked, to prevent instabilities occurring during the experiment. Operating conditions near the resonant frequency of the machine were avoided. There appeared to be resonance at 500 RPM, corresponding to 3.0 m/s. A sliding speed of 3.3 m/s corresponding to 550 RPM was therefore used.

During each test run the frictional force and the rate of decrease of the pin length with time were monitored continuously using strain gauges and a linear differential voltage transformer (LDVT), respectively. The outputs from these instruments were amplified and then fed to a chart recorder which gave a continuous display of friction and wear with time.

The temperature at known points along the pin (Figure 3.3) were noted at regular internals, along with the disc temperature by means of a multichannel electronic thermometer.

An aluminium tray was used to collect the wear debris. The clockwise rotation of the disc (see Figure 2.3) caused the detached debris particles to fall downwards, into the tray. For the "running-in"

period, the wear debris was collected from the start of the experiment but steady conditions of friction and wear were well established before the wear debris of the equilibrium regime was collected.

3.7 Measurement of Friction and Wear

The torque produced by the friction drag of the rotating disc on the pin caused the instrument arm (Figure 3.1) to exert an upward push on the friction transducer. This caused a displacement of the chart pen, proportional to the magnitude of the friction force.

In Figure 3.1 if x_1 and x_2 are the respective distances of the pin centres and transducer axis from the centre of the moveable shaft, then by the principle of moments:

$$F \times x_1 = P \times x_2$$

where F is the friction force at the pin and P is the pushing force on the transducer. Calibration of the friction transducer was achieved by placing a standard weight (W) on the pin-holder (so that its centre of gravity coincided with the pin axis) and noting the displacement (Y) produced on the chart recorder. The friction channel of the chart recorder was kept on a range of 100 mV, which on the chart paper was equivalent to 200 mm. The calibrations obtained with various standard loads are shown in the table below.

Load at Pin (N)	4.46	8.92	20	44.6
Displacement of Chart Pin (mm)	8	16	36	79.5

Clearly the transducer is linear over the range of loads used. From the results an average calibration of 19.5 N = 34.9 mm was obtained. Thus if y (mm) is the deflection produced by the chart pen then the friction force at the pin is

$$F = (y/34.9) \times 19.5N$$

The LDVT converted the forward displacement of the pin into an electrical signal which was amplified and fed to the second channel of the same chart recorder used to display the friction. Typically, for most experiments a range of 0-10 volts was used, but for experiments where the rate of wear was very low, the 0-1 volt range was used. On each of these ranges the full scale deflection was 200 mm.

The instrument was calibrated using a micrometer. For each range, the calibrations found were:

(i) 168 mm (deflection of pen) = 2.032 mm (displacement at pin) for the 0-10 volt range

(ii) 168 mm (deflection of pen) = 0.2032 mm (displacement at pin) for the 0-1 volt range.

This clearly demonstrated the linearity of the LDVT. For each test run the wear rate of the pin (volume removed per unit sliding distance) was calculated using the expression

$$W_{exp} = \left(\frac{\pi r^2}{V}\right)\left(\frac{2.032 \times 10^{-3}}{168}\right) \times \left(\frac{h}{t}\right)$$, for the 10 volt range (similar expression for the 1 volt-range), where W_{exp} is the wear rate (in m^3/m), r is the pin radius (m), V is the sliding velocity (m/s) and h/t is the slope of the chart trace (in mm/sec - see Figure 4.1).

3.8 Elevated Temperature Experiments

3.8.1 Introduction

To investigate the effect of elevated temperatures on the results obtained from the purely frictionally heated wear tests, and in particular the effect on the two modes of wear encountered at 2 m/s (purely oxidational and metallic / oxidational wear), wear tests were carried out at 2 m/s for nominal disc temperatures of 200°C, 300°C, 400°C and 500°C. Loads of 12.5 N to 100 N were used.

3.8.2 Method of Heating

The disc was heated by means of a modified 2kW cooker element, which was fitted tightly to the back face of the disc. The heating current was controlled by a variac power supply and passed via a two-way slip-ring-brush assembly (Figure 3.2 (c)) to the heater.

In order to reduce heat losses down the main-shaft, an insulating sindanyo block was used as a spacer between the shaft and the disc. This also conveniently carried the thermocouple leads from the silver slip rings to the front face of the disc. To facilitate water cooling of the shaft and bearings, a rotary union, with a stationary centre tube was utilized (see Figure 2.7).

To control the disc temperature to within $10^{\circ}C$ during each test run, the variation of variac power with disc temperature (37) was studied at 334 RPM, corresponding to a linear speed of 2 m/s. The graph obtained is shown in Figure 3.6. From the graph the relationship between the two quantities was found to be

$$T_D = 1.44 P^{.84}$$

where T_D is the excess disc temperature and P the power in watts.

3.8.3 Wear Tests

In a typical experiment, the disc was preheated to a temperature somewhat lower than the required temperature, since the frictional heating would contribute to the overall disc temperature. The magnitude of this contribution was estimated from measurement of the disc temperature for the non-externally heated experiment of the same load and speed.

As in the purely frictionally heated wear tests, the wear debris was collected in an aluminium tray. This was beneficial at these

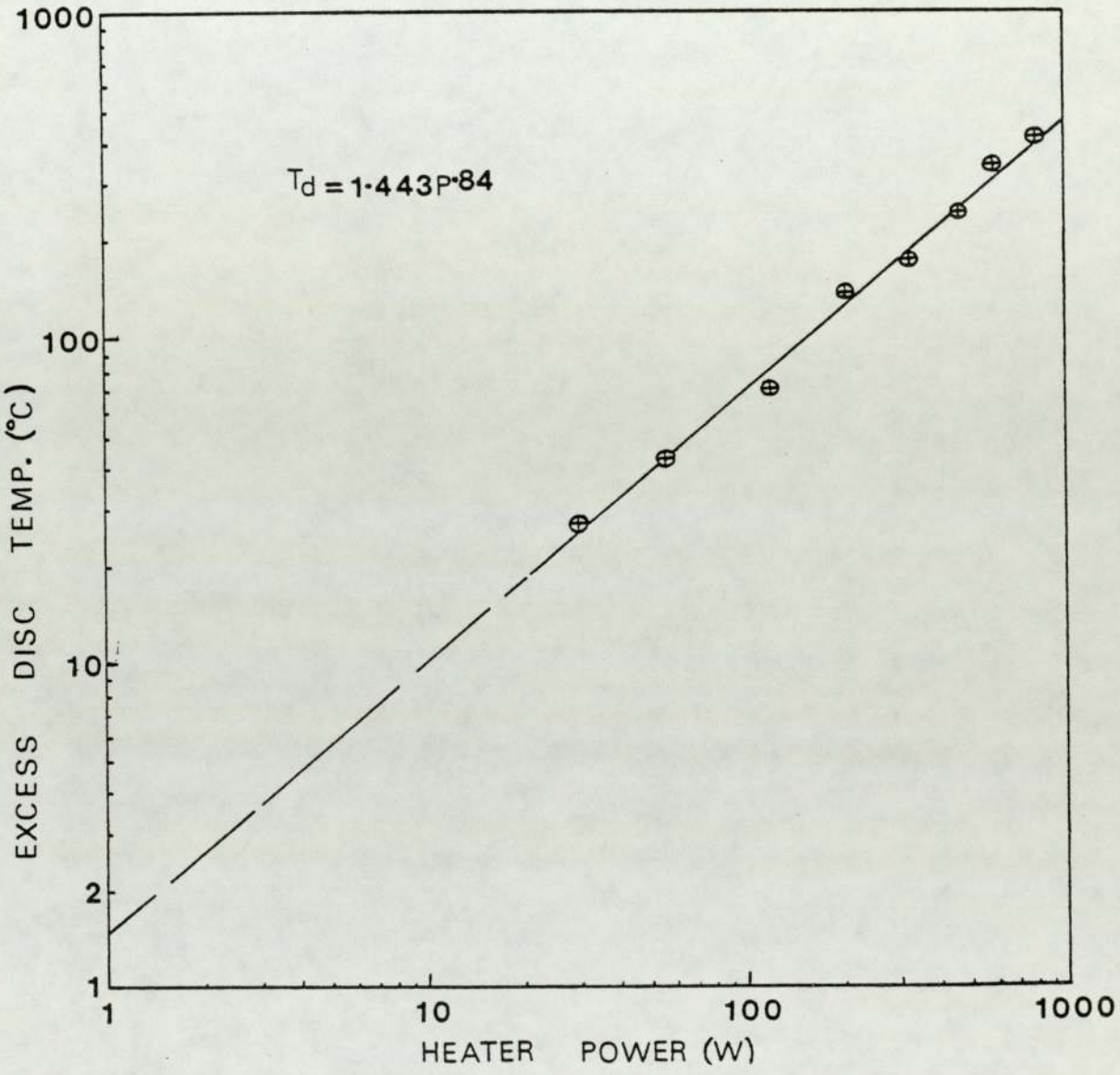

FIGURE 3.6 Variation of Excess Disc Temperature with Heater Power at 334 RPM (2 m/s).

higher temperatures since aluminium has resistive oxidation properties and did not contaminate the debris.

3. 9 Physical Methods of Analysis

3.9.1 Talysurf Profilometry

In order to assess the wear of the disc material, talysurf profiles were taken radially across the wear track. The average peak to trough surface roughness (38) was then computed. Typically, profiles were taken at five different sections across the wear track.

3.9.2 Microhardness Tests

Microhardness measurements were carried out on selected worn specimens using a mini load microhardness tester. Typically, about eight readings were taken over the wear scar, and the average value computed.

3.9.3 Metallographic Taper Sections

In order to examine the morphology within the subsurface layers of the worn specimens, metallographic sectioning of selected samples were carried out. The sample under test was mounted in conductive bakelite and then tapered to the required angle (about 10^{o}). A sample holder which was tapered at 10^{o} was used to hold the mounted specimen. Bakelite material was removed until about $\frac{1}{4}$ of the tapered sample was revealed. The specimen was then diamond polished to a surface finish of 1 μm. Optical microscopy was used for the initial examination. Hardness measurements were taken of the subsurface layers and bulk. The sample was then cleaned and etched using a suitable reagent (alcholic $Fe\,Cl_3$). A more detailed study was carried out using SEM and EDAX.

3.9.4 X-ray Diffraction (XRD) of Wear Debris

X-ray diffraction of the wear debris was carried out using the Debye-Scherrer technique. The debris was placed in a fine capillary tube (0.5 mm in diameter) of non-crystalline glass, and irradiated in a cylindrical powder camera (39, 40) using molybdenum K_α X-rays. The voltage and current settings of the X-ray tube were 40 kV and 20 mA respectively. Typically, exposure times were about two hours, with four minutes to develop the film and ten minutes for fixing.

The use of molybdenum radiation resulted in sharp but closely spaced diffraction lines. However, lines of high d-values (particularly relevant for oxides) were readily obtainable from the pattern. Cobalt K_α radiation was used to resolve the very closely spaced lines. However, the patterns obtained were fairly dull. This was due to the high absorption of cobalt X-rays by the considerable amount of chromium present in the debris.

3.9.5 Glancing Angle XRD of Worn Specimens

Typically, the specimen under investigation was arranged so that the area to be analysed was at the centre of the cylindrical camera. To obtain a sharp glancing angle pattern, it was ensured that when observed through the collimator, the specimen appeared in the top left hand corner of the field of view. This corresponded to a glancing angle (between specimen and beam) of less than 20°.

Cobalt K_α X-rays were used to irradiate the desired area of the specimen, at an X-ray tube setting of 40 kV and 30 mA for thirty minutes. The exposed film was then developed for three minutes, fixed for ten minutes and washed for at least one hour, then dried in an oven. Since the X-rays penetrated less material ($< 200\ \mu m$) compared with the

wear debris (500 μm) there was less absorption and hence the patterns obtained were sharp in comparison with the latter.

3.9.6 Scanning Electron Microscopy (SEM)& Energy Dispersive Analysis by X-rays (EDAX)

(i) Direct Examination of Worn Surfaces

After wear, the surface topographies of the pins and disc inserts were examined using a Scanning Electron Microscope. The EDAX attachment was used to identify the elemental constituents within the surface layers (as far as possible).

In order to measure the thickness of oxide films developed on the surfaces, the tilt correction facility of the instrument was utilized. In a typical investigation, the angle of tilt was adjusted to a fairly high value, say 45°, and the tilt correction was set to the same angle. This unified the magnification over the area of the specimen under study. In regions where the oxide film had fractured leaving near parallel edges, the vertical distance between the edges was measured and converted into microns (using the "bar" in the bottom corner of the micrograph) since the vertical magnification was equal to the horizontal magnification. A number of measurements were taken over each specimen in order to obtain the average oxide film thickness.

(ii) Examination of Wear Debris

The wear debris from selected tests runs was examined by trapping the wear particles within aqueous carbon which was placed on an aluminium stud. Gentle heating (less than 10°C above room temperature) of the stud left the wear particles adhering to a carbon base. The stud was then incorporated into the vacuum chamber of the instrument. EDAX was used to determine the relative proportions of iron and

chromium in the wear debris.

(iii) Examination of Tapered Sections

Selected specimens were carefully examined in order to ascertain whether there were any changes in structure or composition in the subsurface layers of both pin and disc materials during wear. Investigations were carried out before and after etching each specimen.

3.9.7 Auger Analysis

A very selected number of worn specimens were examined using Auger Electron Spectroscopy.

Typically, the sample was argon etched with a beam voltage of 5KV and emission current of 25 mA, for varying times. The relative concentrations of the main elemental constituents (oxygen, iron and chromium) were obtained from the Auger spectra and plotted against etching time.

In addition, the areas in which oxygen rich species were concentrated were examined using the elemental mapping facility of the instrument.

Clearly, the main advantage of using Auger Electron Spectroscopy in preference to EDAX (or as a complimentary technique) is that the amount of oxygen present in the surface layers can be estimated. In addition, the areas where oxygen rich species are concentrated can also be identified using the former technique. In contrast, the characteristic X-ray radiation of the oxygen atom is too low in energy to be detected by EDAX.

CHAPTER 4

EXPERIMENTAL RESULTS

4.1 Introduction

In this chapter the results of the wear tests will first be given, followed by the analysis of the wear debris and the worn specimens.

4.2 Wear Tests Without External Heating

Figure 4.1 shows a typical chart recording of the frictional force variation and the reduction of the pin height versus time. Initially, as the surfaces wore into conformity there was a rapid variation in the frictional force, and the reduction in pin height with time was non-linear. The wear debris consisted of relatively large metallic particles.

4.2.1 Wear Results

(i) Wear Results at 0.23 m/s

To ensure that an equilibrium wear regime was attained, the experimental run time at this slow speed was typically about 24 hours. The resulting wear debris was reddish brown in colour, intermingled with metallic particles. The wear rate was found to be proportional to the applied load as shown in Figure 4.2.

(ii) Wear Results at 1 m/s

After the initial "break-in" period there was a prolonged period of steady severe wear. The duration of this was from about two to four hours, depending on the severity of the load. The wear debris consisted of fine metallic fragments, in comparison to the larger fragments

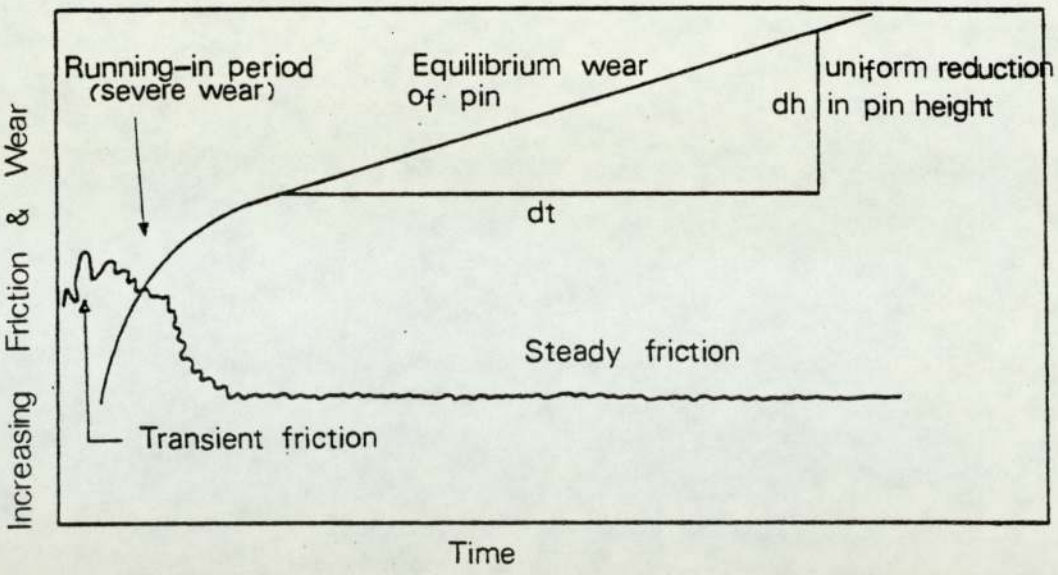

FIGURE 4.1 Variation of Friction and Wear with time (no external heating).

Load (N)	Wear Rate (m^3/m)
12.5	
25.0	5.9×10^{-13}
37.5	17.8×10^{-13}
50.0	37.4×10^{-13}
56.25	70.7×10^{-13}
68.75	138.9×10^{-13}
75.0	104.0×10^{-13}
87.5	817.0×10^{-13}

TABLE 4.1 Severe Wear Rates at 1 m/s .

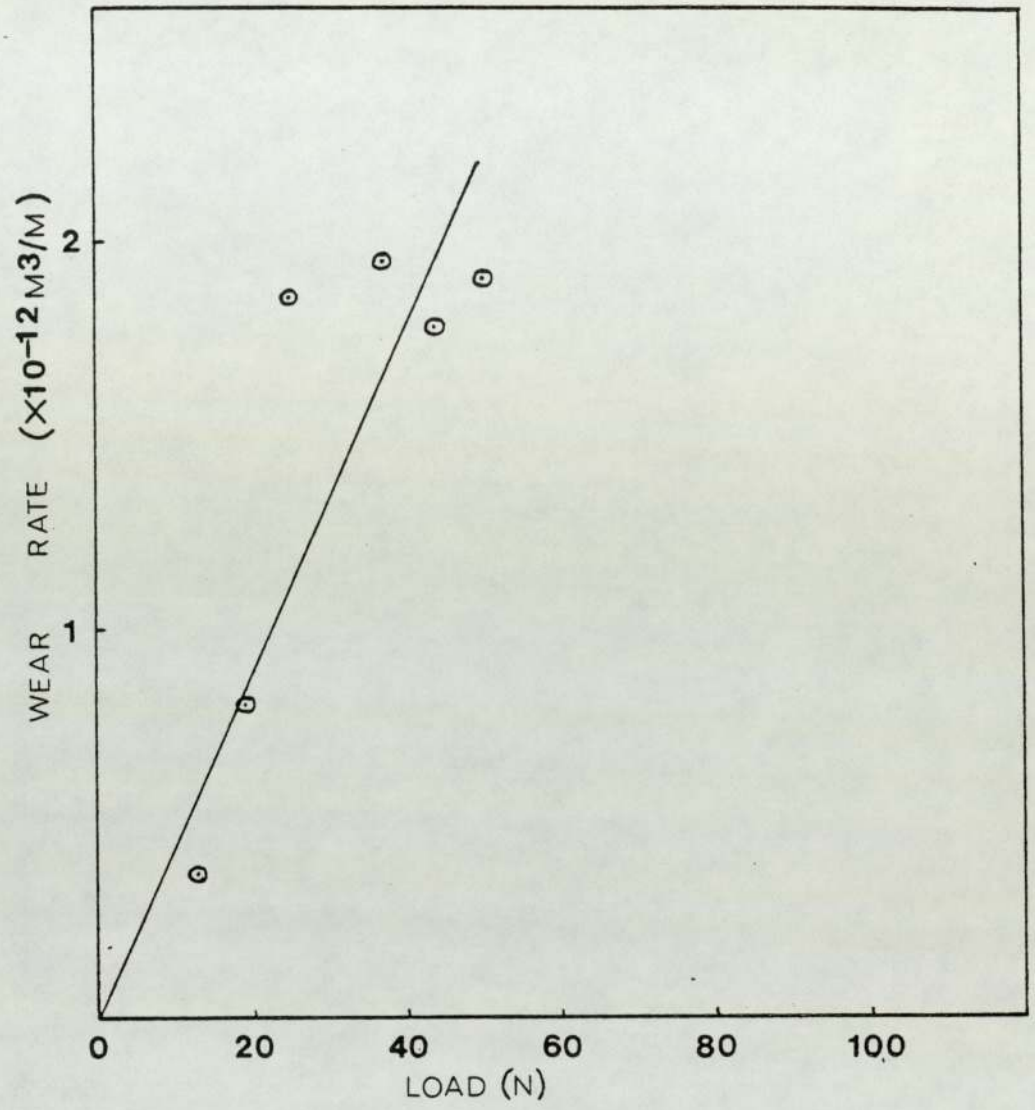

FIGURE 4.2 Equilibrium Wear Rate of Brico 65 (pin) versus Load at 0.23 m/s (no external heating).

observed in the "running-in" period. When the oxide film had become sufficiently thick to protect the surfaces, mild wear ensued and persisted until the end of the experiment. The wear debris was mainly oxide.

The severe wear rates are shown in Table 4.1. A summary of the mild wear results is shown in Figure 4.3. There was a transition at about 60 N, above which there was a moderate increase in the slope of the wear rate versus load graph. Below the transition the wear debris was completely oxide, and above, the debris also contained varying amounts of metallic fragments.

(iii) Wear Results at 2m/s

In comparison to the 1 m/s test runs there was no period of severe wear after "running-in". Once a particular wear regime was established both the friction and wear became steady and remained so throughout the experiment (Figure 4.1).

It is evident from Figure 4.4 that there was a rapid change in wear rate within the load range 67 N - 75 N. As the wear mode changed from predominantly oxidational to mixed metallic/oxidational wear there was a three fold increase in the wear rate.

(iv) Wear Results at 3.3 m/s

For the higher speed experiments a predominantly oxidational wear regime occurred. There was a transitional load at about 60 N. Above this load the slope of the wear rate versus load graph increased marginally (see Figure 4.5).

(v) Effect of Speed

The effect of speed on the wear of Brico 65 for a normal load of 50 N is shown in Figure 4.6. As the speed was increased from 0.23 to 1 m/s there was a large decrease in wear rate (1.9×10^{-12} -

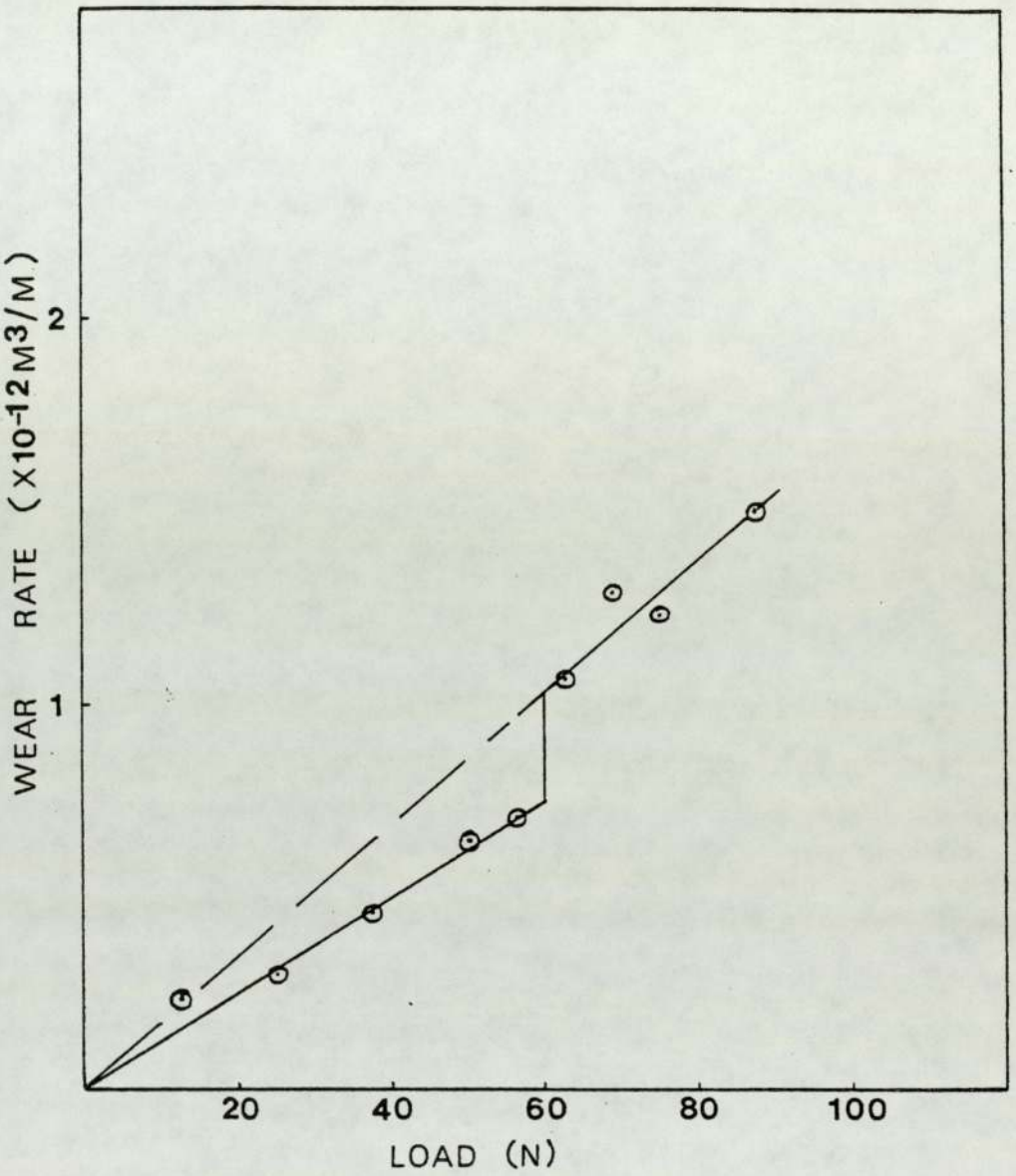

FIGURE 4.3 Equilibrium Wear Rate of Brico 65 (pin) versus Load at 1 m/s (no external heating).

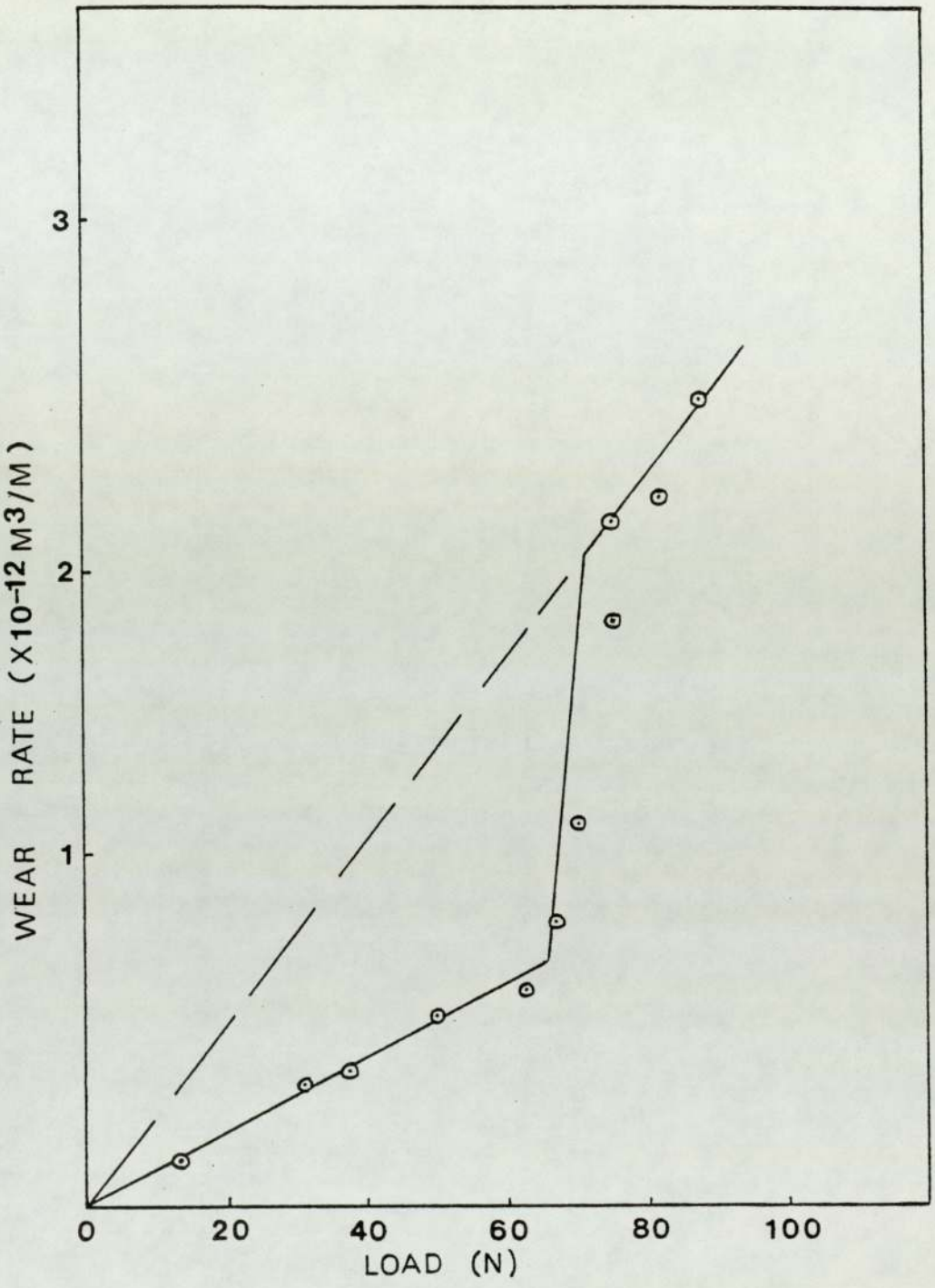

FIGURE 4.4 Equilibrium Wear Rate of Brico 65 (pin) versus Load at 2 m/s (no external heating).

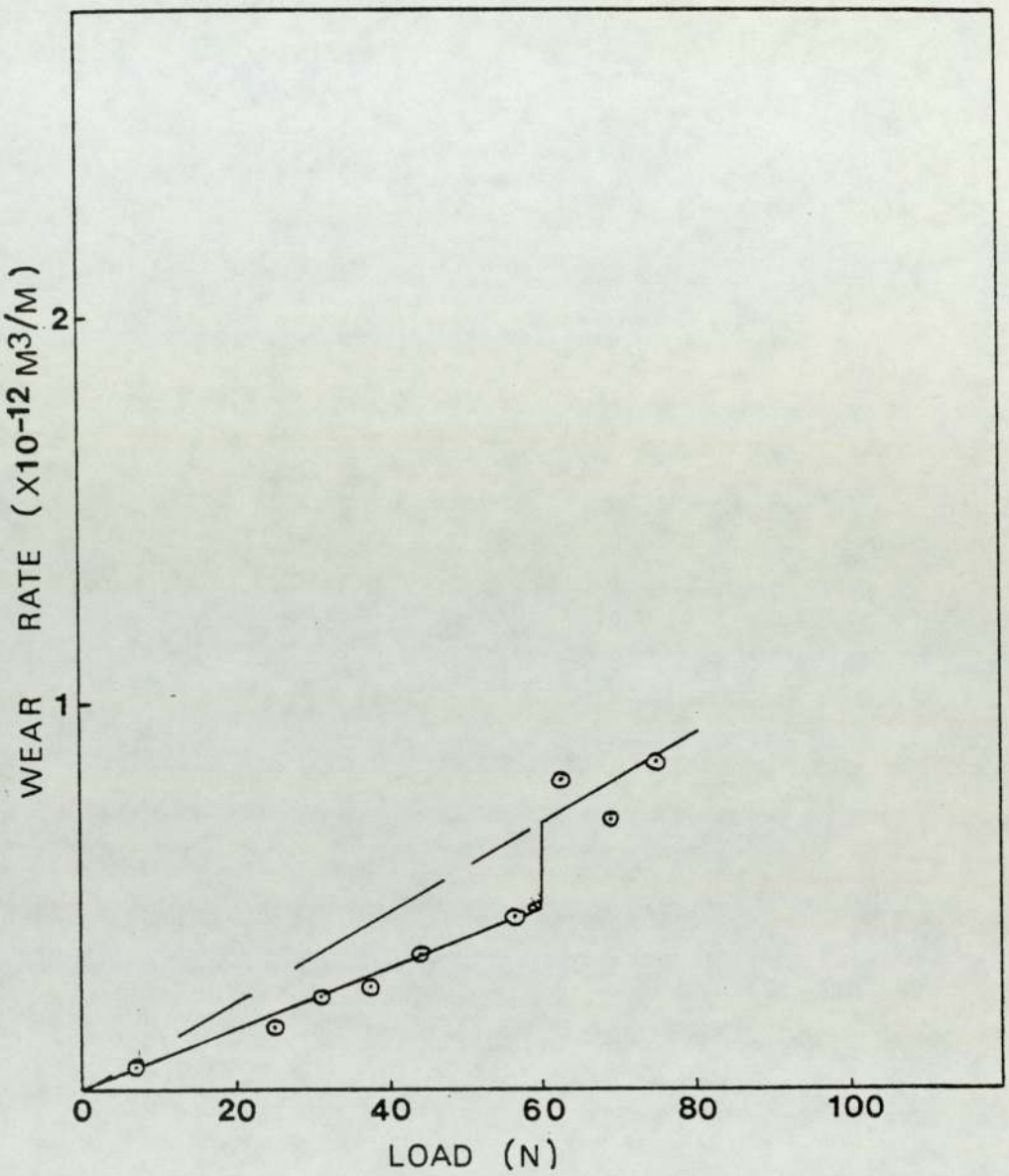

FIGURE 4.5 Equilibrium Wear Rate of Brico 65 (pin) versus Load at 3.3 m/s (no external heating).

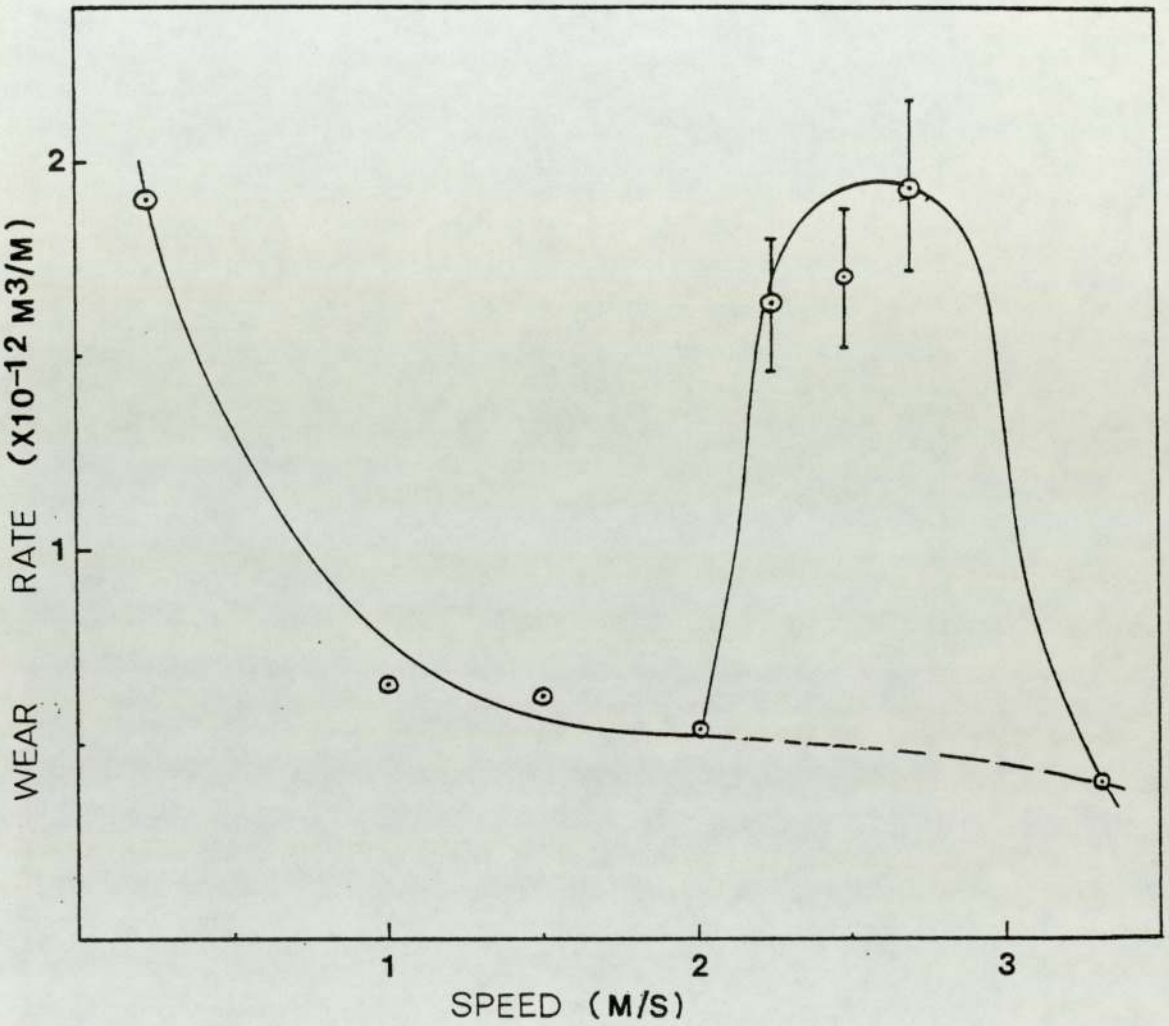

FIGURE 4.6 The Wear Rate of Brico 65 (pin) versus Sliding Speed for a Load of 50N (no external heating).

Speed (m/s)	Wear Coefficient, k ($m^3/m/N$)	
	Below Transition	Above Transition
0.23	4.4×10^{-14}	-
1.00	1.3×10^{-14}	1.7×10^{-14}
2.00	1.1×10^{-14}	2.8×10^{-14}
3.30	0.8×10^{-14}	1.1×10^{-14}

TABLE 4.2 Variation of Wear Coefficient (pin) with speed (no external heating).

Speed (m/s)	Mean Peak to Trough Surface Roughness (μm)	Wear Rate (m^3/m)
0.23	9.5	40.1×10^{-13}
1.00	5.7	5.5×10^{-13}
2.00	2.5	1.7×10^{-13}
3.30	0.73	0.24×10^{-13}

TABLE 4.3 Variation of Disc Wear (no external heating) with speed, at 50N.

6.5×10^{-13} m^3/m) followed by a gradual decrease from 1 to 2 m/s. As the speed was further increased, there was a rapid rise in the wear rate which was a maximum at about 2.7 m/s. Between 2 and 3.3 m/s the wear debris was a mixture of metallic and oxide particles. An increase in the sliding speed to 3.3 m/s caused the wear regime to change back from one of metallic/oxidational to purely oxidational.

(vi) Disc Wear

The average peak to trough surface roughnesses along with the corresponding wear rates are shown in Table 4.3, at various sliding speeds for a normal load of 50 N. In comparison to the pin wear rates (same conditions) the values are lower, except the 0.23 m/s results which gave higher disc wear rates.

4.2.2 Friction Results

The friction results are shown in Figure 4.7. For the low speed experiments the friction coefficient ranged from about 0.67 at 12.5 N to approximately 0.55 at higher loads. As the speed was increased, the variation of μ with load became progressively more gradual. In addition, there was a steady decrease in friction with increasing speed. For a load of 12.5 N μ varied from 0.67 at 0.23 m/s to about 0.33 at 3.3 m/s.

4.2.3 Heat Flow Results

The experimental data for the heat flow measurements are shown in Tables 4.4 (a), (b), (c), and (d). The use of this data to deduce various heat flow parameters will be given in Chapter 5.

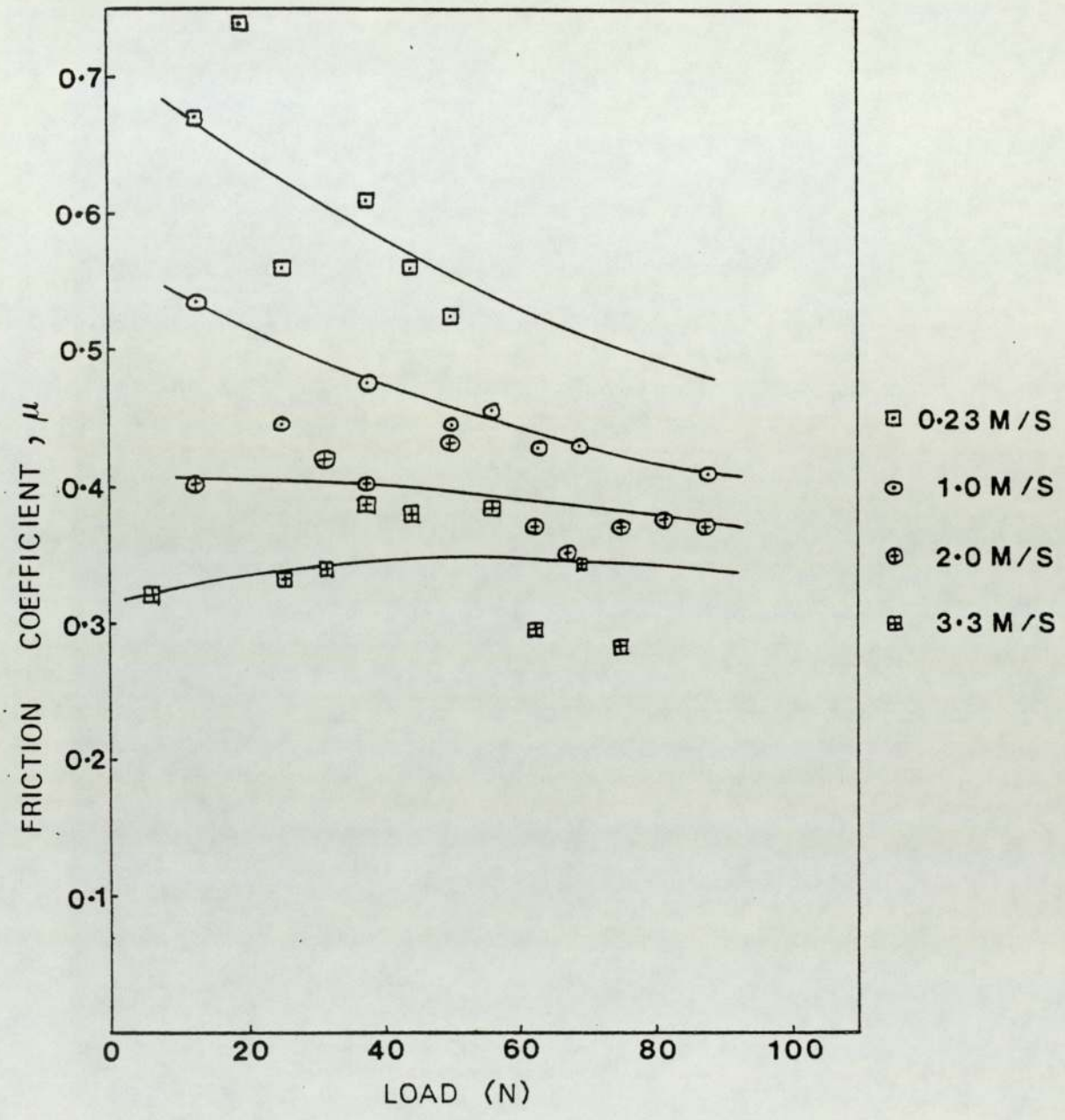

FIGURE 4.7 Friction Coefficient versus Load at various sliding speeds (no external heating).

Load (N)	T_A (°C)	T_B (°C)	T_C (°C)	L_1 (mm)	L_3 (mm)
7.0	37	28	26	5.0	17.0
25.0	87	50	42	3.7	16.9
31.25	92	56	47	5.5	17.0
37.50	120	59	48	3.1	17.1
43.75	142	71	56	3.6	17.6
56.25	144	76	55	7.6	16.7
62.50	155	84	64	7.6	16.5
69.75	184	101	77	7.0	16.8
75.00	195	85	63	5.8	16.9

TABLE 4.4 (a) Heat Flow Data for Brico 65 at 3.3 m/s .

Load (N)	T_A (°C)	T_B (°C)	T_C (°C)	L_1 (mm)	L_3 (mm)
12.50	33	29	28	7.9	15.4
18.75	36	30	28	8.0	15.4
25.00	41	32	31	8.3	15.1
37.50	42	31	28	5.5	15.6
43.75	46	34	31	6.8	16.0
50.00	42	34	32	7.9	15.0

TABLE 4.4 (b) Heat Flow Data for Brico 65 at 0.23 m/s .

Load (N)	T_A (°C)	T_B (°C)	T_C (°C)	L_1 (mm)	L_3 (mm)
12.50	48	34.5	32	7.9	16.5
31.25	92	50	39	7.0	16.5
37.50	75	44	39	9.6	17.1
50.00	115	69	51	8.0	16.0
62.50	143	73	61	8.0	18.0
67.00	156	71	58	5.5	18.0
75.00	220	88	79	3.0	18.0
81.25	227	97	77	4.0	18.0
87.50	240	101	89	3.5	18.0

TABLE 4.4 (c) Heat Flow Data for Brico 65 at 2 m/s .

Load (N)	T_A (°C)	T_B (°C)	T_C (°C)	L_1 (mm)	L_3 (mm)
12.50	44	35	31	7.5	15.2
25.00	56	36	31	9.6	15.6
37.50	65	48	41	11.2	16.5
50.00	77	46	35	8.9	17.4
56.25	80	48	40	11.2	15.2
62.50	97	60	53	6.8	15.8
68.75	98	66	51	7.3	16.4
75.00	130	87	68	7.8	16.3

TABLE 4.4 (d) Heat Flow Data for Brico 65 at 1 m/s .

4.3 Elevated Temperature Wear Tests

The typical variation of friction and wear with time is shown in Figure 4.8. During the initial period of the experiment the wear of the pin was negative, due to thermal expansion. This period naturally increased as the ambient disc temperature was increased. To allow for expansion, under mild wear conditions the experimental run time was at least six hours. Under severe wear conditions the run time was about four hours.

4.3.1 Wear Results

(i) Wear Results at 200°C

There was a transition from mild to severe wear at a load of about 44 N. Above this load the wear rate increased by an order of magnitude. At 43.75 N the wear rate was about 10^{-12} m^3/m and at 50 N the value was $10^{-11} m^3/m$ (see Figure 4.9). The resulting wear debris was a mixture of metallic and oxide fragments. However, certain oxides indicative of "mild" oxidational wear were absent from the wear debris and the pin surface. In addition, the pin surface appeared bluish grey in colour and deep grooving of the surface layers was clearly visible with the naked eye.

In comparison, below the transition the surface grooves were absent from the pin. Numerous oxide islands were present in the surface and the wear debris was predominantly oxide.

(ii) Wear Results at 300°C, 400°C and 500°C

For these higher temperature experiments a mild form of oxidational wear occurred for all loads. The wear debris was completely oxide. On initial inspection of the pin and disc surfaces, both appeared to be covered with an appreciable layer of protective oxide. The results

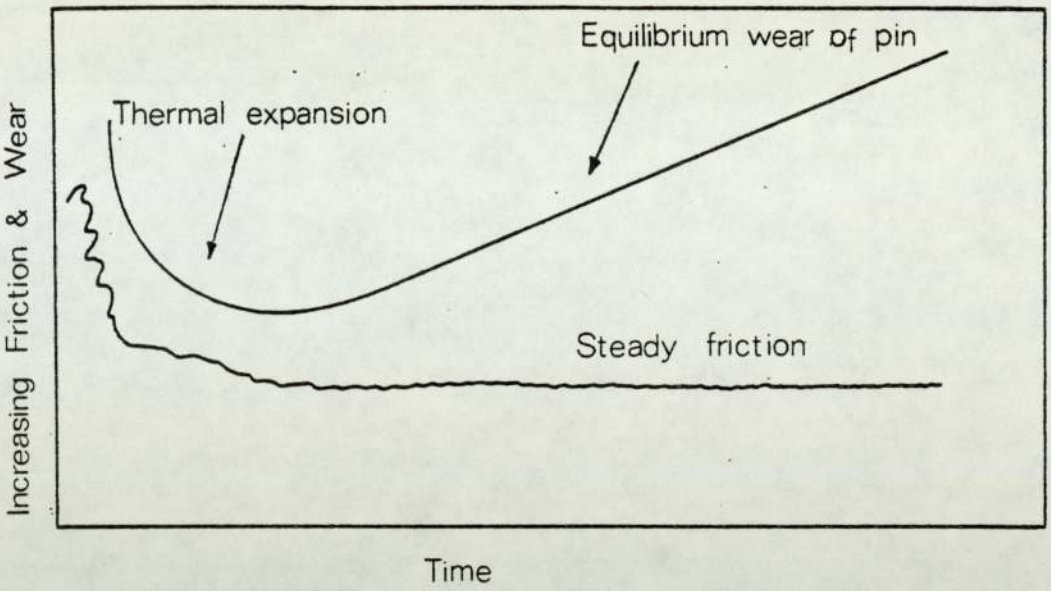

FIGURE 4.8 Variation of Friction and Wear with Time at Elevated Temperatures.

DISC TEMPERATURE (°C)	Specific Wear Rate ($m^3 m^{-1} N^{-1}$)	
	Below Transition	Above Transition
200	1.0×10^{-14}	19.7×10^{-14}
300	0.5×10^{-14}	-
400	0.55×10^{-14}	-
500	0.78×10^{-14}	-

TABLE 4.5 Variation of Specific Wear Rate with Temperature (2 m/s).

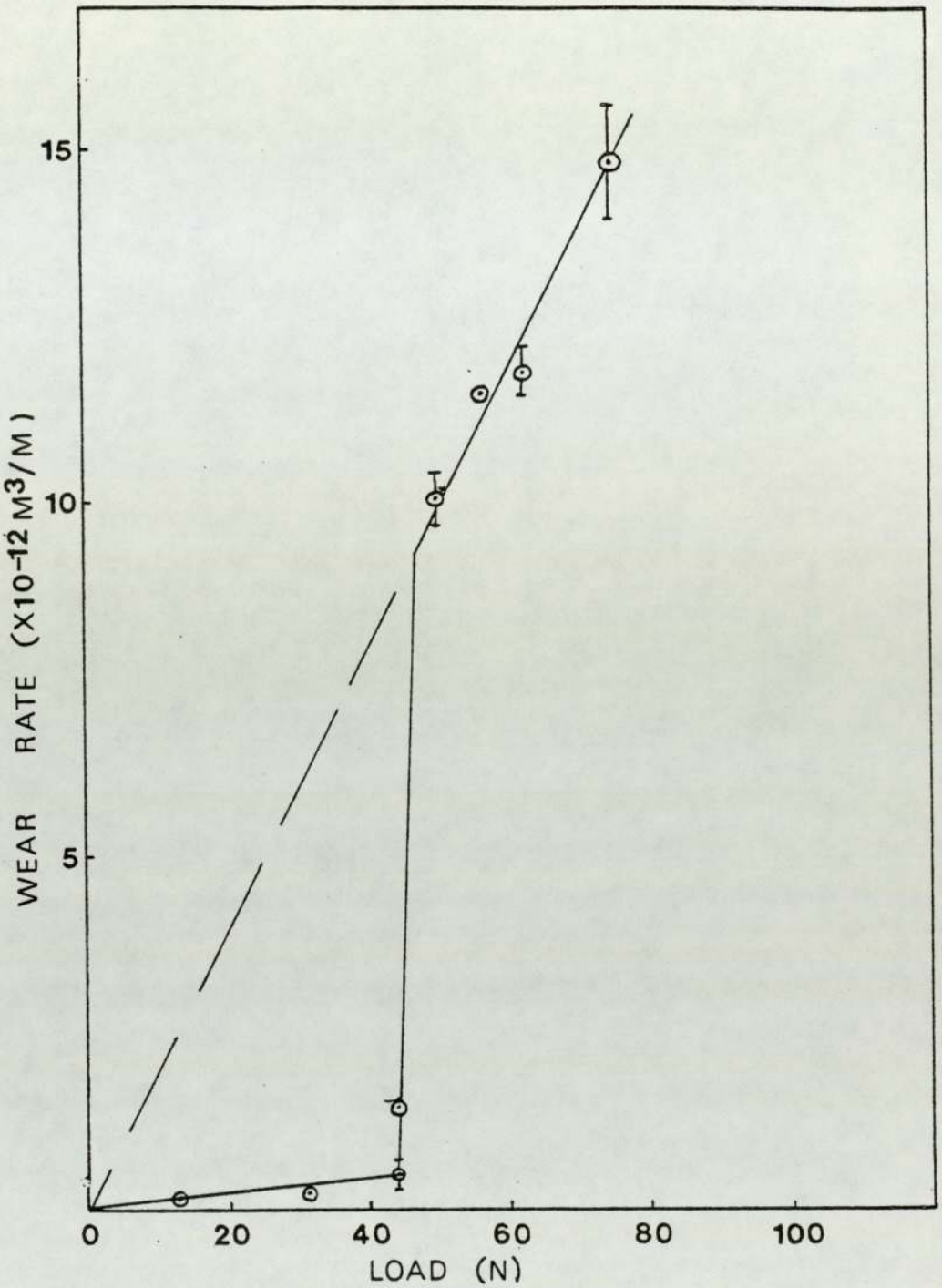

FIGURE 4.9 Equilibrium Wear Rate versus Load at a Disc Temperature of 200°C (2 m/s sliding speed).

are shown in Figure 4.10.

(iii) Effect of External Heating

The specific wear rates with the corresponding disc temperatures are shown in Table 4.5. As the electrical heat input to the disc was increased the transition at 200°C was completely supressed. There was also a decrease in the mild wear rates as the disc was elevated from 200°C to higher temperatures, followed by moderate increases at 500°C. This was presumably due to thermal softening at the higher pin surface temperatures.

(iv) Disc Wear

Under mild wear conditions, the wear rate of the disc, although lower than that of the pin, was comparable in magnitude. In the case of the test runs above the transition, at a disc temperature of 200°C, the wear rates differed by more than an order of magnitude. Talysurf profiles of the wear track for various sliding conditions are shown in Figure 4.11. The disc and corresponding pin wear rates are shown in Table 4.6.

4.3.2 Friction Results

There was a similar variation in the friction coefficient (μ) with load, at elevated temperatures. For these high temperature experiments, μ varied from about 0.4 at low loads to approximately 0.3 at higher loads (see Figure 4.12). In comparison to the wear results, friction appears to be less sensitive to surface changes.

4.3.3 Heat Flow Results

The heat flow data for the elevated temperature experiments are shown in Tables 4.7 (a), (b), (c), and (d). A

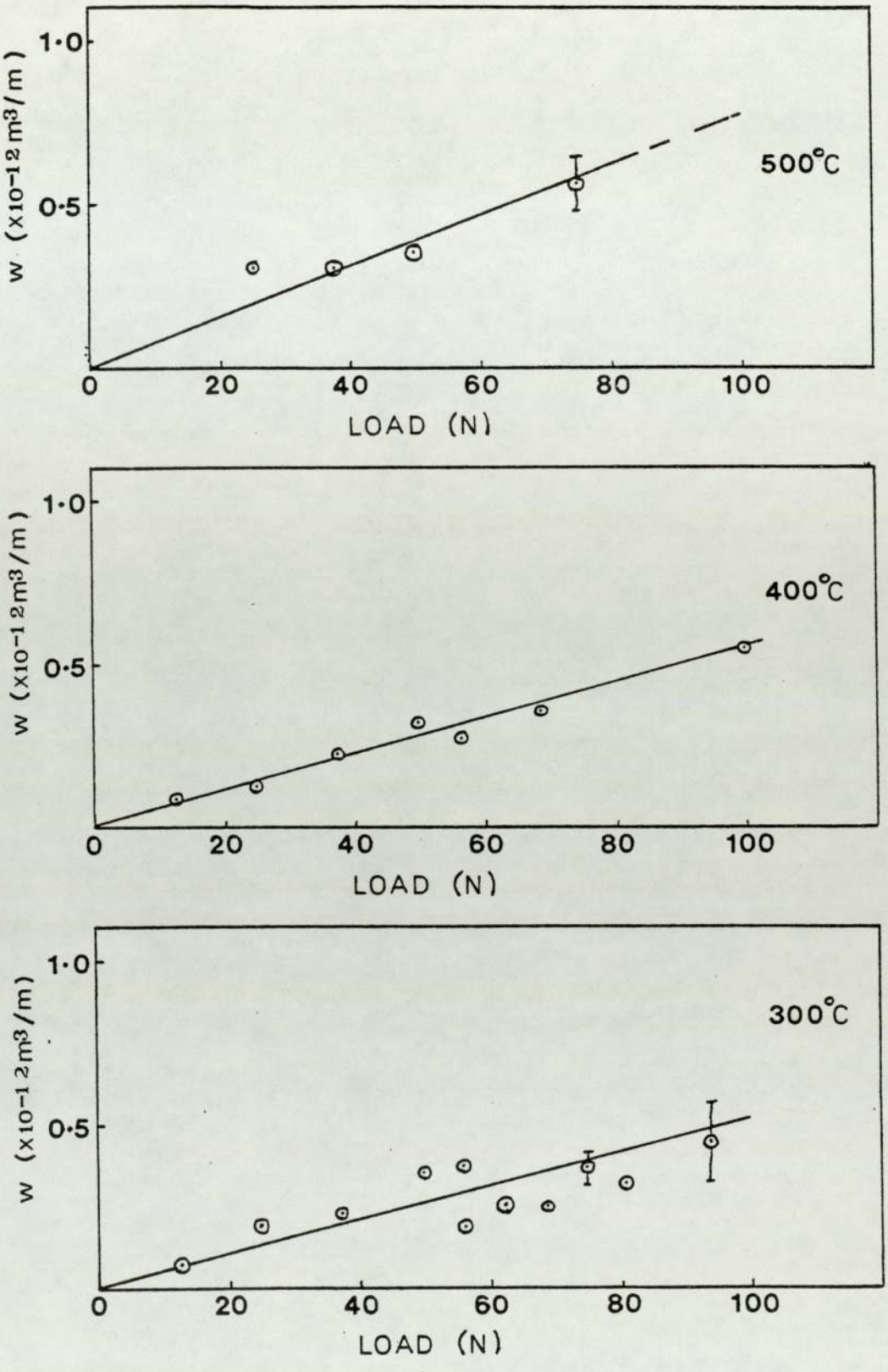

FIGURE 4.10 Equilibrium Wear Rate of Pin versus Load at various Disc Temperatures (2 m/s sliding speed).

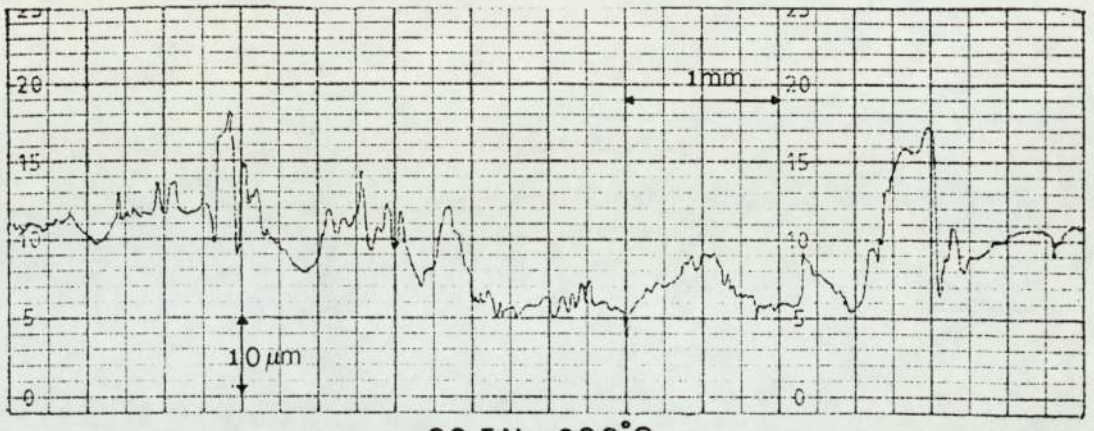

62·5N 200°C

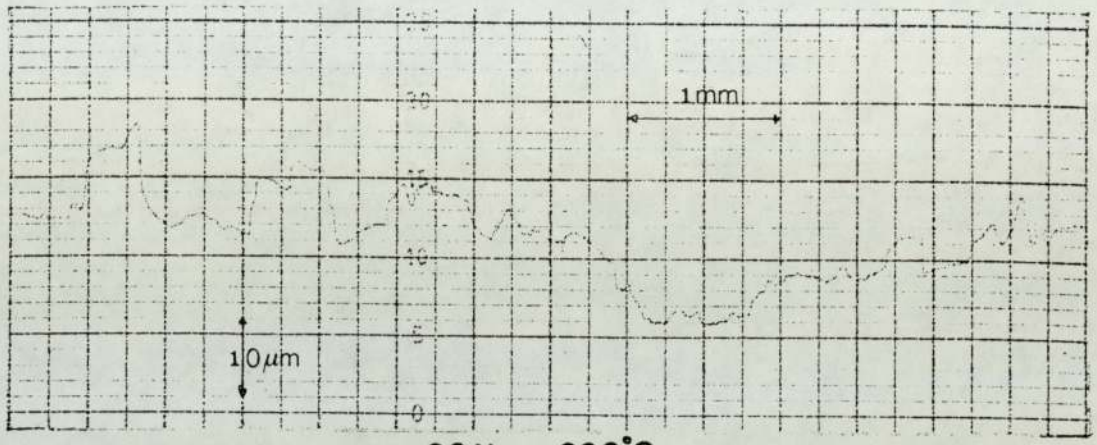

69N 300°C

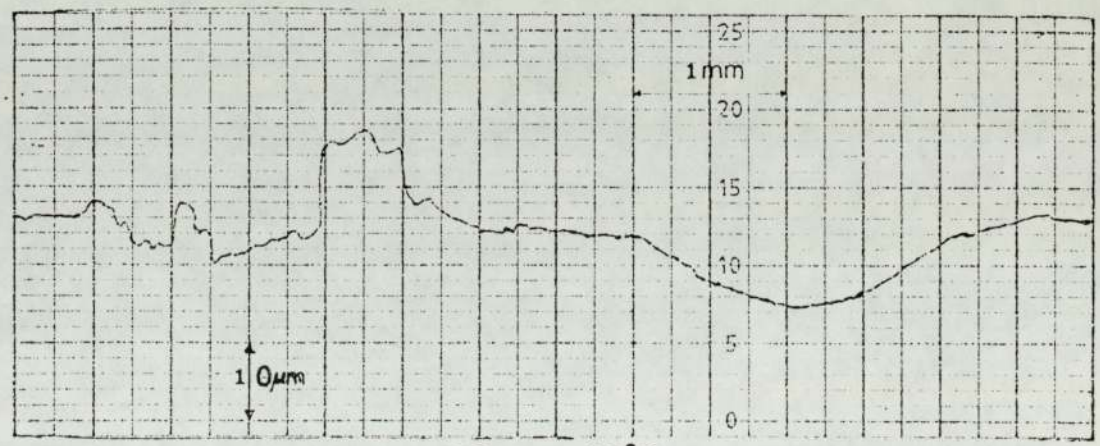

100N 400°C

FIGURE 4.11 Talysurf Profiles of Disc Wear Track for various sliding conditions (2 m/s sliding speed).

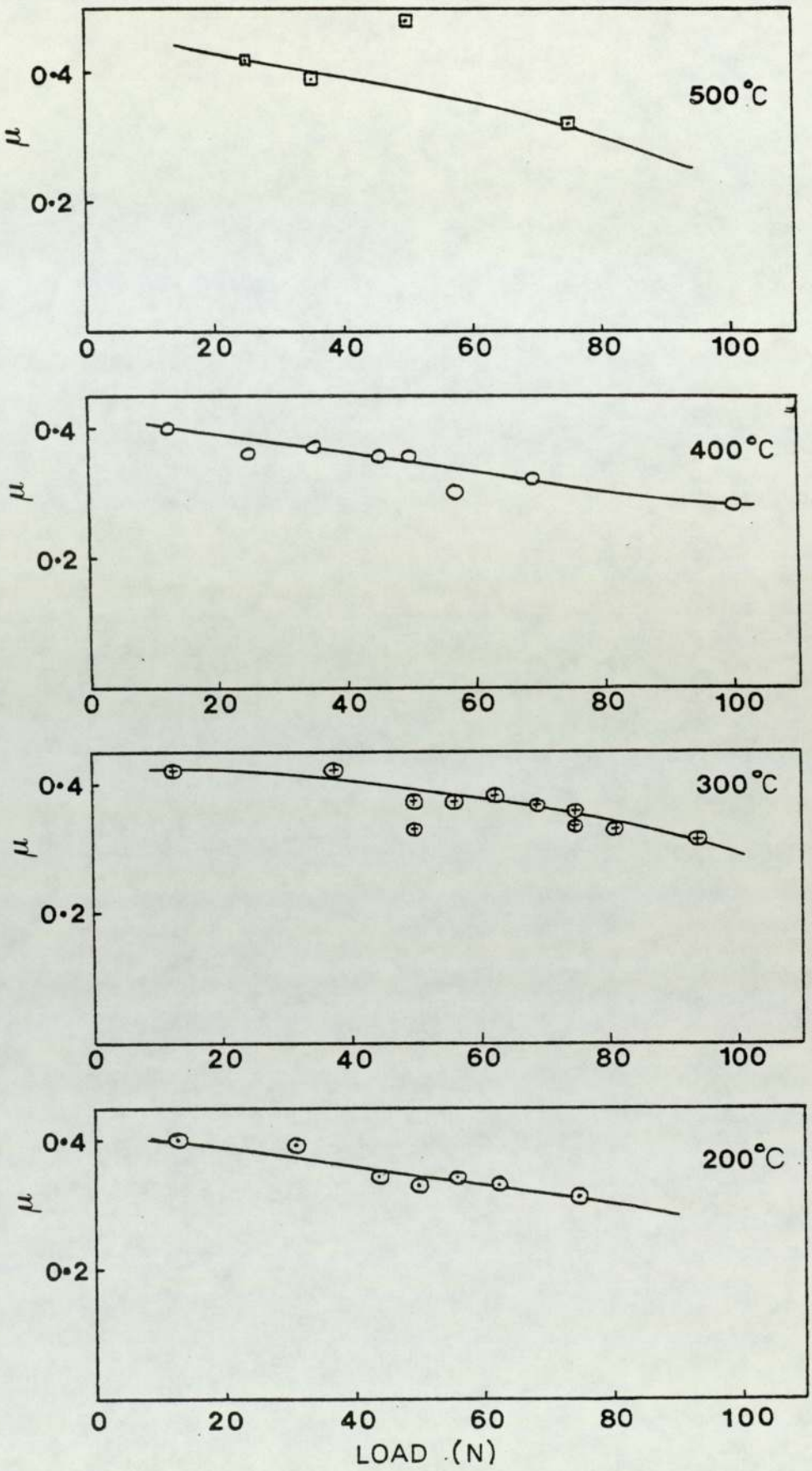

FIGURE 4.12 Friction Coefficient versus Load at various Disc Temperatures for a sliding speed of 2 m/s .

DISC TEMPERATURE (°C)	Load (N)	Disc Wear Rate (m^3/m)	Pin Wear Rate (m^3/m)
200	62.5	2.5×10^{-13}	146×10^{-13}
300	68.75	1.4×10^{-13}	2.4×10^{-13}
400	100	4.5×10^{-13}	5.4×10^{-13}

Table 4.6 Pin and Disc Wear at Elevated Temperatures .

Load (N)	T_A (°C)	T_B (°C)	T_C (°C)	L_1 (mm)	L_3 (mm)
12.50	205	104	80	7.7	17.0
31.25	231	101	85	4.9	15.5
43.75	218	104	80	9.3	15.9
50.00	343	170	127	4.8	15.7
56.25	337	133	102	5.1	17.3
62.50	320	145	100	7.2	16.3
75.00	380	175	117	4.0	16.5

Table 4.7 (a) Heat Flow Data for Brico 65 (Pin) at a Disc Temperature of 200°C .

Load (N)	T_A (°C)	T_B (°C)	T_C (°C)	L_1 (mm)	L_3 (mm)
12.5	232	122	91	9.7	15.2
25.0	291	141	112	4.7	17.6
37.5	306	148	96	5.6	17.5
50.0	319	169	132	6.0	15.5
50.0	343	170	127	4.8	15.7
56.25	259	119	96	11.2	15.7
62.5	318	154	111	4.7	17.5
62.5	320	145	100	7.2	16.3
68.75	315	152	111	6.8	17.3
75.0	247	116	94	11.8	15.6
81.25	314	150	95	8.0	15.0
93.75	309	151	111	9.0	17.2

Table 4.7 (b) Heat Flow Data for Brico 65 (Pin) at a Disc Temperature of 300°C.

Load (N)	T_A (°C)	T_B (°C)	T_C (°C)	L_1 (mm)	L_3 (mm)
12.5	345	171	125	5.3	16.2
25.0	364	210	157	5.8	14.6
37.5	355	167	121	7.4	16.3
50.0	305	138	96	11.2	16.9
56.25	366	209	149	6.6	14.6
68.75	382	205	145	6.1	15.3
100.0	426	222	158	5.5	15.3

Table 4.7 (c) Heat Flow Data for Brico 65 (Pin) at a Disc Temperature of 400°C.

Load (N)	T_A (°C)	T_B (°C)	T_C (°C)	L_1 (mm)	L_3 (mm)
25.0	436	267	214	8.8	17.0
37.5	470	281	224	8.2	16.7
50.0	502	294	230	8.3	16.6
75.0	498	271	220	8.0	16.8

Table 4.7 (d) Heat Flow Data for Brico 65 (Pin) at a Disc Temperature of 500°C.

detailed description of the temperature measurements was given in Section 3.4. The use of the data to deduce parameters such as the bulk surface pin temperature will be given in greater detail in Chapter 5.

4.4 X-Ray Diffraction Analysis of the Wear Debris

In general, the wear debris can be of three types: (1) Purely metallic in form, (2) purely of oxide form, or (3) of a mixed metallic and oxide form.

While the metallic debris is readily identified by X-ray diffraction, the identification of oxide debris, particularly of Fe - Cr alloys, is much more difficult. Such difficulties are due to the continuous range of solid solutions obtainable between Fe and Cr oxides within their rhombohedral, spinel and wustite phases (41).

The rhombohedral oxide phase can exist as a solid solution of Cr_2O_3 and α—Fe_2O_3 (designated as $(Cr, Fe)_2\ O_3$). The most difficult of the oxide phases to identify is the spinel phase (42) which has a complex structural arrangement, of the general form $Fe\ Fe_{(2\ -\ x)}\ Cr_xO_4$ where $0 \leqq x \leqq 2$. For high Cr ($\geqq$ 20%) steels the wustite phase rarely exists as a stable entity. In fact, reflections corresponding to this phase were never detected in the X-ray powder patterns.

In this section the analyses of the wear debris is described in relation to the mild and severe wear regimes.

4.4.1 Analysis for Wear Tests Without External Heating

Typical analyses of the various types of wear debris uncountered under these conditions of sliding are given in Tables 4.8

Intensity	2θ (degrees)	d (A^o)	Possible Identity		
	11.25	3.63	$(Fe,Cr)_2O_3$		
*	15.3	2.67	$(Fe,Cr)_2O_3$		
*	16.25	2.50	$(Fe,Cr)_2O_3$		
*	19.8	2.08		austenite	
***	20.1	2.04			Ferrite
	22.5	1.82	$(Fe,Cr)_2O_3$	austenite	
	24.3	1.68	$(Fe,Cr)_2O_3$		
	28.4	1.43			Ferrite
	32.25	1.27		austenite	
**	35.5	1.17			Ferrite
	46.0	0.91			Ferrite

Table 4.8 (a) Powder diffraction pattern for Brico 65 sliding on on 21 - 4 N at 0.23 m/s and 18.75 N. (Mo K_α radiation, λ = 0.7107 A^o)

*** very strong intensity
** strong intensity
* fairly strong intensity

Intensity	2 θ (degrees)	d (A^o)	Possible Identity	
*	8.5	4.80		$FeFe_{(2-x)}Cr_xO_4$
*	11.25	3.63	$(Fe,Cr)_2O_3$	
*	13.75	2.97		$FeFe_{(2-x)}Cr_xO_4$
*	15.3	2.67	$(Fe,Cr)_2O_3$	
***	16.25	2.51	$(Fe,Cr)_2O_3$	$FeFe_{(2-x)}Cr_xO_4$
*	19.6	2.09		$FeFe_{(2-x)}Cr_xO_4$
*	22.3	1.84	$(Fe,Cr)_2O_3$	
*	24.3	1.69	$(Fe,Cr)_2O_3$	
*	25.5	1.61		$FeFe_{(2-x)}Cr_xO_4$
**	27.75	1.48	$(Fe,Cr)_2O_3$	$FeFe_{(2-x)}Cr_xO_4$
*	28.4	1.43	$(Fe,Cr)_2O_3$	
*	32.3	1.28		$FeFe_{(2-x)}Cr_xO_4$
*	38.1	1.09		$FeFe_{(2-x)}Cr_xO_4$
	39.8	1.04		$FeFe_{(2-x)}Cr_xO_4$
	43.25	0.96		$FeFe_{(2-x)}Cr_xO_4$

TABLE 4.8 (b) Powder diffraction pattern for Brico 65 sliding on 21 - 4N at 2 m/s and 12.5N.
($Mo\ K_\alpha$ radiation, $\lambda = 0.7107A^o$)

Intensity	2θ (degrees)	d $(A)^{\circ}$	Possible Identity		
	13.8	2.96			$FeFe_{(2-x)}Cr_xO_4$
*	16.2	2.52			$FeFe_{(2-x)}Cr_xO_4$
***	19.7	2.08	austenite		$FeFe_{(2-x)}Cr_xO_4$
*	20.1	2.04		Ferrite	
**	22.7	1.80	austenite		
	25.5	1.61			$FeFe_{(2-x)}Cr_xO_4$
	27.8	1.48			$FeFe_{(2-x)}Cr_xO_4$
*	32.5	1.27	austenite		$FeFe_{(2-x)}Cr_xO_4$
	35.5	1.17		Ferrite	
	38.25	1.08	austenite		$FeFe_{(2-x)}Cr_xO_4$
	39.9	1.04	austenite		$FeFe_{(2-x)}Cr_xO_4$
	46.3	.90	austenite		
	50.8	.83		Ferrite	

TABLE 4.8 (c) Powder diffraction pattern for Brico 65 sliding on 21 - 4N at 2 m/s and 75N.
(Mo K_α radiation, λ = 0.7107A°)

Intensity	2θ (degrees)	d (A°)	Possible Identity		
	11.25	3.63	$(Fe,Cr)_2O_3$		
	13.8	2.96			$FeFe_{(2-x)}Cr_xO_4$
	15.3	2.67	$(Fe,Cr)_2O_3$		
**	16.2	2.52	$(Fe,Cr)_2O_3$		$FeFe_{(2-x)}Cr_xO_4$
*	19.7	2.08	Austenite		$FeFe_{(2-x)}Cr_xO_4$
***	20.1	2.04		Ferrite	
*	22.7	1.80	Austenite		
	22.3	1.84	$(Fe,Cr)_2O_3$		
	24.3	1.69	$(Fe,Cr)_2O_3$		
	25.5	1.61			$FeFe_{(2-x)}Cr_xO_4$
*	27.75	1.48	$(Fe,Cr)_2O_3$		$FeFe_{(2-x)}Cr_xO_4$
*	35.5	1.17		Ferrite	
*	38.25	1.08	Austenite		$FeFe_{(2-x)}Cr_xO_4$
	46.0	0.91		Ferrite	

TABLE 4.8 (d) Powder diffraction pattern for Brico 65 sliding on 21 - 4N at 1 m/s and 68.75N (Mo K_α radiation, λ = 0.7107 A°).

Intensity	2θ (degrees)	d (A^o)	Possible Identity		
	13.75	2.97			$FeFe_{(2-x)}Cr_xO_4$
f	15.3	2.67	$(Fe,Cr)_2O_3$		
***	16.25	2.51			$FeFe_{(2-x)}Cr_xO_4$
	19.6	2.09			$FeFe_{(2-x)}Cr_xO_4$
**	20.1	2.04		Ferrite	
f	24.3	1.69	$(Fe,Cr)_2O_3$		
**	25.5	1.61			$FeFe_{(2-x)}Cr_xO_4$
**	27.75	1.48			$FeFe_{(2-x)}Cr_xO_4$
	32.3	1.28			$FeFe_{(2-x)}Cr_xO_4$
	35.5	1.17		Ferrite	
	38.25	1.08			$FeFe_{(2-x)}Cr_xO_4$
	39.8	1.04			$FeFe_{(2-x)}Cr_xO_4$
	43.25	0.96			$FeFe_{(2-x)}Cr_xO_4$
	46.0	0.91		Ferrite	

TABLE 4.8 (e) Powder diffraction pattern for Brico 65 sliding on 21 - 4N at 3.3 m/s and 62.5N. (Mo K_α , λ = 0.7107 A^o)

(a), (b), (c), (d) and (e), in which the interplanar spacings, d, were identified from the various angles of reflection on the X-ray film. The ASTM index (43, 44) was used to correlate the measured 'd' values with particular oxide and metallic species.

A summary of the types of debris found for the various experimental conditions is given in Table 4.9.

(i) Wear Debris at 0.23 m/s

For this low speed of sliding the constituents of the wear debris were found to be ferrite (α-(Fe,Cr)),austenite (γ-(Fe,Cr)) with varying amounts of the rhombohedral oxide ($(Fe,Cr)_2O_3$). The proportions of the metallic constituents increased with load. The occurence of the rhombohedral phase is not surprising since this is the oxide phase most likely to be formed at the lower temperatures.

(ii) Mild Wear Debris

In the case of the higher sliding speeds the debris was found to be almost completely oxide (Table 4.8 (b)) with the major constituents being the rhombohedral and spinel oxide phases of iron and chromium. It is possible that the other alloying elements also formed oxides but due to their lower concentration levels, they were not detected. However, one would envisage that these elements would yield similar oxide phases as Fe and Cr.

The proportion of the spinel phase appeared to increase with speed and load (see Table 4.8 (e)).

(iii) Metallic / Oxide Debris

Above the transition load, varying amounts of ferrite, austenite, spinel oxide and to a lesser extent the rhombohedral oxide phase were detected.

Debris Constituents	Experimental Conditions
Ferrite, austenite, $(Fe,Cr)_2O_3$	All runs at 0.23 m/s
$(Fe,Cr)_2O_3$, $FeFe_{(2-x)}Cr_xO_4$	1 m/s, 2m/s, 3.3 m/s - all loads below transition.
Austenite, ferrite, $FeFe_{(2-x)}Cr_xO_4$	2 m/s - loads above transition. (2.25 m/s - 50N), (2.47 m/s - 50N)
Ferrite, $(Fe,Cr)_2O_3$, $FeFe_{(2-x)}Cr_xO_4$ austenite	1 m/s at all loads above transition .
$FeFe_{(2-x)}Cr_xO_4$, Ferrite	3.3 m/s - above transition

TABLE 4.9 Types of Wear Debris found under various sliding conditions. (no external heating).

Debris Constituents	Experimental Conditions
$(Fe,Cr)_2O_3$, $FeFe_{(2-x)}Cr_xO_4$	200°C (all loads below transition) 300°C, 400°C and 500°C at all loads.
Austenite, ferrite, $FeFe_{(2-x)}Cr_xO_4$	200°C - above transition

TABLE 4.10 Types of wear Debris found at Elevated Temperatures.

In comparison, the height of the transitions at 1 m/s and 3.3 m/s are less significant than the sudden increase in wear rate at 2 m/s. In fact, analysis of the wear debris for experiments above the transition load, for the latter speed, revealed (Table 4.8 (c)) that austenite was the major constituent. This is interesting since the pin is a ferritic material and the disc, although austenitic in structure, was found to wear far less than the former. This suggested the occurrence of phase transformed material in the surface layers of the pin.

4.4.2 Analysis for Elevated Temperature Wear Tests

(i) Mild Wear Debris

For the test runs below the transition load at 200°C and for all loads at the other high temperatures (300°C, 400°C and 500°C), the debris was completely oxide (see Table 4.10). Consisting of the rhombohedral and the spinel phases. It is possible that the wustite phase was also formed, particularly at the very high temperatures. However, due to slow cooling the latter may have been converted to one of the other phases.

(ii) Severe Wear Debris

This type of debris was encountered for loads above the transition at 200°C. The wear fragments consisted of austenite, ferrite, the spinel oxide phase and possibly $\gamma - Fe_2O_3$. The relative intensities of the lines with 'd' values 2.96, 2.51, 1.61 and 1.48 A° suggested that the oxide was mainly spinel (44) and $\gamma - Fe_2O_3$, if at all present, was in small quantities. As the load was increased the intensity of the austenite lines increased accordingly.

4.5 Glancing Angle X-Ray Diffraction of the Worn Specimens

Glancing angle X-ray diffraction analysis of the worn specimens was used to substantiate the findings of the powder diffraction technique.

4.5.1 Analysis for Wear Tests Without External Heating

In the case of the pin material, the ferrite lines were used as the internal reference. For conditions where mild wear was prevalent, the rhombohedral and spinel oxide phases were detected in the surface layers of Brico 65. By the same token, the austenite lines were used as the internal standard in the case of 21 - 4N (disc). Under mild wear conditions, the same oxide phases found in the pin were identified in the disc.

For the 2 m/s test runs above the transition, austenite and the spinel oxide phase were detected (as additional materials) in the surface layers of the pin. The glancing angle X-ray diffraction patterns of the disc material gave lines (in addition to the austenite lines) which could be interpreted as belonging to the spinel oxide phase and ferrite. However, under these conditions of high stresses and strains the lines corresponding to the latter could also be interpreted as indicative of body centred cubic martensite (α^1) (45). Various workers (46 - 49) have found that on cold-working the face centred cubic austenitic structure transforms to . α^1.

4.5.2 Analysis for Wear Tests at Elevated Temperatures

The glancing angle technique revealed that under mild wear conditions the rhombohedral and spinel oxide phases were present in the surface layers of both pin and disc materials (as in the non-externally heated wear tests).

Intensity	2 θ (degrees)	d (A^{o})	Possible Identity		
	28.75	3.67	$(Fe,Cr)_2O_3$		
	35.5	2.96			$FeFe_{(2-x)}Cr_xO_4$
b_3	39.25	2.67	$(Fe,Cr)_2O_3$		
b_2	41.75	2.52	$(Fe,Cr)_2O_3$		
b_1	52.3	2.03		Ferrite	
	58.2	1.84	$(Fe,Cr)_2O_3$		
	61.5	1.75			$FeFe_{(2-x)}Cr_xO_4$
	64	1.69	$(Fe,Cr)_2O_3$		
	74.2	1.48	$(Fe,Cr)_2O_3$		$FeFe_{(2-x)}Cr_xO_4$
	77	1.44	$(Fe,Cr)_2O_3$	Ferrite	
	99.75	1.17		Ferrite	
	124.0	1.01		Ferrite	

TABLE 4.11 (a) Glancing angle diffraction pattern for Brico 65(Pin) at $12\frac{1}{2}$N, 200°C (Co(K_α) radiation, $\lambda \approx 1.789A^{o}$).

b_1 Most intense line

b_2 Second most intense line

b_3 Third most intense line

Intensity	2 θ (degrees)	d (A^{o})	Possible Identity		
f	21.5	4.80			$FeFe_{(2-x)}Cr_xO_4$
b_4	35.25	2.96			$FeFe_{(2-x)}Cr_xO_4$
b_3	41.5	2.53			$FeFe_{(2-x)}Cr_xO_4$
b_2	50.8	2.085	Austenite		
b_1	52.3	2.03		Ferrite	
	59.5	1.80	Austenite		$FeFe_{(2-x)}Cr_xO_4$
	66.8	1.62			$FeFe_{(2-x)}Cr_xO_4$
f	73.75	1.48			$FeFe_{(2-x)}Cr_xO_4$
	77	1.44		Ferrite	
	89	1.28	Austenite		$FeFe_{(2-x)}Cr_xO_4$
	99.75	1.17		Ferrite	
	110.5	1.08	Austenite		$FeFe_{(2-x)}Cr_xO_4$
	124.5	1.01		Ferrite	

TABLE 4.11 (b) Glancing angle diffraction pattern for Brico 65 (pin) at 62.5N, 200°C (Co (K_α) $\lambda \approx 1.789$ A^{o}).

b_1 Most intense line

b_2 Second most intense line

b_3 Third most intense line

f faint line

Intensity	2θ (degrees)	d (A°)	Possible Identity		
	35.25	2.96			$FeFe_{(2-x)}Cr_xO_4$
	41.50	2.53			$FeFe_{(2-x)}Cr_xO_4$
b_1	51.0	2.08		Austenite	
b_2	52.3	2.03	Ferrite		
	59.75	1.80		Austenite	$FeFe_{(2-x)}Cr_xO_4$
	66.8	1.62			$FeFe_{(2-x)}Cr_xO_4$
	73.75	1.48			$FeFe_{(2-x)}Cr_xO_4$
	77	1.44	Ferrite		
	89	1.28		Austenite	$FeFe_{(2-x)}Cr_xO_4$
	99.75	1.17	Ferrite		
	110.5	1.08		Austenite	$FeFe_{(2-x)}Cr_xO_4$
	124.5	1.01	Ferrite		

TABLE 4.11 (c) Glancing angle diffraction pattern for 21 - 4N (disc) at 62.5N, 200°C (Co (K_α), $\lambda \approx 1.789$ A°).

b_1 Most intense line

b_2 Second most intense line

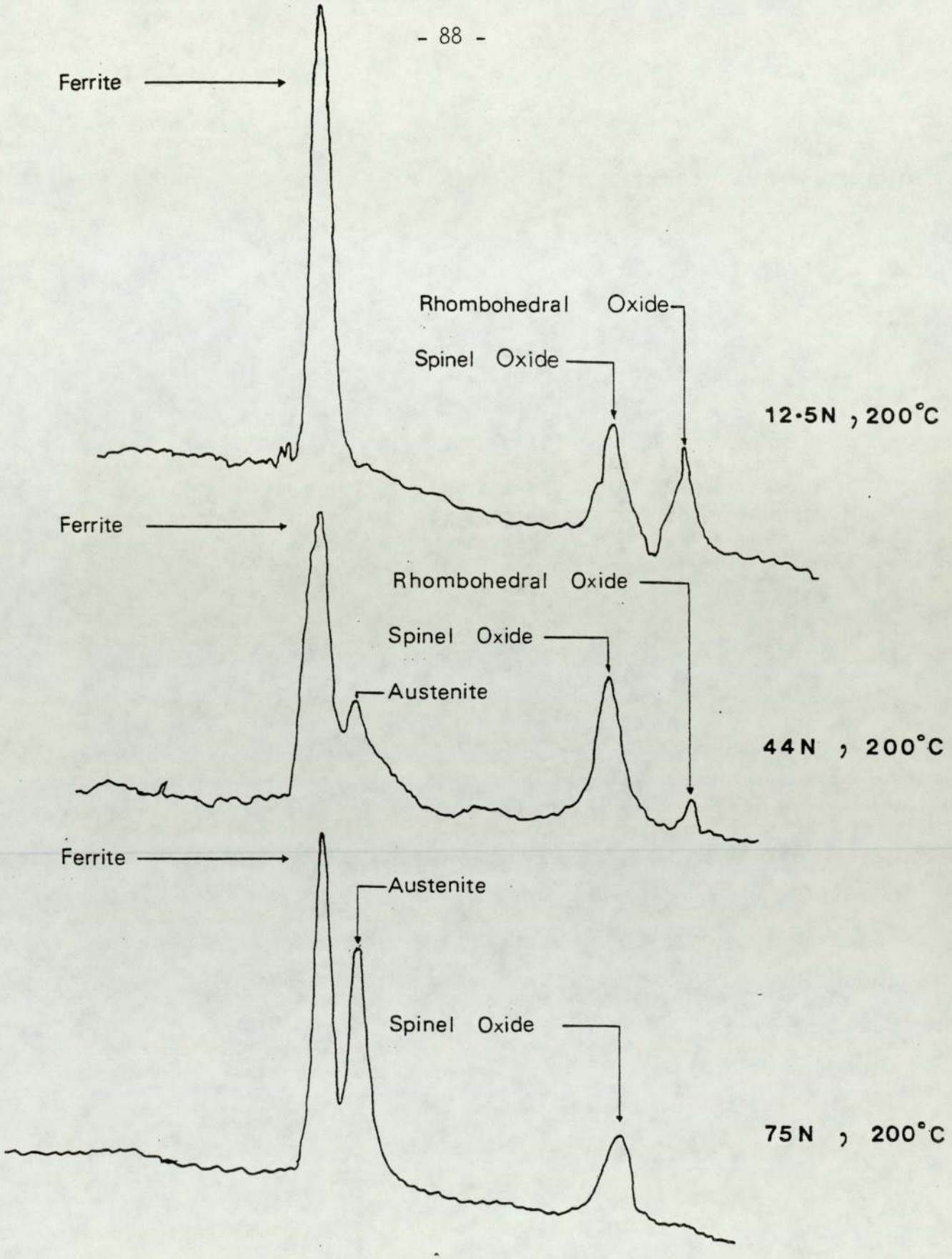

FIGURE 4.13 Variation of the main Ferrite, Austenite and Oxide Diffraction Lines with Load (Brico 65 pin).

In the case of severe wear conditions, which was prevalent at 200°C above the transition, the constituents detected in the surface layers of Brico 65 were austenite and the spinel oxide. The rhombohedral oxide was not detected. For the 21 - 4N disc the species identified from the diffraction patterns were the spinel oxide and ferrite or body centred cubic martensite. The analysis of typical glancing angle patterns are given in Tables 4.11 (a), (b) and (c).

Figure 4.13 shows the variation of the relative intensities, obtained from a micro-densitometer trace of the X-ray films (50) (for Brico 65) of the main austenite, ferrite and oxide diffraction lines as the wear regime changed from mild to severe wear, with increasing load at a disc temperature of 200°C. As is evident from Figure 4.13, the amount of austenite present increased with load while the spinel oxide decreased and the rhombohedral oxide was completely absent at higher loads.

4.6 Scanning Electron Microscopy (SEM) and Energy Dispersive Analysis by X-Rays (EDAX)

Scanning electron micrographs of typical wear surface topographies for both pin and disc materials are described in relation to the various wear regimes encountered. In addition, the thickness of oxide films formed during sliding are related to the above wear regimes. The results of wear debris examination by SEM and EDAX are given.

To support the above findings, the results of the sub-surface examinations are also given.

(a)

(b)

FIGURE 4.14 Wear Surface Topographies at 0.23 m/s
(a) Brico 65 (25N, 0.23 m/s)
(b) 21 - 4N ($18\frac{3}{4}$N, 0.23 m/s)

4.6.1 Wear Surface Topographies at 0.23 m/s

Figures 4.14 (a) and (b) show the metallic / oxide nature of the wear scars formed at this slow speed of sliding. It is evident from the micrographs that in addition to the oxidized regions of higher elevation, there is metallic deformation and subsequent removal of under-lying material. This accounts for the wear debris being of a metallic / oxide nature.

4.6.2 Mild Wear Surface Topographies

Figures 4.15 (a), (b), (c), (d), (e), (f), (g), and (h) illustrate the general nature of the wear scars of Brico 65 and 21 - 4N under mild wear conditions, at "room" (no external heating) and elevated temperatures. Clearly, the surfaces of the pin and disc are very similar under these conditions of sliding. Typically, the wear topography of the steels are characterised by numerous oxide islands which are very smooth in appearance.

The average size and number of these oxide islands (plateaux) depend on the details of the sliding wear tests. For the purely frictionally heated wear tests the number of plateaux appear to increase with load. At elevated temperatures the oxide islands take on a very shiny appearance. The topographies are of similar appearance to those reported by Stott et. al. (14), formed under conditions of reciprocating sliding. However, the method of formation of the oxide films in the present work is essentially different to the method of formation of Stott's oxide glazes (this is discussed in greater detail in Chapter 6). The glazed appearance of the plateaux is due to the mechanical action of the sliding process.

The composition of the oxide plateaux is exemplified by

FIGURE 4.15 Mild Wear Surface Topographies

(a) Brico 65 62½N, 2 m/s

(b) 21 - 4N 37½N, 2 m/s

(c) Brico 65 31N, 200°C

(d) Brico 65 56N, 300°C

(e) Brico 65 62½N, 300°C

(f) Brico 65 50N, 500°C

(g) Brico 65 100N, 400°C

(h) 21 - 4N 62½N, 300°C

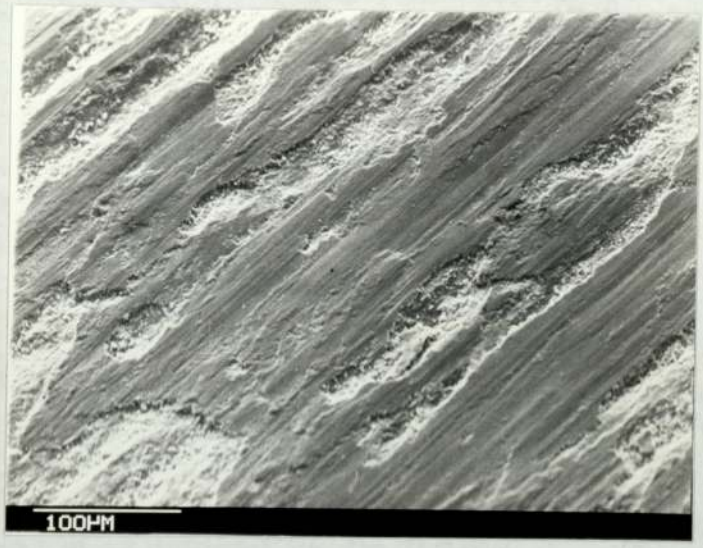

(a)

(b)

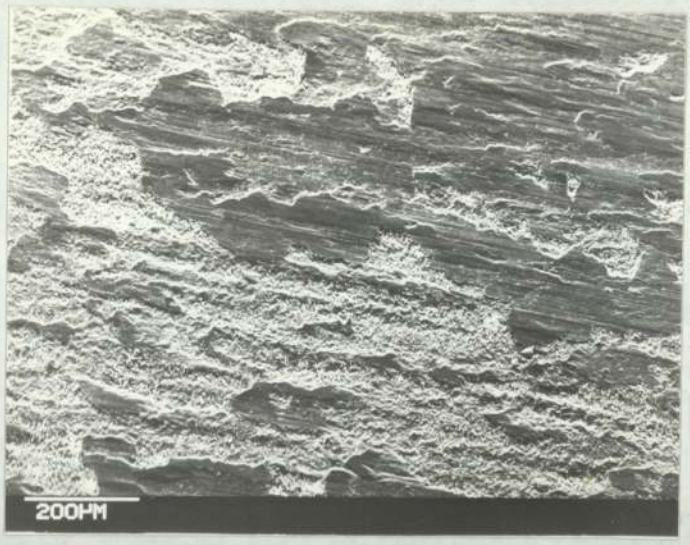

(c)

(d)

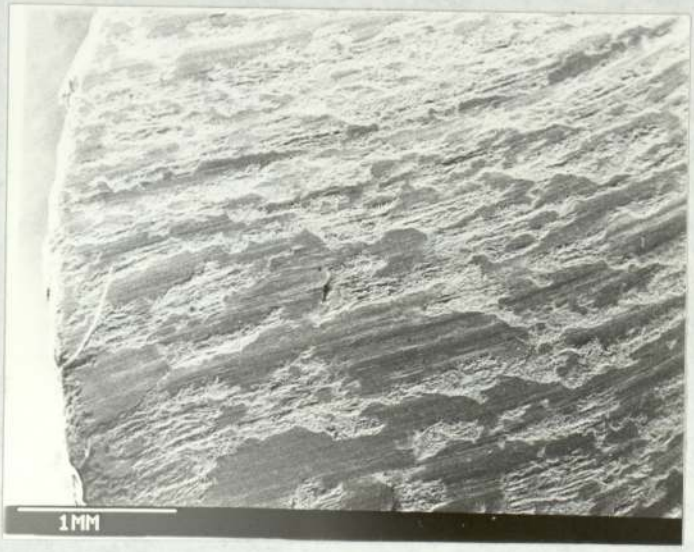

(e)

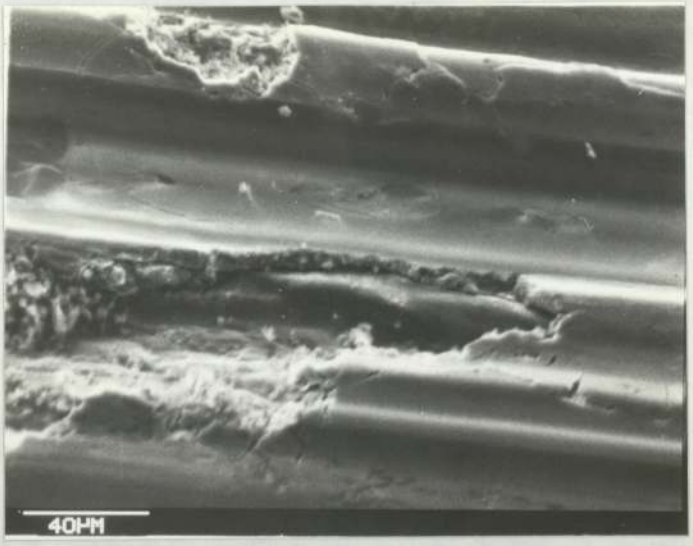

(f)

(g)

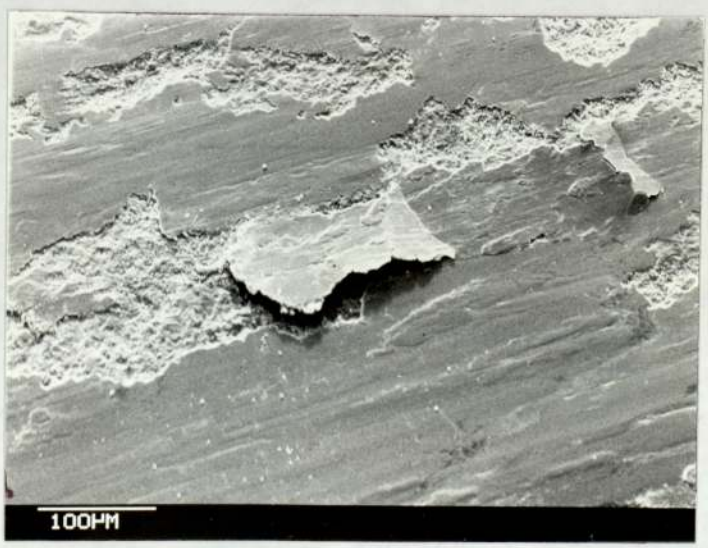

(h)

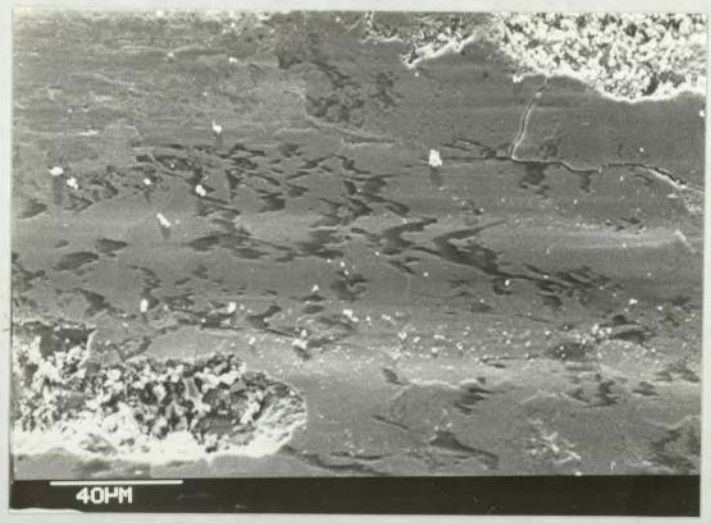

(a)

(b)

FIGURE 4.16 (a) Micrograph Showing Section of Oxide Plateau (Brico 65 25N, 400°C).

X-ray Distribution of (b) Si, (c) Fe and (d) Cr in (a).

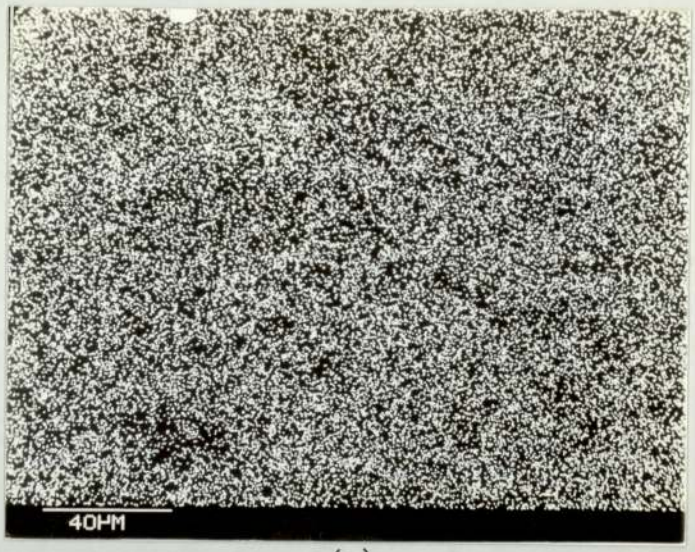

(c)

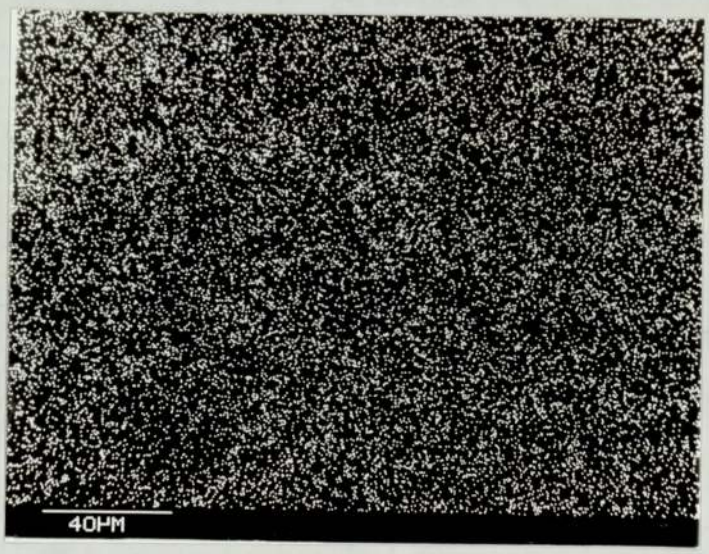

(d)

FIGURE 4.16

the micrographs in Figure 4.16. There appears to be an enrichment of silicon in the very top layers of the oxide film. Iron and chromium appear to be bonded together in solid solutions of their rhombohedral and spinel oxide phases (as indicated by X-ray diffraction analysis). It seems likely that the other elements of minor concentrations such as manganese and nickel are also bonded within these solid solutions.

4.6.3 Transfer and Abrasive Wear Surface Topographies

Figures 4.17 (a), (b), (c), and (d) illustrate the differences in the nature of the wear scars of Brico 65 (pin) and 21 - 4N (disc) for experimental conditions above the transition load, at 2 m/s (no external heating) and at a disc temperature of 200°C.

Typically, the pin topography is characterised by the presence of numerous grooves running parallel to the sliding direction. In contrast, numerous transferred islands of material are clearly evident in the disc surface. The original machine lines can be seen below the transferred patches, in Figures 4.17 (b) and (d). This indicates negligible wear of the disc. EDAX showed that the silicon concentration in the transferred areas was well above the bulk concentration of the disc material.

4.6.4 Oxide Film Thickness Measurements

A summary of the oxide film thickness measurements, for the various sliding conditions is given in Table 4.12.

In the cases of predominantly oxidational wear, the equilibrium film thickness on both the pin (ξ) and disc (ξ^*) surfaces were found to be very similar. For the metallic / oxidational wear modes, ξ^* was always found to be greater than ξ.

(a)

(b)

FIGURE 4.17 Transfer Wear Surface Topographies .

(a) Brico 65 75N, 2m/s

(b) 21 - 4N 75N, 2m/s

(c) 21 - 4N 62½N, 200°C

(d) Brico 65 62½N, 200°C

(e) Brico 65 62½N, 200°C

(c)

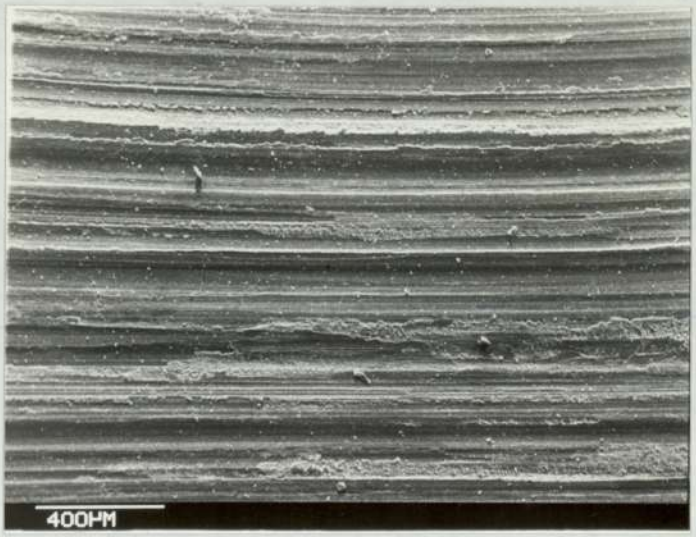

(d)

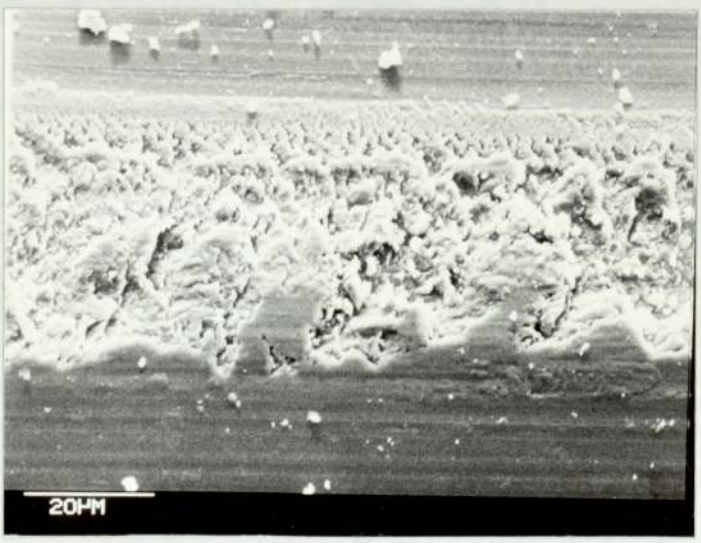

(e)

Experimental Condition	Oxide film thickness (μm)	
	Pin (ξ)	Disc (ξ*)
0.23 m/s test runs	1.5 ± .5	1.5 ± .5
1 m/s - below transition	2.0 ± .25	2.0 ± .25
1 m/s - above transition	1.5 ± .25	3.0 ± .5
2 m/s - below transition	3.25 ± .25	3.5 ± .25
2 m/s - at transition	2.5 ± .25	3.5 ± .25
2 m/s - above transition	2.0 ± .25	4.0 ± .5
3.3 m/s - all test runs	3.5 ± .5	3.5 ± .5
200°C - below transition	3.5 ± .25	3.5 ± .25
200°C - at transition	3.0 ± .5	3.5 ± .5
200°C - above transition	very patchy <.5	3.25 ± .5
300°C, 400°C, 500°C - all loads	5 ± 1	5 ± 1

TABLE 4.12 Variation of Oxide film thickness with Experimental Conditions.

FIGURE 4.18 Critical Oxide Film Thicknesses .

(a) Brico 65 62½N, 1 m/s

(b) 21 - 4N 62½N, 1 m/s

(c) Brico 65 56N, 3.3 m/s

(d) 21 - 4N 56N, 3.3 m/s

(e) Brico 65 100N, 400°C

(f) 21 - 4N 62½N, 300°C

(g) Brico 65 69N, 400°C

(h) Brico 65 75N, 2 m/s

(i) 21 - 4N 75N, 2 m/s

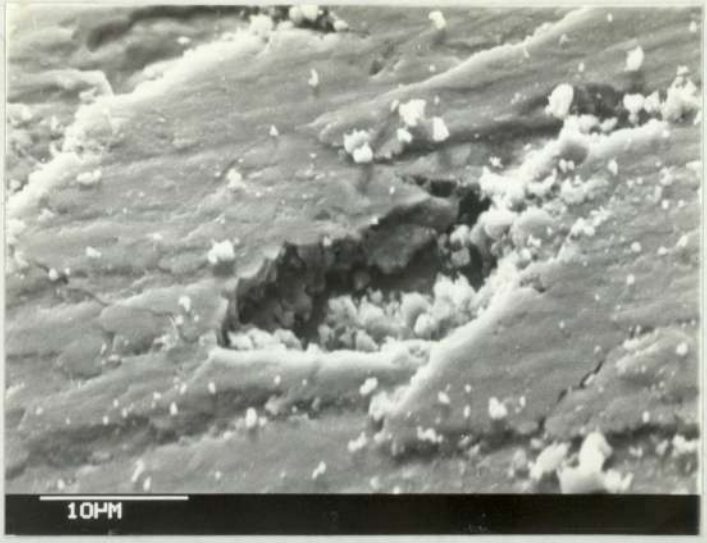

(a)

(b)

(c)

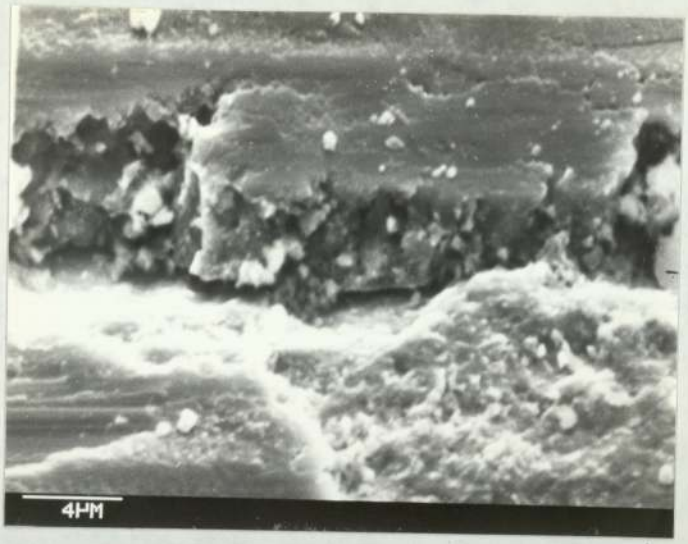

(d)

(e)

(f)

(g)

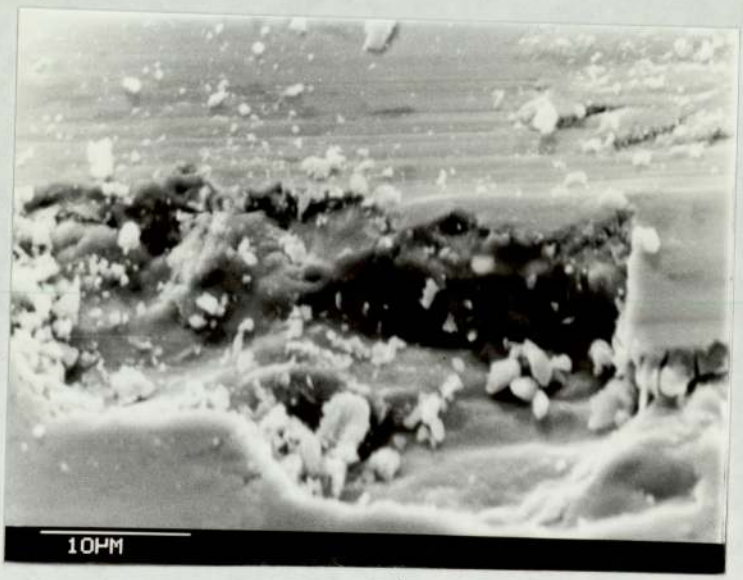

(h)

(i)

The trends in the results is best illustrated by the test runs at a disc temperature of 200°C. In the region below the transition load of 44N, the equilibrium oxide films on both pin and disc was about 3.5 μm. Above the transition, ξ was less than .5 μm and ξ^* was approximately 3.25 μm.

Micrographs of critical film thicknesses are shown in Figures 4.18 (a), (b), (c), (d), (e), (f), (g), (h) and (i).

4.6.5 Wear Debris

Table 4.13 gives the volume ratio of iron to chromium in the wear debris for various experimental conditions. The figures were obtained by comparing the relative intensities of the Kevex peaks of Fe (K_α) and Cr (K_α). It is evident that for all the above conditions the relative concentrations of Fe and Cr in the wear debris is similar to the bulk concentrations. This would indicate that the oxides exist as solid solutions.

Figures 4.19 (a) and (b) are SEM micrographs of oxide and metallic / oxide wear debris, respectively.

4.6.6 Tapered Sections

SEM micrographs of typical tapered sections are shown in Figure 4.20 (a), (b); Figure 4.21 (a), (b) and Figure 4.22 (a), (b) of various worn specimens.

(i) Mild Wear

In the case of specimens from mild wear conditions there was a protective film between the mounting material (bakelite) and the alloy. The measured thickness of the film was in agreement with the measurements of critical oxide film thicknesses (see Table 4.14).

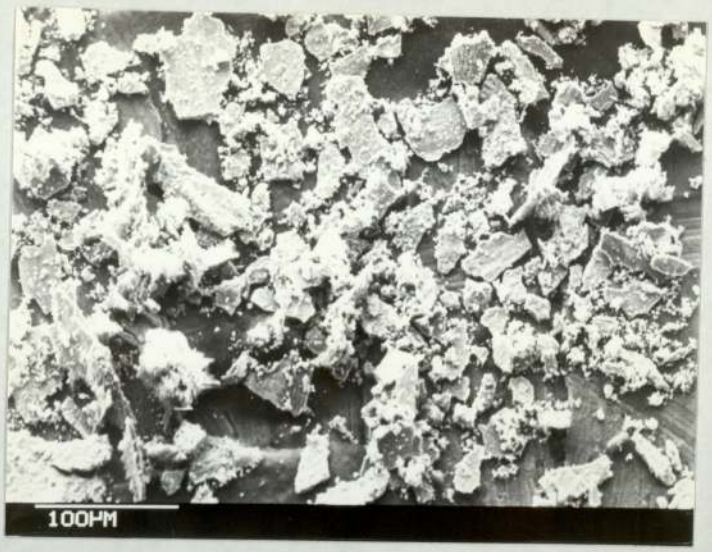

(a)

(b)

FIGURE 4.19 (a) Oxide Wear Debris (50N, 2 m/s) .
(b) Metallic / Oxide Wear Debris (87N, 2 m/s) .

(a)

(b)

FIGURE 4.20 Tapered Sections from Mild Wear Region .
(a) Brico 65 12½N, 200°C; θ = 8.5°
(b) Brico 65 75N, 300°C; θ = 11.3°
$FeCl_3$ (alcholic) etchant

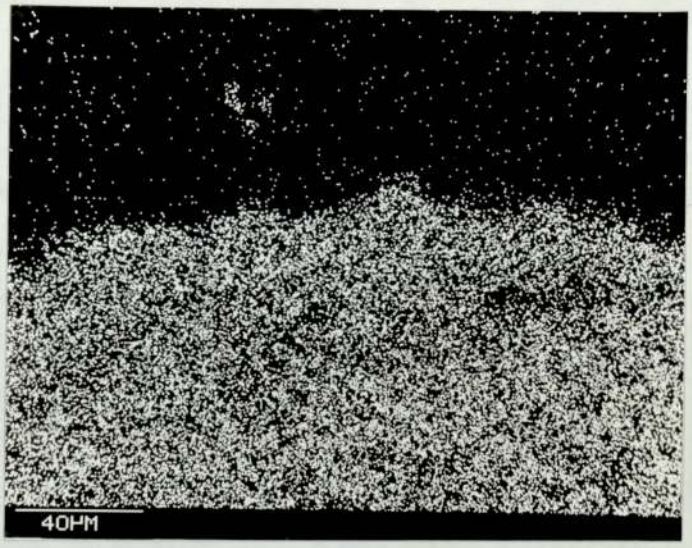

(c)

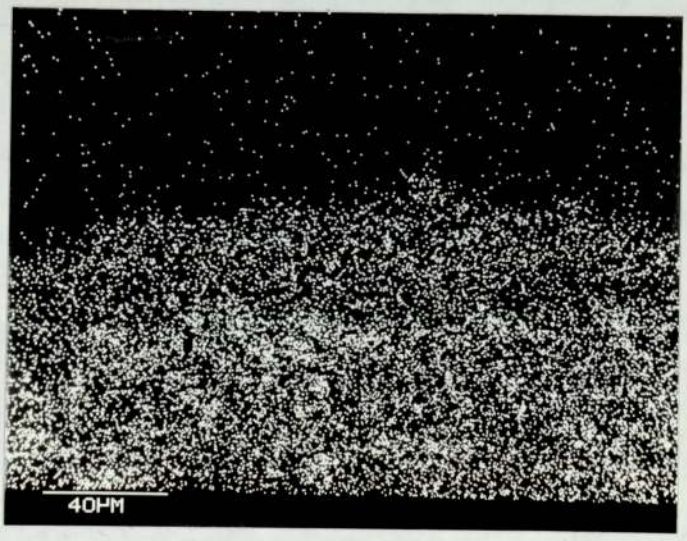

(d)

FIGURE 4.20 X-ray Distribution of (c) Fe and (d) Cr in (b) .

(a)

(b)

FIGURE 4.21 Tapered Section from metallic / oxide wear region ($\theta = 5^{o}$) .

Brico 65 80N, 2 m/s .

(a) Structure of transformed layer

(b) Structure of oxide film

Etchant : Picral

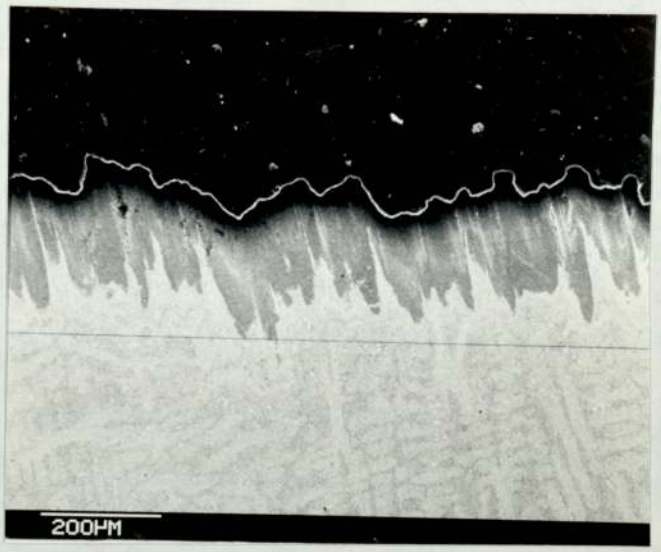

(a)

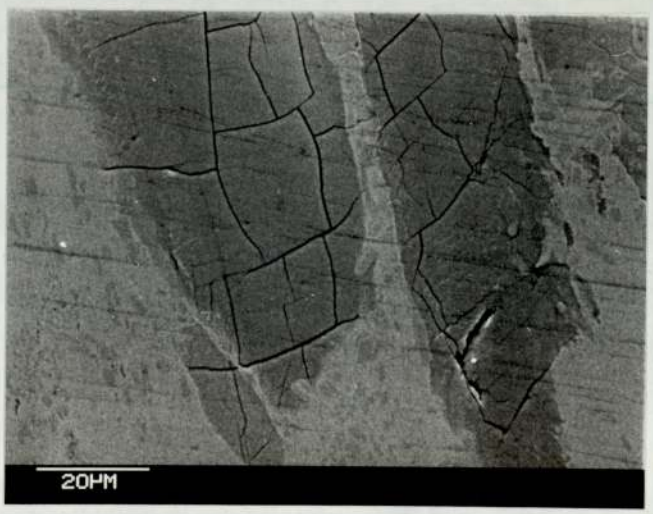

(b)

FIGURE 4.22 Tapered Section from severe wear region (θ = 8.53°).
Brico 65 50N, 200°C.
(a) General appearance of transformed layer.
(b) Stress cracks within layer.
X.ray Distribution of (c) Fe, (d) Cr and (e) Si in (a).

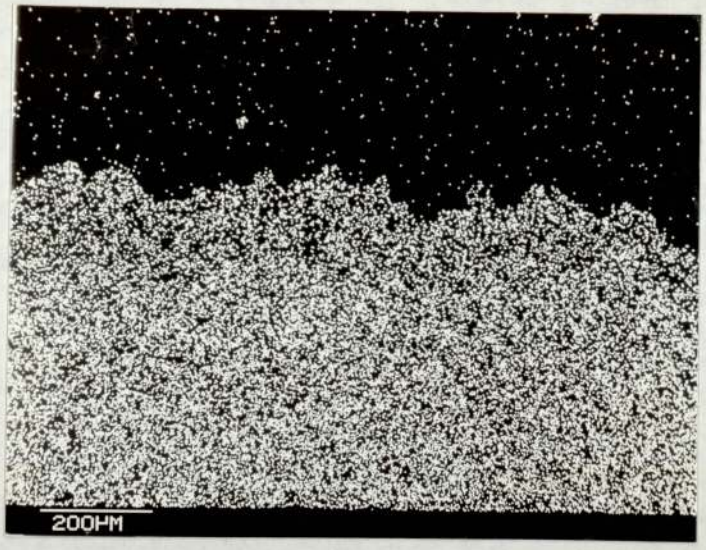

(c)

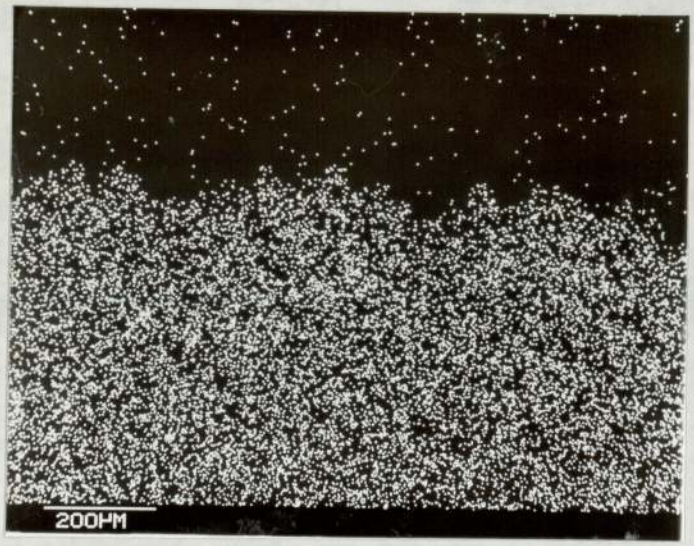

(d)

(e)

Experimental Condition	Volume Ratio Fe:Cr
Bulk Sample	3.1
50N, 2 m/s	2.8
75N, 2 m/s	2.9
12½N, 200°C	3.1
62½N, 200°C	2.9
56N, 300°C	3.2
100N, 400°C	3.1
25N, 400°C	3.2
75N, 500°C	3.2

TABLE 4.13 Volume ratio of Fe to Cr in Wear Debris for various experimental conditions.

Specimen	ξ (μm) - Tapered Section	ξ (μm) - Direct
BRICO 65, 12½N, 200°C	3.46	3.5 ± .25
BRICO 65, 75N, 300°C	5.9	5.0 ± 1.0

TABLE 4.14 Comparison between film thickness measurements by Tapered section and Direct Surface Examination.

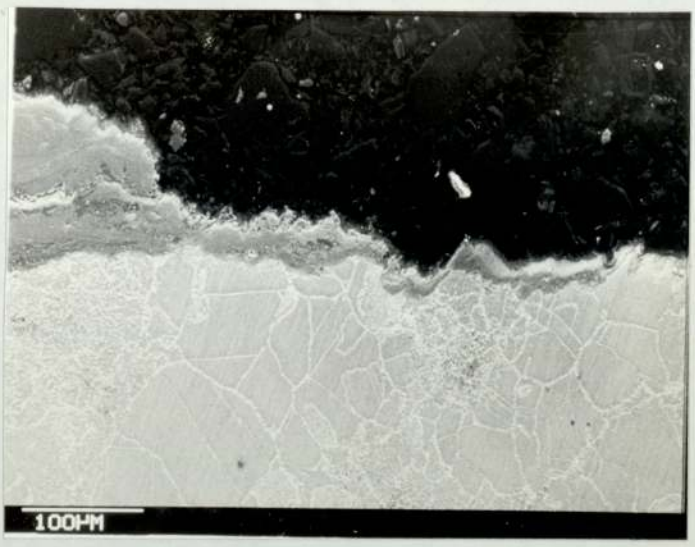

(a)

(b)

FIGURE 4.23 Tapered Section from severe wear region ($\theta = 12.84^{\circ}$).

21 - 4N $62\frac{1}{2}$N, 200°C.

(a) General appearance of transformed layer.

(b) Transferred material.

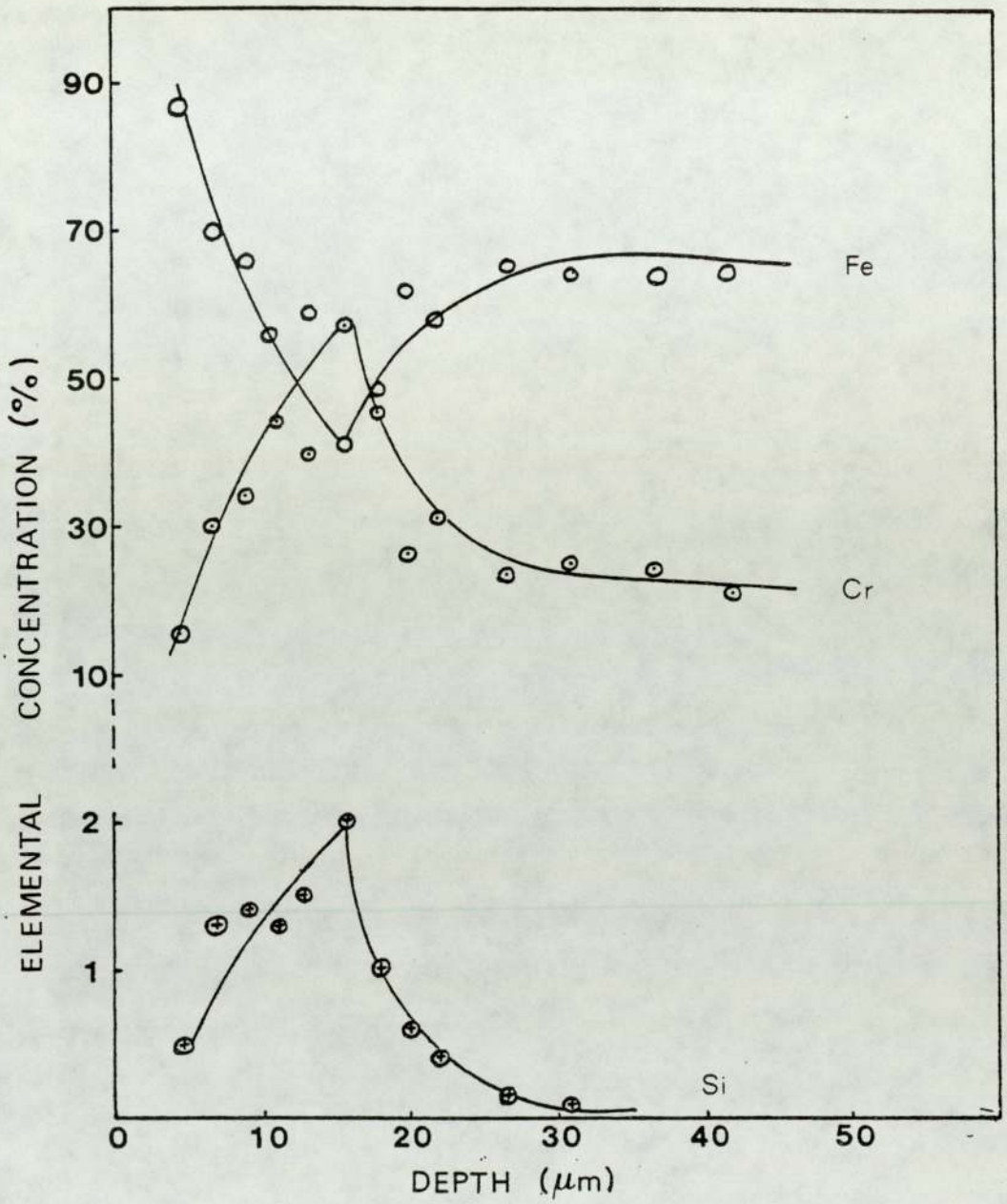

FIGURE 4.24 Elemental Concentration versus Depth for Iron, Chromium and Silicon (21 - 4N, 62½N, 200°C, 2 m/s).

(ii) Transfer Wear

In the case of this wear mode phase transformed materials were detected in the subsurface of Brico 65 and 21 - 4N.

For Brico 65 the transformed layer (probably a form of unstable austenite) was very non-uniform and patchy in appearance (Figure 4.22), with no evidence of oxide above the layer. In addition, numerous cracks were present in the layer for the test samples at 200°C (Figure 4.22). Microhardness tests showed that the layer was 650 - 800 VPN. However, the micrographs (Figure 4.22) suggest that the structure is of a brittle nature.

In contrast, the transformed material within the sub-surface of 21 - 4N is more compact in structure (Figure 4.23). Micro-hardness measurements within the layer revealed that it is very hard (greater than 1000 VPN). Figure 4.24 shows the variation of the concentrations of Fe, Cr and Si with depth, through the layer shown in Figure 4.23 (b). From the graphs it is evident that the Cr and Si levels are at a maximum about 15 μm below the surface, Fe being at a minimum concentration at this depth, within the transformed layer. Dumbleton and Douthett (45) have found that silicon improves the wear resistance of austenitic steels.

4.7 Auger Analysis

This technique although not extensively used, confirmed the findings of the more widely used methods of surface examination. Figures 4.25 (a) and (b) show the section of an oxide plateau with the corresponding oxygen distribution. There can be no doubt that the plateau is oxide. A typical Auger spectrum is shown in Figure 4.26.

For mild wear specimens (thick oxide films), even after

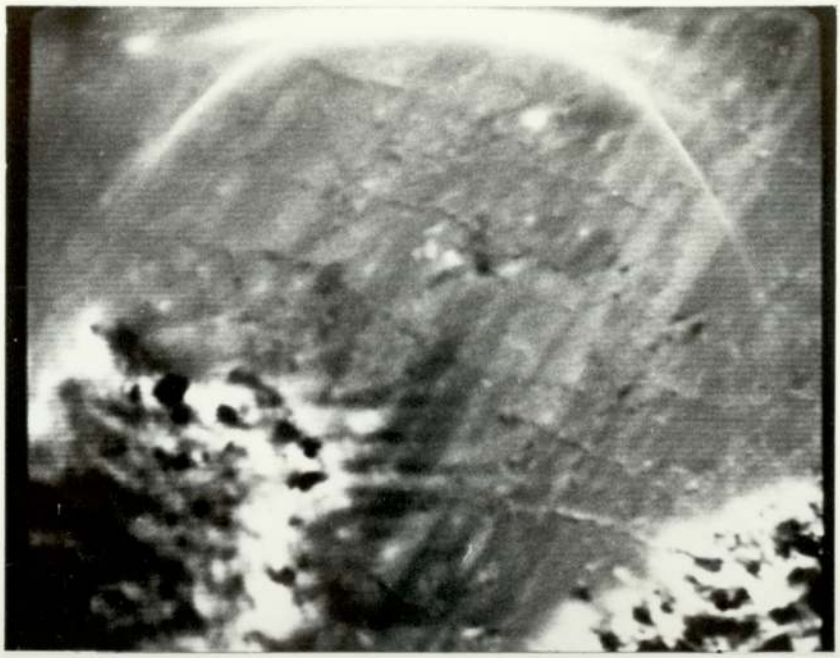

(a)

(b)

Figure 4.25 (a) Section of an oxide plateau (Brico 65 $62\frac{1}{2}$N. 300°C)

(b) Corresponding oxygen map

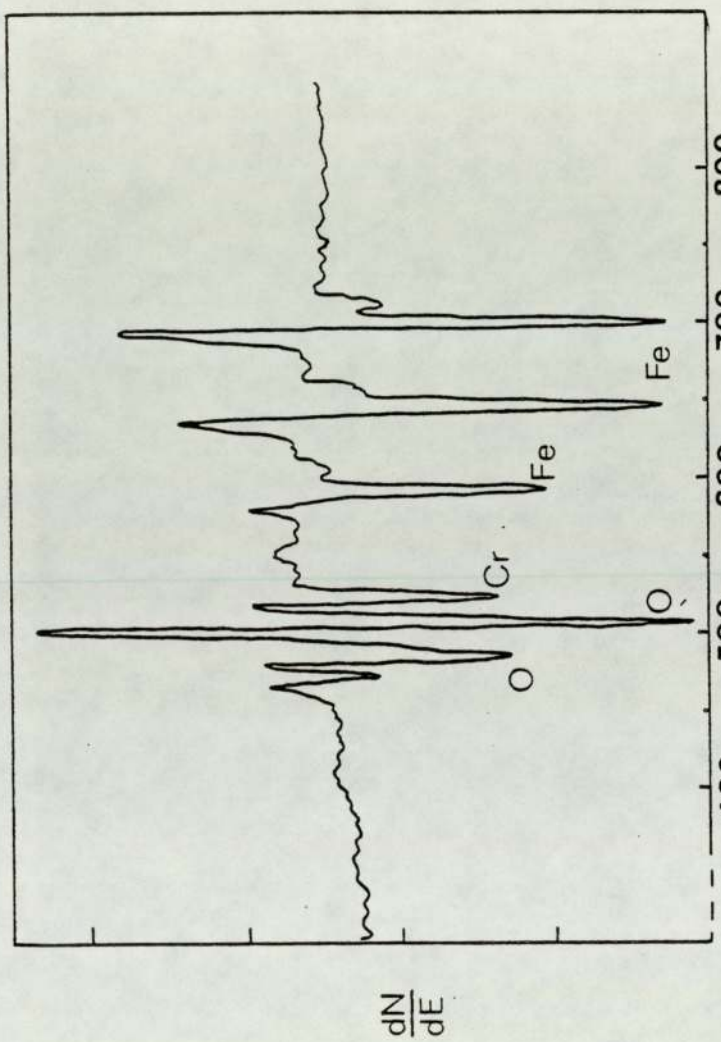

FIGURE 4.26 Typical Auger Spectrum (Brico 65, 62½N, 2 m/s).

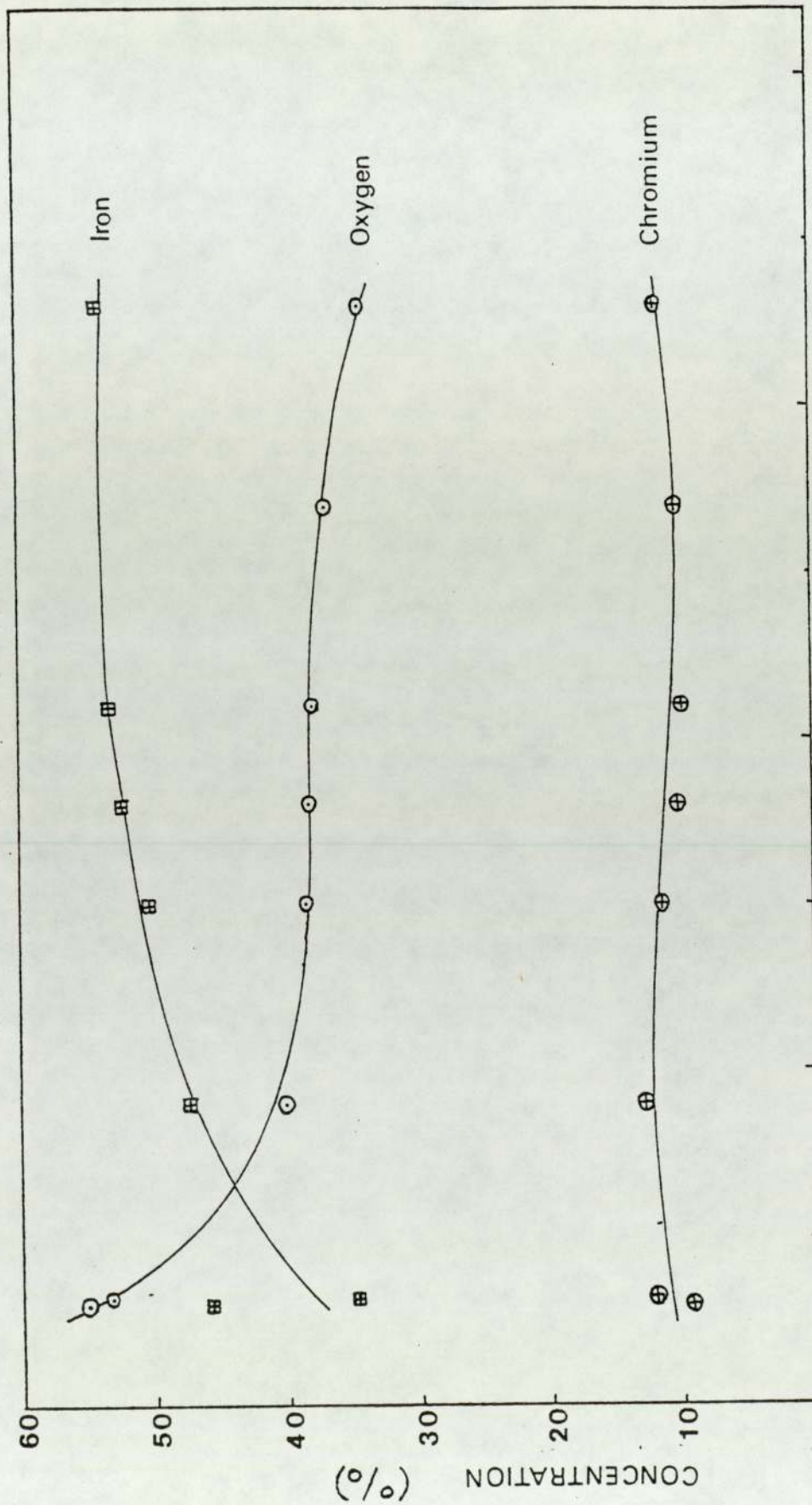

FIGURE 4.27 Auger Analysis of Argon Etched Pin Sample (20 kV, 25 mA).

six hours etching the concentration of oxygen did not decrease significantly. This is presumably due to the very low etching rates of these compact oxides. The relative concentration of chromium to iron although variable over the specimen area, was never found to be greater than the bulk concentration.

Figure 4.27 shows the variation of the relative concentrations of oxygen, iron and chromium with etching time for a specimen pin taken from the transfer wear region. There was an initial sharp decrease in the oxygen concentration followed by a very gradual decrease for etching times up to 330 minutes. There was a gradual increase in iron concentration to a value to 54% at 330 minutes. The chromium concentration level was approximately constant.

CHAPTER 5

THEORETICAL CONSIDERATIONS

5.1 Introduction

In this chapter the heat flow analysis for the sliding bodies will be dealt with in order to deduce important parameters such as the bulk surface pin temperature, the division of frictional heating at the pin-disc interface and the contact temperature of the sliding bodies.

Using the deduced surface parameters along with the experimentally measured quantities (e.g. oxide film thickness, wear rate) tribological values for the activation evergy (Q_p) and the Arrhenius constant (A_p), for parabolic oxidation are obtained from the oxidational wear equation (20).

In addition, the modification of Quinn's oxidational wear theory to account for 'out-of-contact' oxidation is discussed.

5.2 Heat Flow Analysis

5.2.1 Division of Heat and the Bulk Surface Pin Temperature

The calorimeter arrangement for the heat flow analysis is shown in Figure 3.3.

It has been shown elsewhere (31) that under steady state conditions the heat flowing per second along the insulated portion of the pin is given by

$$H_3 = K_s \pi R_t^2 M \left\{ \frac{(T_A - T_C) \times \cosh(ML_3) - (T_B - T_C)}{\sinh(ML_3)} \right\} \quad \cdots (5.1)$$

where $M^2 = 2 K_i / K_s R_t^2 \log_e (R_a/R_t)$ . . .(5.2)

The above symbols designate the following:

T_A = temperature recorded by thermocouple at pin surface just as it emerges from pin holder.

T_B = temperature recorded by thermocouple situated at a distance L_3 along the cylindrical surface of the pin from the thermocouple reading T_A.

L_3 = distance between thermocouples reading T_A and T_B.

T_C = thermocouple reading at the inside diameter of the copper cylinder around the pin and insulator.

K_s = thermal conductivity of the pin material

K_i = thermal conductivity of the insulator

R_t = radius of the pin

R_a = outer radius of the cylindrical insulating medium .

Furthermore, the heat flow per second (H_2) entering the section of the pin where the thermocouple measuring T_A is conducting heat away is given by

$$H_2 = H_3 + C (T_A - T_C) / (R_a - R_t) \quad . . .(5.3)$$

The heat flow rate (H_1) into the pin from the pin-disc interface is given by the equation (Rowson and Quinn 1980)

$$H_1 = \frac{\pi}{Z} R_t K_s \left\{(T_A - T_C) \times \sinh(L_1/ZR_t)\right\} + H_2 \cosh(L_1/ZR_t) \quad . . .(5.4)$$

where $Z^2 = K_s/2R_t h$

and L_1 = length of pin exposed to the air between calorimeter and disc.

h = the heat transfer coefficient from the exposed portion of the

pin to the ambient air.

The bulk surface temperature of the pin (T_s) is obtained from the expression

$$T_s = (T_A - T_C) \times \cosh(L_1/ZR_t) + \frac{ZH_2}{\pi \overline{K_s} R_t} \times \sinh(L_1/ZR_t) + T_C \quad \ldots (5.6)$$

At the real areas of contact the total frictional heat generated per second is simply the product of the frictional force (F) and the sliding speed (U). The experimental division of heat (δ_{exp}) between the pin and the disc (51, 52) can therefore be calculated from the equation

$$\delta_{exp} = H_1/UF \quad \ldots (5.7)$$

The heat flow parameters (T_s and δ_{exp}) were calculated from the preceeding equations by using the experimentally measured quantities in a Fortran computer program. Figure 5.1 shows the variation of the bulk surface temperature of the pin with load, at the various sliding speeds, for experiments in which there was no external heating. The linear variation of T_s with load is clearly exemplified by these graphs (53 - 55). In addition, for the 2 m/s test runs there is a moderate increase in the slope of the graph for loads above 67N, corresponding to the change in wear regime from purely oxidational to metallic/oxidational wear. Recalling Figure 4.4, there was a rapid increase in the wear rate (1.3×10^{-12} m^3/m) as the load was increased from 67N to 75N. The incremental increase in the bulk surface temperature of the pin (T_s), although definitely present, is less significant than the increase in wear rate. From Table 4.12 the SEM measurements indicate that the oxide film thickness has decreased from approximately 3.25 μm below the transition to approximately 2.0 μm

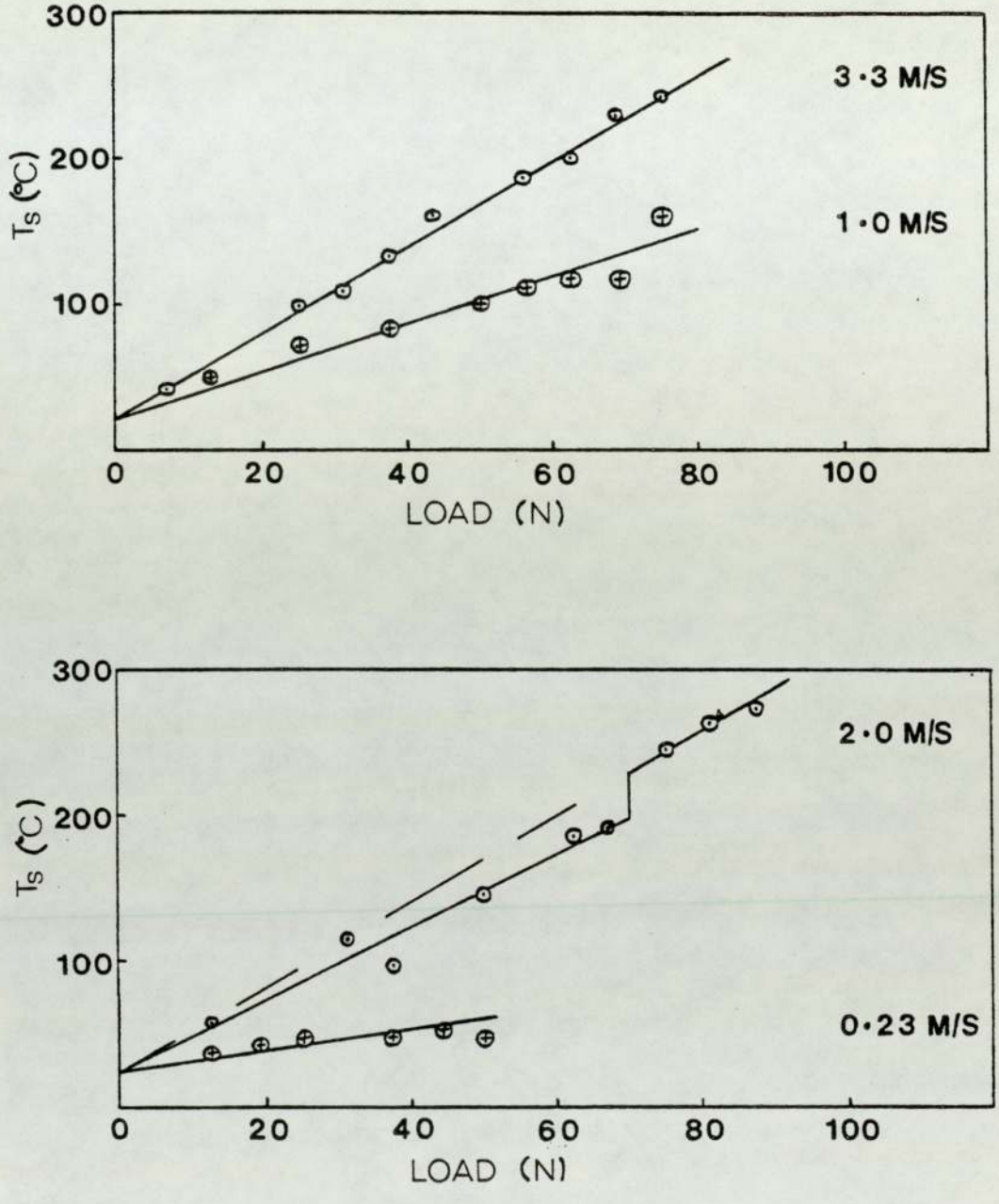

FIGURE 5.1 Bulk Surface Pin Temperature versus Load at Various Sliding Speeds (no external heating).

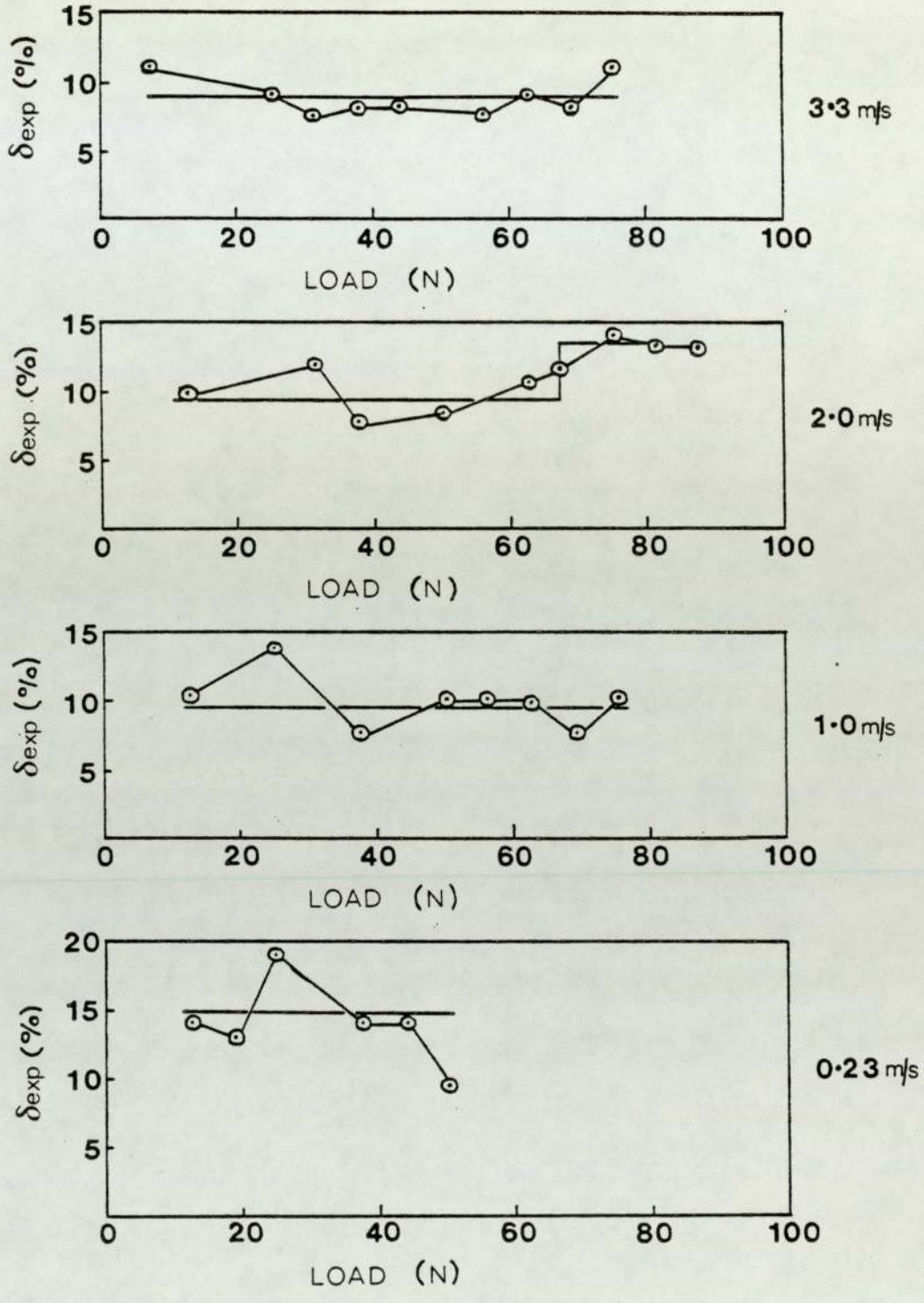

FIGURE 5.2 Division of Heat versus Load at Various Sliding Speeds (no external heating).

above the transition. In addition, there is some metallic contact for loads above the transition. The surface conductance has therefore increased, above 67N, and hence the substrate temperature, T_s, has increased accordingly.

The corresponding experimental division of heat versus load graphs are shown in Figure 5.2. It is evident that there is a considerable scatter in the experimental values. The mean values ($\bar{x}$) and the standard deviations (σ) of δ_{exp} are given in Table 5.1. For the 2 m/s wear tests, the moderate increase in the division of heat for loads above 67N, due to the change in surface conductance, has been masked by the scatter in the experimental points.

Figure 5.3 shows the variation of T_s with load at various disc temperatures (as measured by a thermocouple close to the wear track). The linear dependence of the bulk surface pin temperature on load is further illustrated by these results. At a disc temperature of 200° C, it is interesting to note the sudden incremental increase (100° C) in T_s as the load was increased from 44N to 50N. Recalling Figure 4.9, there was a rapid change in wear rate for the same increase in load.

From the SEM measurements in Table 4.12, below the transition load of 44N the average oxide film thickness on the pin was 3.5 μm, and above the transition, examination indicated that the surface oxide on the pin was very patchy and was less than 0.5 μm in thickness. Clearly a large change in surface conductance has occurred. This is far more significant than the small change in conductance, encountered for the purely frictionally heated wear tests at the same sliding speed of 2 m/s, for loads greater than 67N. Hence the sudden increase in the bulk pin surface temperature in the former case is far

Speed (m/s)	exp (%)			
	Below Transition		Above Transition	
	$\bar{x}$	σ		
3.3	8.8	1.5	-	-
2.0	9.6	1.6	13.3	0.6
1.0	9.6	1.9	-	-
0.23	14.8	2.4	-	-

Table 5.1 Experimental Division of Heat at Various Speeds.

Speed	Slope of T_s versus Load Graph	
	Below Transition	Above Transition
3.3	2.95	-
2.0	2.50	2.78
1.0	1.62	-
0.23	0.73	-

Table 5.2 Variation of dT_s / dW with speed.

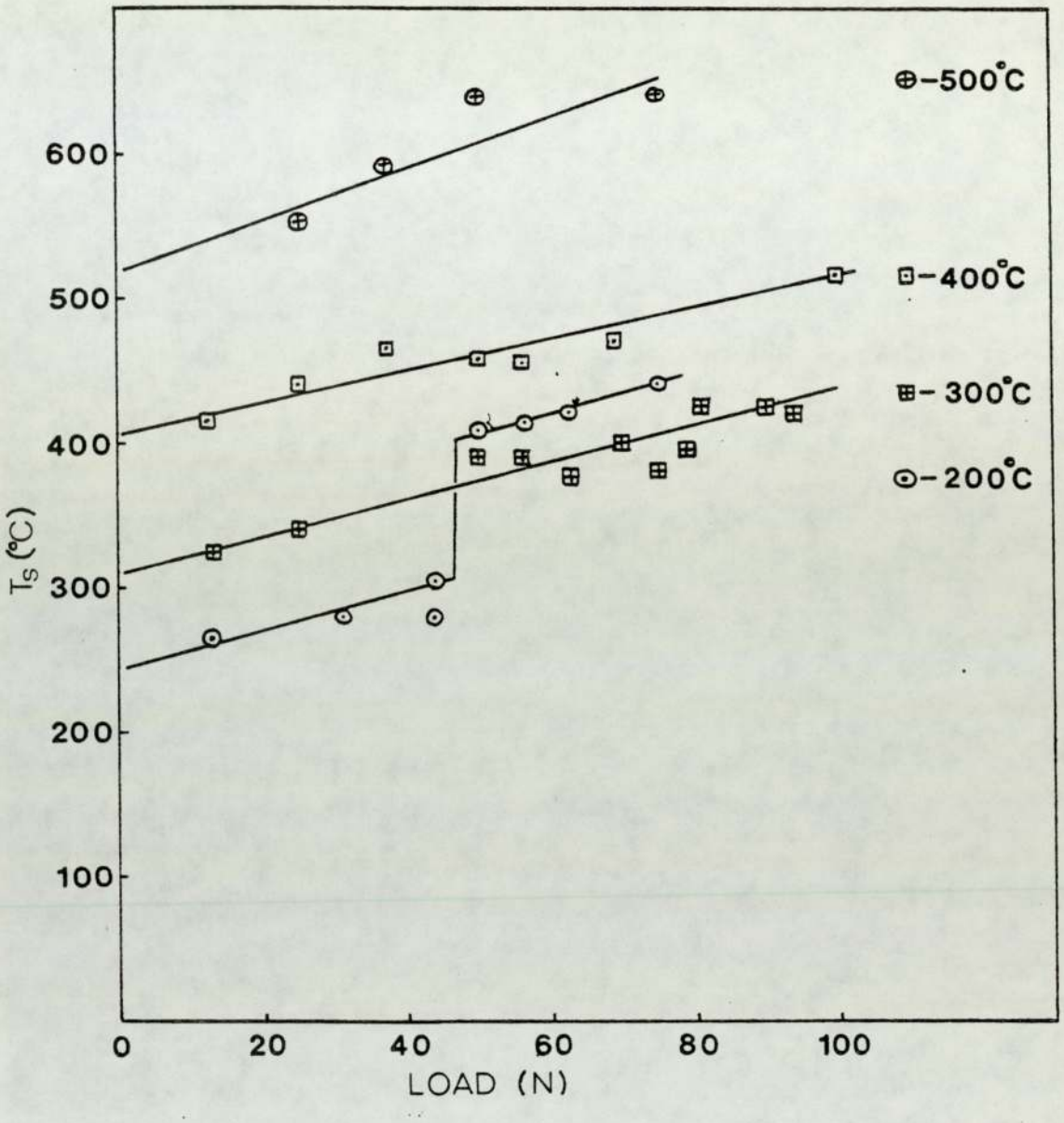

FIGURE 5.3 The Variation of Bulk Surface Pin Temperature with Load at various Disc Temperatures.

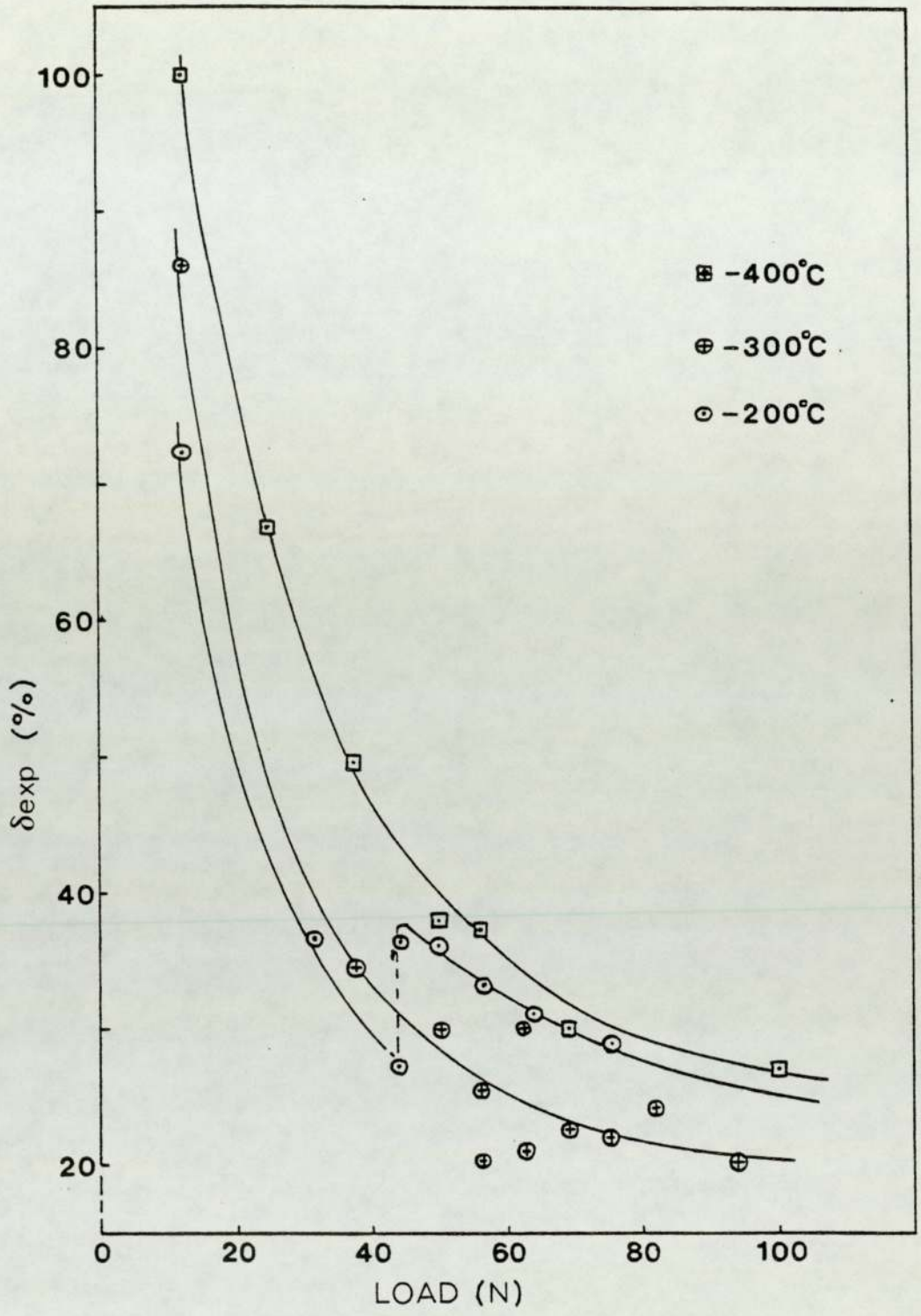

FIGURE 5.4 Division of Heat versus Load at Various Disc Temperatures.

greater.

The results further illustrate the similarities in the variation of wear rate and T_s with load (54, 55).

The variation of the experimental division of heat with load, at disc temperatures of 200°C, 300°C and 400°C are shown in Figure 5.4. It is instructive to note that frictional heating contributes to the disc temperature, in addition to external heating (see Section 3.6). As the load is increased the frictional contribution is increased, for the same disc temperature. However, as more electrical energy is supplied there is an increased resistance to frictional heating due to the increasing electrical heat flux. The results of these effects are:

(1) δ_{exp} decreases with load for any disc temperature. The curves in Figure 5.4 indicate that the variation of δ_{exp} with load may be described by a combination of exponential functions.

(2) δ_{exp} increases with temperature for a given load, assuming the the same wear regime.

It is evident from Figure 5.4 that for 200°C there is a discontinuity in the curve at approximately 44N. This is due to the increase in surface conductance of the pin, caused by the change in wear regime from one of purely oxidational wear, below the transition load of 44N, to one of predominantly metallic wear above the transition. Between 44N and 50N there is an incremental increase in the division of heat of about 10%. All subsequent experimental points lie on a 'new curve'.

5.2.2 Surface Model for a Pin-on-Disc Geometry

In order to deduce the contact temperature (T_o) of the

sliding bodies consider a surface model of N circular contacting asperities beneath the pin of average radius (a). Hence the total real contact area (A_r) is

$$A_r = N\pi a^2 \qquad \ldots(5.8)$$

For plastic deformation A_r is given by (Bowden and Tabor, 1954):

$$A_r = W/P_m \qquad \ldots(5.9)$$

where W is the applied load and P_m is the hardness of the softer material (the pin)

$$\therefore\ N\pi a^2 = W/P_m \qquad \ldots(5.10)$$

We suppose that on each asperity there is an oxide film of thickness ξ in the case of the pin and ξ^* in the case of the disc. It has been shown elsewhere (31) that for the pin (see Appendix 3).

$$T_o = T_s + \frac{H_1}{N\pi K_{sp} a} + \frac{H_1 \xi}{N\pi K_o a^2} \qquad \ldots(5.11)$$

where K_{sp} and K_o are the thermal conductivities of the pin material and the oxide respectively.

In previous analysis (54-56) the oxide film thickness (ξ^*) on the disc has always been neglected. However, SEM measurements have shown that in the case of oxidational wear, ξ and ξ^* are of the same order (see Section 4.6.4). It is reasonable to assume that in the case of the disc (the moving body) the expression for the contact temperature will be of the same form as equation (5.11). However, a parameter which depends on the speed, average contact size and material properties of the contact must be incorporated into the equation. It is therefore postulated that for the disc

$$T_o = T_D + \frac{\alpha(UF - H_1)}{N\pi K_{sd} a} + \frac{\alpha(UF - H_1)}{N\pi a^2 K_o} \xi^* \qquad \ldots(5.12)$$

where T_D is the bulk surface temperature of the disc, $(UF - H_1)$ is the heat flowing per second into the disc from the pin-disc interface and K_{sd} is the thermal conductivity of the disc material. The dimensionless parameter α is related to the dimensionless quantity $L = Ua/2\chi$, where χ is the thermal diffusivity of the medium in which sliding occurs.

The calculations of Holm (57,58) show that α ranges from approximately 0.85 at L = 0.1 to about 0.35 at L = 5. In addition, it can be concluded from Archard (24), that for the range $0.1 < L < 9.0$, α varies approximately linearly with L. Hence $\alpha = mL + c$, where m and c are constants.

Using the above data we find that m = -0.10 and c = 0.86.

$$\therefore \alpha = 0.86 - 0.1L \quad \ldots (5.13)$$

For sliding within oxide films we have, the thermal diffusivity,

$$\chi_o = K_o / \rho_o C_o \quad \ldots (5.13a)$$

where K_o = thermal conductivity of the oxide

ρ_o = the density of the oxide

C_o = the specific heat capacity of the oxide

Hence, α will depend on the oxide properties, which all vary with temperature.

Incorporating equations (5.10) and (5.13) into equations (5.11) and (5.12):

$$T_o = T_s + \frac{P_m H_1 a}{W K_{sp}} + \frac{P_m H_1 \xi}{W K_o} \quad \ldots (5.11a)$$

$$T_o = T_D + P_m (0.86 - Ua/20\chi_o)(UF - H_1)\, a + \frac{P_m(0.86 - Ua/20\chi_o)(UF - H_1)\xi^*}{W K_o}$$

. . .(5.12a)

Equating and collecting coefficients:

$$\frac{P_m U (UF - H_1)}{20W\chi_o K_{sd}} a^2 - \frac{P_m}{W}\left\{\frac{0.86 (UF - H_1)}{K_{sd}} + \frac{H_1}{K_{sp}} - \frac{U(UF - H_1)\xi^*}{20\chi_o K_o}\right\} a$$

$$+ \frac{P_m}{W}\left\{0.86 \frac{(UF - H_1)\xi^*}{K_o} - \frac{H_1 \xi}{K_o} - \frac{(T_s - T_D)}{P/W}\right\} = 0 \quad . . .(5.14)$$

The latter equation is a quadratic in the contact radius (a) of the form $Ax^2 + Bx + C = 0$. Hence, equation (5.14) will have two solutions if $B^2 > 4AC$. The positive root of the equation will yield the contact radius.

In equation (5.14) all the parameters (experimental and material properties) will be known except χ_o, the thermal diffusivity of the oxide. Only estimates are available for K_o, ρ_o and C_o, which all vary with temperature. The density and the specific heat capacity vary in opposition with temperature. Hence the variation in the product $\rho_o C_o$ will be much less significant in the variation of χ_o, compared with the thermal conductivity.

Molgaard and Smeltzer (59) have shown that for hematite and magnetite, K_o varies with absolute temperature (T) according to the equations:

Fe_2O_3 : $K_o = (8.39 - 6.63 \times 10^{-3}\, T)\ WM^{-1}\, K^{-1}$

Fe_3O_4 : $K_o = (4.23 - 1.37 \times 10^{-3}\, T)\ WM^{-1}\, K^{-1}$

Examinations of the wear debris using EDAX revealed that approximately $\frac{3}{4}$ of the oxide was iron (Section 4.6.5). In addition, the oxide debris consisted of mainly the rhombohedral and spinel

oxide phases of the Fe - Cr system (Section 4.4). Hence the above expressions can be used as guide lines in the calculations. However, it is better to use the value of K_o which gives the best agreement between the experimental division (δ_{exp}) and the theoretical division of heat (δ_{th}). Where δ_{exp} is given by equation (5.7) and

$$\delta_{th} = t_d / (t_p + t_d) \quad \ldots (5.15)$$

Following Archard's approach (24) t_d is the 'fictitious' flash temperature obtained with a heat flow rate of UF supplied to the disc only and t_p is a similar temperature deduced on the assumption that the heat is supplied at that rate to the pin only. The expressions for the 'ficticious' temperatures are

$$t_d = \frac{\alpha P_m UFa}{W K_{sd}} + \frac{\alpha P_m UF \xi^*}{W K_o} \quad \ldots (5.16)$$

$$t_p = \frac{P_m UFa}{W K_{sp}} + \frac{P_m UF \xi}{W K_o} \quad \ldots (5.17)$$

5.2.3 Calculation of T_o, N and a

In the calculations the variation of the physical parameters with temperature was allowed for, as far as possible. The bulk hardness (P_m) of the pin material (see Figure 5.5) was taken at the bulk surface pin temperature (T_s), using figures from the hardness response with temperature of a material with similar specification to Brico 65 (60). The thermal conductivity of the disc material (21 - 4N) was taken at T_D and a mean value of the thermal conductivity (26.8 $Wm^{-1} K^{-1}$) in the temperature range 20-500°C was used for Brico 65. For the product $\rho_o C_o$, a value of 4.5×10^6 $Jm^{-3} K^{-1}$, based on the densities and specific heat capacities of iron and chromium oxides

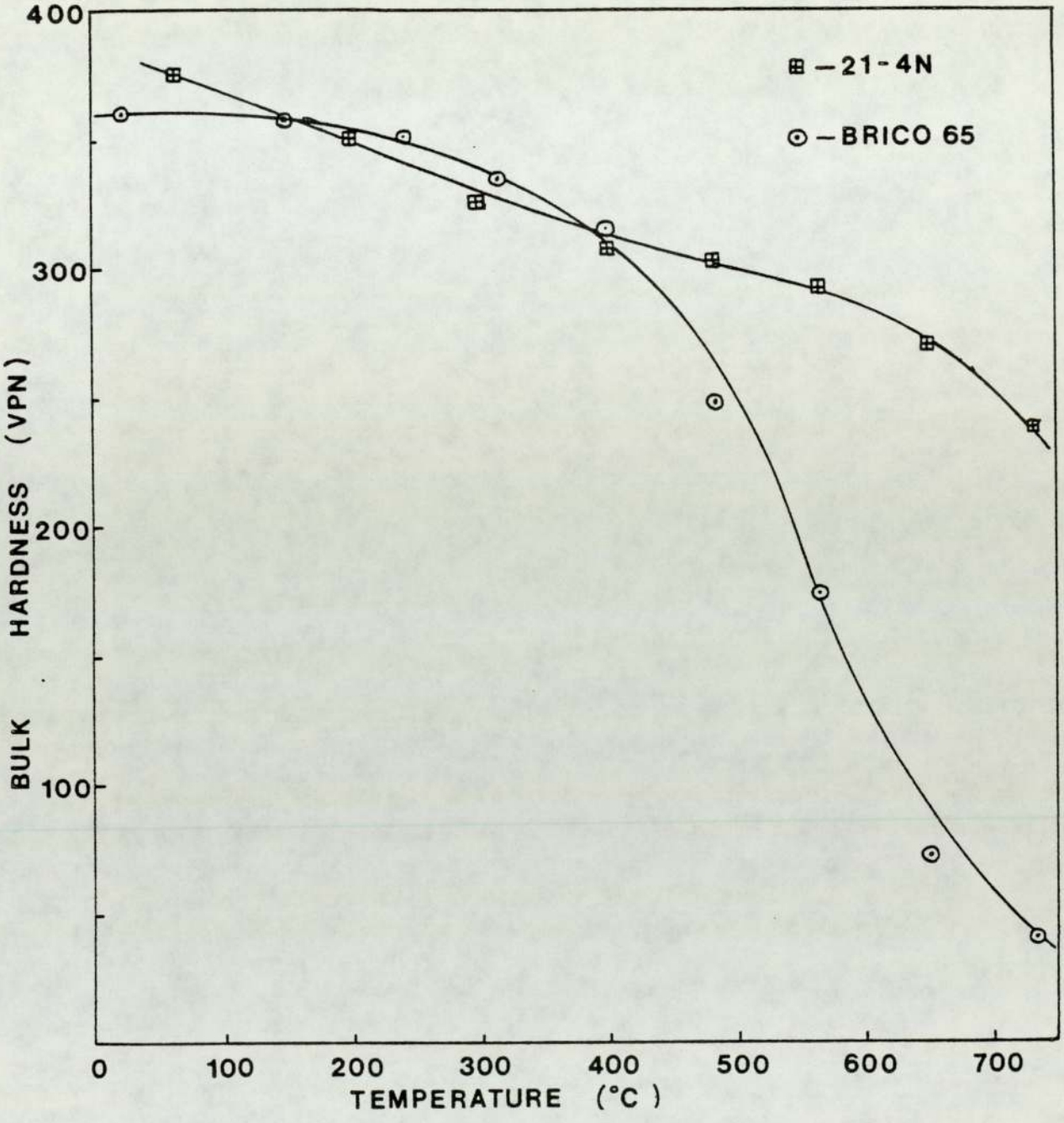

FIGURE 5.5 The variation of Bulk Hardness with Temperature.

(Fe_2O_3, Fe_3O_4 and Cr_2O_3) was used (61).

In a typical calculation, a value of K_o, based on the oxide which predominated in the wear debris, (along with the other parameters) was used to find the coefficients A, B and C in equation (5.14). It turns out that for these oxidational wear experiments, the coefficients A and B are always positive, however, C is always negative. Since the required value of contact radius must be such that $0 < Ua/2\chi_o < 8.6$, the positive solution to equation (5.14) is appropriate. The contact radius was therefore found from the expression

$$a = -B + \frac{(B^2 - 4AC)^{\frac{1}{2}}}{2A} \quad \ldots (5.17)$$

The theoretical division of heat (δ_{th}) was then computed and compared with the experimental division of heat (δ_{exp}). When the best agreement between theory and experiment was obtained, the value for the contact radius was used to calculate the number of contacting asperities (N) and the contact temperature (T_o).

A typical calculation is illustrated by the following:

Taking the 62.5N, 3.3 m/s experiment we have UF = 60.74W, H_1 = 5.52W, δ_{exp} = 9.1%, T_s = 199°C, T_D = 70°C, $P_m/W = 5.65 \times 10^7$ N/m^2, $\xi = \xi^* = 3.5\ \mu$m, K_{sp} = 26.8 W m^{-1} K^{-1}, K_{sd} = 15.0 Wm^{-1} K^{-1}

Assume K_o = 4.0 Wm^{-1} K^{-1}, thus $\chi_o = K_o/\rho_o C_o = 8.826 \times 10^{-7}$ m^2 s^{-1}

Hence

$$A = \frac{P_m U (UF - H_1)}{20W\chi_o K_{sd}} = 3.887 \times 10^{13}$$

$$B = \frac{-P_m}{W}\left\{0.86\ \frac{(UF - H_1)}{K_{sd}} + \frac{H_1}{K_{sp}} - \frac{U(UF - H_1)\xi^*}{20\chi_o K_o}\right\} = 2.95 \times 10^8$$

$$C = -\left\{\frac{P_m}{W}\left(0.86\ \frac{(UF - H_1)\xi^*}{K_o} - \frac{H_1\xi}{K_o}\right) - (T_s - T_D)\right\} = -1.846 \times 10^3$$

$4AC = -28.705 \times 10^{16}$, $B^2 = 8.703 \times 10^{16}$. This yields a value of (a)=4.07 μm and $\alpha = (.86 - Ua/20\chi_o) = 0.1$. Hence from equations (5.15), (5.16) and (5.17) $\delta_{th} = 10\%$. If we assume that $K_o = 4.2\ Wm^{-1}K^{-1}$, this gives $A = 3.702 \times 10^{13}$, $B = 2.48 \times 10^{8}$ and $C = 1.752 \times 10^{3}$. These values yield 4.3 μm for the contact radius. This in turn gives a value for the theoretical division of heat of 9.6%, compared with an experimental division of heat 9.1%. There is good agreement between theory and experiment and the iteration process is therefore halted. A contact radius value of 4.3 μm subsequently yields 305 contacting asperities and a contact temperature of $509^{o}C$.

The variation of the surface parameters with load at sliding speeds of 2.0 and 3.3 m/s are given in Tables 5.4 (a) and (b). For the 2 m/s results there is a gradual decrease in oxide thermal conductivity with increasing load (increasing temperature). Considering the errors in the experimental measurements, particularly the error in the experimental division of heat, the agreement between δ_{exp} and δ_{th} is reasonable. In contrast, the 3.3 m/s results indicate that there is negligible variation in K_o with increasing temperature. The agreement between δ_{th} and δ_{exp} appears to be fairly good.

Graphs of (1) the number of contacting asperities (N) and (2) the average contact radius (a), versus load are shown in Figures 5.6 (a) and (b) respectively, for the above sliding speeds. It is obvious that the number of contacts, N, is directly proportional to the load. The constant of proportionality is dependent on the wear regime and the sliding speed. Figure 5.6 (b) indicate that the contact radius is approximately constant at 4.3 μm for all loads at 3.3 m/s. At 2 m/s (a) is constant at about 8.75 μm for loads up

Load (newtons)	K_o ($Wm^{-1}\ ^oC^{-1}$)	a(μm)	δ_{exp} (%)	δ_{th} (%)	N	T_o (^oC)
12.5	5.0	9.15	9.8	4.2	13	319
31.25	5.0	8.9	11.6	6.8	36	452
37.5	4.9	8.9	7.7	5.0	43	315
50.0	4.8	8.58	8.3	6.7	61	413
62.5	4.8	8.4	10.5	7.0	80	519
67.0	4.5	7.9	11.6	9.5	97	437
75.0	4.2	7.3	14.0	12.6	131	509
81.25	4.2	7.3	13.0	12.6	142	516
87.5	4.2	7.3	12.8	12.6	153	511

Table 5.3 (a) The Variation of Various Surface Parameters with Load at 2.0 m/s .

Load (newtons)	K_o ($Wm^{-1}\,{}^oC^{-1}$)	a(μm)	δ_{exp}(%)	δ_{th}(%)	N	T_o(^oC)
7.0	4.2	4.38	11.2	8.4	33	350
25.00	4.2	4.44	8.8	7.5	114	441
31.25	4.2	4.50	7.2	6.5	133	392
37.50	4.2	4.40	8.1	7.8	175	498
43.75	4.2	4.40	8.2	7.8	204	524
56.25	4.2	4.43	7.4	7.6	258	519
62.50	4.2	4.07	9.1	9.6	305	509
69.75	4.2	4.35	7.9	9.0	332	546
75.00	4.2	4.14	11.1	12.8	394	623

Table 5.3 (b) The Variation of Various Surface Parameters with Load at 3.3 m/s.

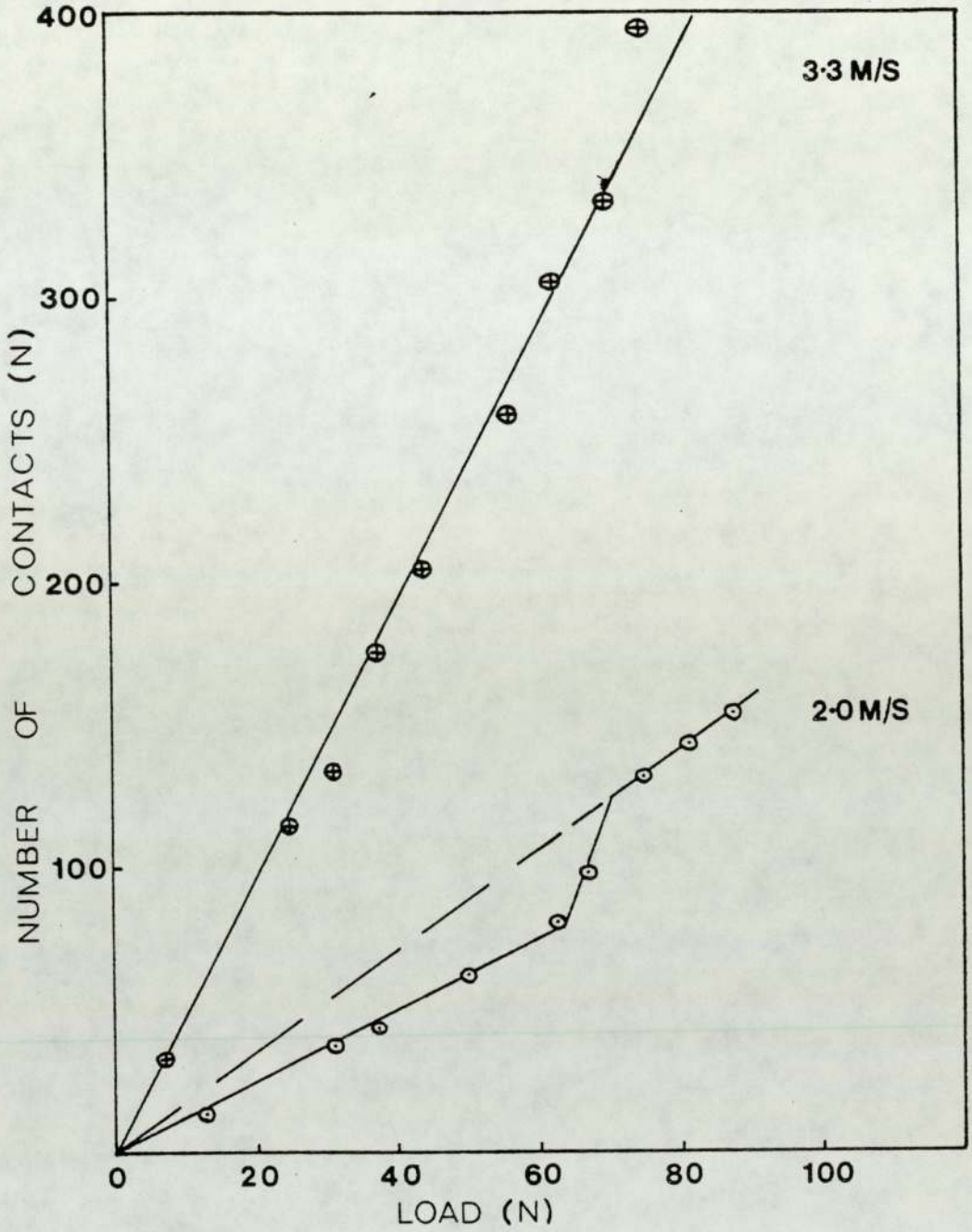

FIGURE 5.6 (a) Number of Contacts versus Load at 2 and 3.3 m/s.

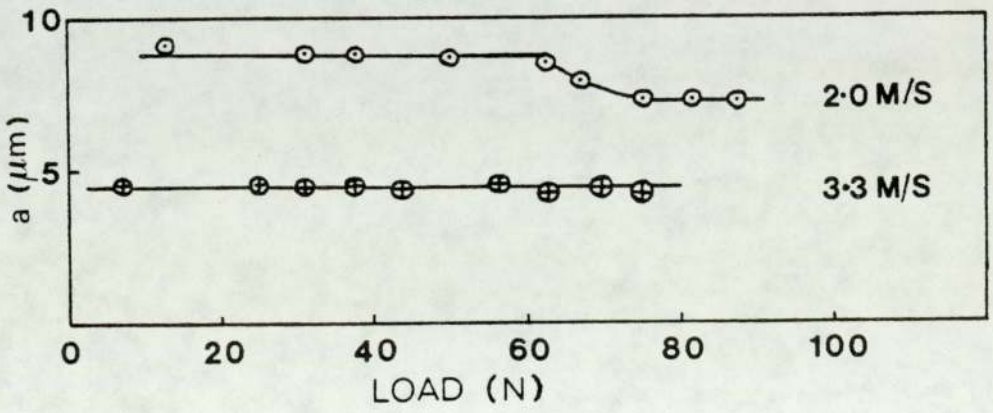

FIGURE 5.6 (b) Mean Contact Radius versus Load at 2 and 3.3 m/s.

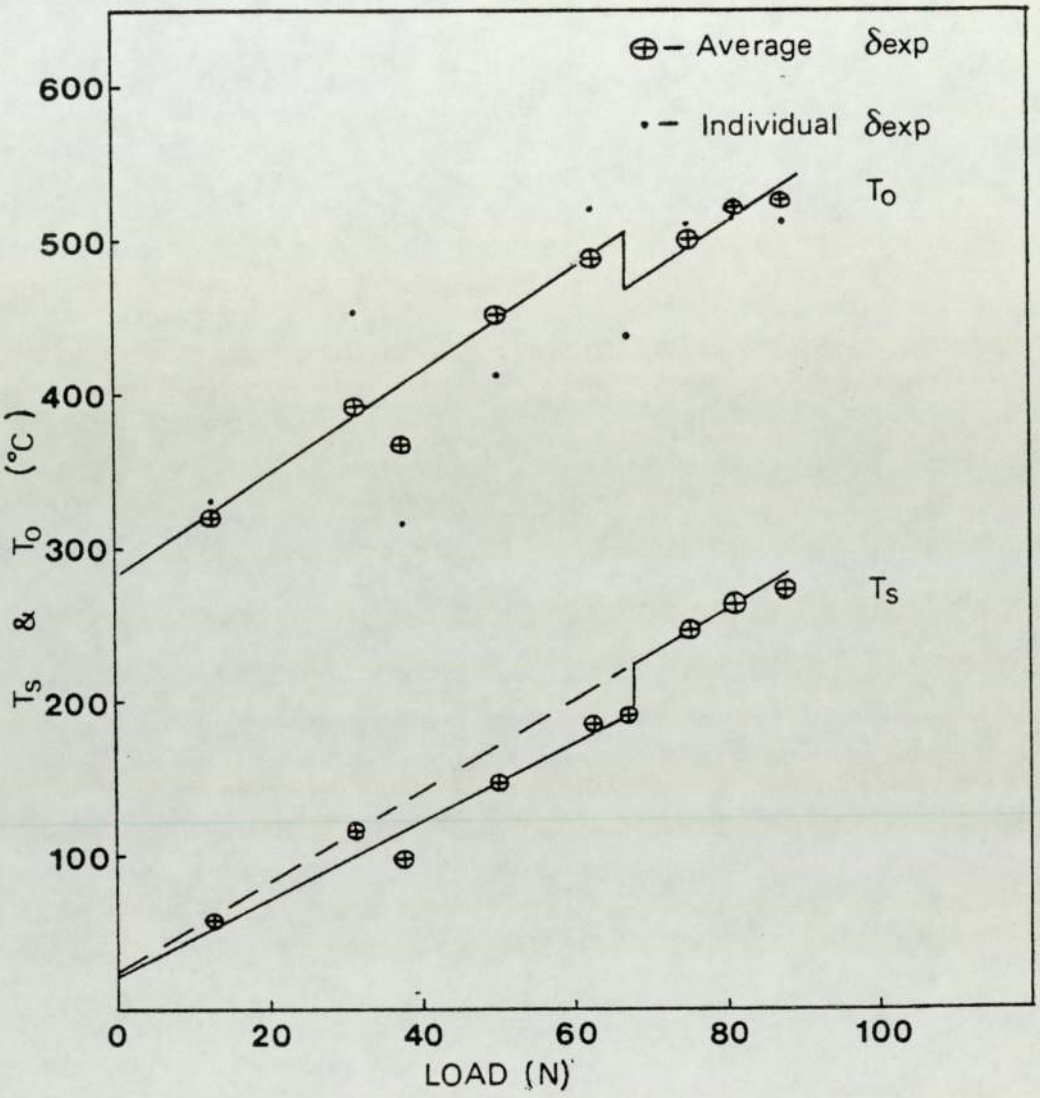

Figure 5·7 Variation of Contact Temperature and Bulk Surface Pin Temperature with Load at 2m/s.

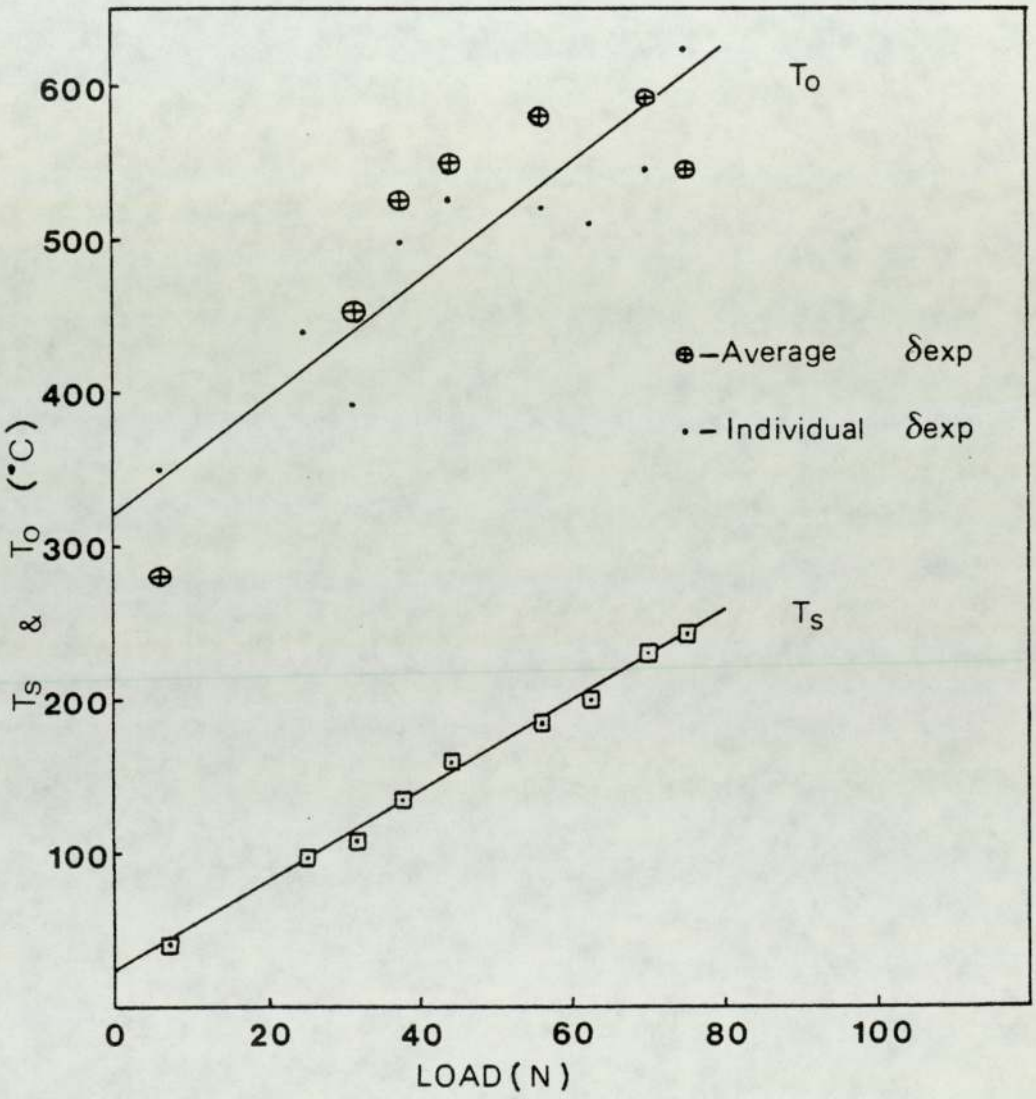

FIGURE 5.8 Variation of Contact Temperature and Bulk Surface Pin Temperature with Load at 3.3 m/s.

to 62.5 N. With increasing load it decreases to a constant value of 7.3 μm at, and above 75 N. This corresponds to a change in wear mode from purely oxidational wear below the transition load of 67 N to metallic/oxidational wear above this load.

The variation of contact temperature (T_o) with load at 2 m/s and 3.3 m/s is shown in Figures 5.7 and 5.8 (T_s is also included for comparison). The results suggest that T_o varies linearly with load, in the same manner as T_s. Since there is considerable scatter in the experimental division of heat, (Figure 5.2) for each load the contact temperature was calculated using both the actual δ_{exp} value and also the mean. In the case of the 2 m/s experiments the line of best fit, for the points calculated from the individual δ_{exp} values, appears to pass through the points calculated from the average value of this quantity (see Figure 5.7). For the 3.3 m/s experiments the calculation of T_o from the individual $\delta_{exp's}$ give a reasonable straight line fit, with less scatter in the points compared with the 2 m/s experiments.

5.3 Quinn's Oxidational Wear Theory

Essentially, the oxidational wear theory as proposed by Quinn (20) states that under conditions of mild oxidational wear, the wear rate (w) of one member of a sliding pair of steels is given by the equation

$$w = \frac{Wd\,A_p}{P_m U f^2 \rho^2 \zeta^2} \exp\left(-Q_p/R(T_o + 273)\right) \qquad \ldots (5.18)$$

where all the symbols have already been defined in Section 1.4.4.

The detail derivation and discussion of this equation has been dealt with elsewhere (20, 31). According to this theory, the

oxide contacts at temperature T_o, grow in thickness until the oxide film reaches a critical value of ξ, at which it becomes mechanically unstable and breaks away from the substrate, thus forming a wear fragment. It is assumed in the theory that the oxide film growth is controlled by a diffusion process in which the mass uptake of oxygen (Δm) to form the oxide occurs at a parabolic rate with respect to time (t), i.e. $\Delta m^2 = k_p t$, where $k_p = A_p \exp(-Q_p/R(T_o + 273))$; is the parabolic rate constant. Furthermore, following the Archard approach (19), 1/K encounters are necessary to produce a wear particle, where of course K is the probability of producing a wear particle at a given oxide contact.

Previous applications of equation (5.18) to the sliding wear of low alloy steel (55) have assumed that the activation energy (Q_p) as derived from static oxidation experiments, (62 - 63) for parabolic oxidation, is directly applicable to a tribological situation in which the same oxide phases are formed. However, the Arrhenius constant (A_p) for tribo-oxidation will be very different and has been derived by the use of friction, wear and heat flow results from continuous sliding experiments with similar steels (55).

In the proceeding section a technique based on equation (5.18) is used to derive tribological values of A_p and Q_p for Brico 65 sliding on 21 - 4 N, under mild wear conditions. This assumes the validity of the experimental measurements and deduced surface parameters from the preceeding sections of the thesis.

According to the oxidational theory of mild wear (20) the Arrhenius constant (A_p) and the activation energy (Q_p) will both depend on the type of oxide which is predominant in the wear process and these values of A_p and Q_p will be approximately constant

for the range of loads and speeds giving rise to this oxide (54,55). In the case of Brico 65 sliding on 21 - 4N it can be recalled from Chapter 4 that for speeds of 2 m/s and 3.3 m/s the spinel oxide phase of iron and chromium predominated in the wear process below a transition load (see Figure 4.4, Figure 4.5 and Table 4.9).

If equation (5.18) is re-arranged we have

$$\frac{w}{W} = \frac{2\, a\, A_p \exp\,(-Q_p/RT)}{P_m u f^2 \rho 2 \xi 2} \qquad \ldots \quad (5.18a)$$

where the size of the sliding contact, d, has been replaced by twice the average contact radius and T is the absolute temperature ($T = T_o + 273$). Note that the ratio w/W is simply the slope of the wear rate versus load graph for a particular sliding speed. Let the slopes of these graphs at 3.3 m/s and 2 m/s be denoted by k_1 and k_2 respectively. If the experimental and heat flow parameters are substituted into equation (5.18a) for 2 loads at these speeds we have

$$k_1 = \frac{2a_1\, A_p \exp\,(-Q_p/RT_1)}{P_{m1} U_1 f^2 \rho_1^2 \xi_1^2} \qquad \ldots \quad (5.18b)$$

and,

$$k_2 = \frac{2a_2 A_p \exp\,(-Q_p/RT_2)}{P_{m2} U_2 f^2 \rho_2^2 \xi_2^2} \qquad \ldots \quad (5.18c)$$

Dividing the latter equations:

$$\frac{k_1}{k_2} = \frac{a_1 P_{m2}\, U_2\, \rho_2^2\, \xi_2^2}{a_2 P_{m1}\, U_1\, \rho_1^2\, \xi_1^2} \exp\left[- \frac{Q_p}{R} \left\{ \frac{1}{T_1} - \frac{1}{T_2} \right\} \right] \qquad \ldots \quad (5.18\,d)$$

The hardnesses P_{m1} and P_{m2} are both temperature dependent, however,

for Brico 65 at surface temperatures (T_s) below 300°C the variation is negligible (see Figure 5.5). Since we are dealing with the same oxide phase we assume that the densities ρ_1 and ρ_2 are approximately equal for the range of temperatures considered. Furthermore, if $T_1 > T_2$, then $1/T_2 - 1/T_1 > 0$. Equation(5.18d) therefore reduces to

$$\frac{k_1}{k_2} = \frac{a_1 U_2 \xi_2^2}{a_2 U_1 \xi_1^2} \exp\left[-\frac{Q_p}{R}\left\{\frac{1}{T_2} - \frac{1}{T_1}\right\}\right]$$

$$\therefore \ln\left\{\frac{k_1 a_2 U_1 \xi_1^2}{k_2 a_1 U_2 \xi_2^2}\right\} = \frac{Q_p}{R}\left\{\frac{1}{T_2} - \frac{1}{T_1}\right\} \quad \text{and hence}$$

$$Q_p = \frac{T_1 T_2 R}{T_1 - T_2} \ln\left\{\frac{k_1 a_2 U_1 \xi_1^2}{k_2 a_1 U_2 \xi_2^2}\right\} \quad \ldots \quad (5.19)$$

Equation (5.19) can therefore be used to find the activation energy. This value of Q_p can then be substituted into equation (5.18b) or equation (5.18c) to yield the corresponding A_p value.

When Q_p is calculated from the latter equation, the principal errors in the calculation will be due to the errors in the temperatures T_1 and T_2.

The maximum fractional error in the expression $T = T_1 T_2 / (T_1 - T_2)$ is given by

$$\frac{\Delta T}{T} = \pm\left\{\frac{\Delta(T_1 - T_2)}{T_1 - T_2} + \frac{\Delta T_1}{T_1} + \frac{\Delta T_2}{T_2}\right\} \quad \ldots \quad (5.20)$$

where the terms in the numerators represent the errors. To serve as an illustration, consider the following idealised calculation:
If we have $T_1 = 673$ K, $T_2 = 623$ K and $\Delta T_1 = \Delta T_2 = \pm 10$K then the error as given by equation (5.20) is

$$\frac{\Delta T}{T} = \pm\left(\frac{20}{50} + \frac{10}{623} + \frac{10}{673}\right) = \pm(.4 + .0016 + .0014)$$

$\therefore$ percentage error = 40.30%

Hence the errors in T_1 and T_2 are magnified when the difference in the inverse of these quantities are taken. Clearly, the first term on the right-hand side of equation (5.20) will contribute most to the final error and therefore the difference between the temperatures were kept as large as possible in the calculations. Furthermore, considering the scatter of the points in Figures 5.7 and 5.8, the T_o values used in the calculation were taken from those points which gave the least deviation from the line of best fit, in order to minimise these errors.

The following illustrates a typical calculation: Taking the 25N, 3.3 m/s and the 12.5N, 2 m/s experiments we have, $k_1 = 0.8 \times 10^{-14}$ m^3/mN, $k_2 = 1.1 \times 10^{-14}$ $m^3/m\ N$; $U_1 = 3.3$ m/s, $U_2 = 2.0$ m/s; $R = 8.3$ J mol^{-1} k^{-1}; $a_1 = 4.44\ \mu m$, $a_2 = 9.15\ \mu m$; $\xi_1 = 3.5\ \mu m$, $\xi_2 = 3.24\ \mu m$; $T_1 = 714K$, $T_2 = 592$ K.

Using equation (5.19) we have

$$\ln\left\{\frac{k_1\ a_2\ U_1\ \xi_1^2}{k_2\ a_1\ U_2\ \xi_2^2}\right\} = 1.054\ ,\quad \frac{1}{T_2} - \frac{1}{T_1} = 2.886 \times 10^{-4}$$

and hence $Q_p = 30.3$ kJ/ mole

This value of Q_p yields a corresponding value of $A_p = 5.1 \times 10^{-2}$ kg^2 m^{-4} s^{-1}. The values of A_p and Q_p obtained by choosing various experimental pairs and performing the above calculations are shown in Table 5.4. The activation evergy values lie within a reasonable range considering the errors involved in the calculations, however, there is a lot more variation in the A_p values. This is due to the

Experimental Pair	A_p (k_g^2 m^{-4} s^{-1})	Q_p(kJ/mole)
25N, 3.3m/s - 12.5N, 2m/s	5.1×10^{-2}	30.3
56N, 3.3m/s - 50N, 2m/s	1.9×10^{-1}	42.3
56N, 3.3m/s - 12.5N, 2m/s	6.9×10^{-3}	20.5
37.5N, 3.3m/s - 12.5N, 2m/s	1.0×10^{-2}	22.5
44N, 3.3 m/s - 12.5N, 2m/s	6.6×10^{-3}	20.3
44N, 3.3 m/s - 50N, 2m/s	1.5×10^{-1}	40.9
Average value	6.9×10^{-2}	29.5
Standard Deviation	8.1×10^{-2}	10.1

Table 5.4 Values of Arrhenius constant and activation energy for Brico 65 sliding on 21 - 4N disc at 2 m/s and 3.3 m/s (mainly Fe - Cr spinel oxide, some Fe-Cr rhombohedral oxide).

fact that moderate variations in Q_p result in larger variations in the exponential term and hence in the Arrhenius constant.

5.4 'Out-of-Contact' Oxidation

As the bulk surface temperature (T_s) increases, oxidation at areas of the sliding specimens which are not in actual contact becomes increasingly important. In particular, when external heating is applied to the specimens the combined effect of the former and frictional heating can cause relatively high bulk surface temperatures. Quinn's original theory as described by equation (5.18) must therefore be modified to take 'out-of-contact' oxidation into account.

Consider a wear machine of pin-on-disc geometry. Furthermore assume that an equilibrium oxidational wear regime has been attained and that we have a uniform distribution of circular asperities of diameter d. Following the Archard approach (19) we define K* as the probability of producing a wear particle per revolution of the disc. Inversely, the number of revolutions needed to form a wear particle will be $1/K^*$, where the latter may be expressed as

$$\frac{1}{k^*} = \frac{t}{t_r} \qquad \ldots . (5.21)$$

where t is the time of oxidation leading to the formation of a detached oxide fragment and t_r is the time for one revolution.

If under a given normal load W there are N contacts between pin and disc at any instant, then the number of contacts per unit area is given by

$$n = \frac{4N}{\pi D^2} \qquad \ldots (5.22)$$

where D is the diameter of the pin. Using equation (5.22), the number

of disc asperities which will encounter those on the pin every revolution is

$$2\pi RD \frac{4N}{\pi D^2} = \frac{8RN}{D} \quad \ldots \quad (5.23)$$

where R is the mean radius of the wear track. The number of asperities on the wear track in an annulus of width d is therefore (8RN/D) x (d/D) and hence each asperity on the pin will make

$$m = \frac{8RNd}{D^2} \quad \ldots \quad (5.24)$$

encounters per revolution.

We are now in a position to relate the so called Archard K factor to K*. Since 1/K* revolutions are needed to produce a wear particle, then the corresponding number of encounters required to produce an oxide fragment is given by

$$1/K = 1/K^*\left(\frac{8dRN}{D^2}\right) \quad \ldots \quad (5.25a)$$

Hence the probability of producing a wear particle at a contact is

$$K = K^* \frac{D^2}{8RdN} \quad \ldots \quad (5.25\ b)$$

Let T_C be the contact temperature and T_s be the "out-of-contact" temperature of the asperities. T_s will be representative of the general surface temperature. The oxidation time for one revolution is given by

$$t_r = t_{rc} + t_{rs} = \frac{2\pi R}{U} \quad \ldots \quad (5.26)$$

where t_{rc} is the time of oxidation at the temperature (T_c), t_{rs} is the time of oxidation at the temperature (T_s) of the contact per revolution and U is the linear sliding speed. The time for which two opposing asperities are in contact is given by

$$\tau = \frac{d}{U} \quad \ldots \quad (5.27)$$

From equations (5.24) and (5.27) the contact time per revolution is given by

$$t_{rc} = \frac{8RN}{U}\left(\frac{d}{D}\right)^2 \quad \ldots\ldots (5.28)$$

Hence the time of oxidation at the contact temperature T_c is

$$t_c = \frac{1}{K^*} t_{rc} = \frac{d}{UK} \quad \ldots\ldots (5.29)$$

from equations (5.25b) and (5.28). The out of contact time per revolution is given by

$$t_{rs} = \frac{2\pi R}{U} - \frac{8RNd^2}{U D^2} \quad \ldots\ldots (5.30)$$

Hence the time of oxidation at the general surface temperature (T_s) is

$$t_s = \frac{1}{K^*} t_{rs} = \frac{D^2}{4UdK} - \frac{d}{UK} \quad \ldots\ldots (5.31)$$

For relatively thick oxide films the oxide growth rate can be assumed to follow a parabolic rate law (64), namely $\Delta m^2 = k_p t$. Hence for the mass uptake of oxygen at the contact temperature (T_c) we have the expression

$$\Delta m_c^2 = k_p (T_c)\, t_c \quad \ldots\ldots (5.32a)$$

and at the general surface temperature (T_s)

$$\Delta m_s^2 = k_p (T_s) t_s \quad \ldots\ldots (5.32b)$$

where $k_p(T_c)$ and $k_p(T_s)$ are the parabolic rate constants at the respective temperatures and are given by

$$k_p(T_c) = A_p (T_c) \exp\left(- Q_p(T_c) / R T_c\right) \quad \ldots (5.33a)$$

$$k_p(T_s) = A_p(T_s) \exp\left(- Q_p(T_s) / R T_s\right) \quad \ldots (5.33b)$$

The mass uptake of oxygen is also related to other oxide parameters, namely,

$$\Delta m_c = f(T_c)\, \rho (T_c)\, \xi_c \quad \ldots\ldots (5.34a)$$

$$\Delta m_s = f(T_s)\,\rho\,(T_s)\,\xi_s \quad \ldots\ldots (5.34b)$$

where f is the fraction of the oxide which is oxygen, ρ is the density of the oxide and ξ_c, ξ_s are the oxide thicknesses produced during contact and "out-of-contact" respectively. Clearly the critical oxide film thickness (ξ) is given by

$$\xi = \xi_c + \xi_s \quad \ldots\ldots (5.35)$$

Squaring the latter equation:

$$\xi^2 = \xi_c^2 + 2\,\xi_c \times \xi_s + \xi_s^2$$

Substituting from equations (5.34a) and (5.34b):

$$\xi^2 = \frac{\Delta m_c^2}{f^2(T_c)\rho^2(T_c)} + \frac{2\,\Delta m_c\,\Delta m_s}{f(T_c)f(T_s)\rho(T_c)\rho(Ts)} + \frac{\Delta m_s^2}{f^2(T_s)\rho^2(Ts)} \quad \ldots (5.36)$$

Substituting for the Δm terms:

$$\xi^2 = \frac{k_p(T_c)\,d}{KUf^2(T_c)\rho^2(T_c)} + \frac{2\,(k_p(T_c)\,k_p(T_s))^{\frac{1}{2}}}{KUf(T_c)f(T_s)\rho(T_c)\rho(T_s)} \left(\frac{\pi D^2}{4N} - d^2\right)^{\frac{1}{2}}$$

$$+ \frac{k_p(T_s)}{f^2(T_s)\rho^2(T_s)UK} \left(\frac{\pi D^2}{4dN} - d\right) \quad \ldots\ldots (5.37)$$

Hence the Archard K factor is given by

$$K = \frac{k_p(T_c)d}{\xi^2 f^2(T_c)\rho^2(T_c)U} + \frac{2(k_p(T_c)k_p(T_s))^{\frac{1}{2}}}{U\xi^2 f(T_c)f(T_s)\rho(T_c)\rho(T_s)} \left(\frac{\pi D^2}{4N} - d^2\right)^{\frac{1}{2}} +$$

$$\frac{k_p(T_s)}{U\xi^2 f^2(T_s)\rho^2(T_s)} \left(\frac{\pi D^2}{4dN} - d\right) \quad \ldots\ldots (5.38)$$

where the parabolic rate constants $k_p(T_c)$ and $k_p(T_s)$ are given by equations (5.33a) and (5.33b). The latter expression for K may be substituted into the equation $w = KW/P_m$ to yield an expression for

the theoretical wear rate. It can be seen that when the 'out-of-contact' oxidation is negligible then the last 2 terms in equation (5.38) disappear and it reduces to Quinn's original expression for the K factor.

So far, the unavailability of static oxidation constants for Brico 65 and 21 - 4N has hampered the application of this modified theory to these materials. However, the theory has been applied to low alloy steels and the correlation with experiment has been very reasonable (65).

CHAPTER 6

DISCUSSION

6.1 Introduction

The wear and to a lesser extent friction of Brico 65 sliding on 21 - 4N is discussed with reference to the appropriate wear mechanisms ((1) Oxidational Wear and (2) Transfer followed by Abrasive Wear), in the light of considerable experimental evidence reported in Chapter 4.

The effect of oxide films and subsurface metallurgical changes on wear are considered in detail.

The heat flow results are also discussed and interesting comparisons with the wear results are made.

In addition, the parabolic rate constants (A_p and Q_p) deduced from the heat flow results and the oxidational wear equation in Chapter 5 are compared with the oxidation constants used for other materials during wear.

6.2 Wear Behaviour

In general, under all conditions of unlubricated sliding the mechanisms which are prevalent in the wear process are (1) Oxidational Wear and (2) Transfer (Adhesion) followed by Abrasive Wear.

The wear behaviour at 0.23 m/s is an exception to the general pattern. In this case a metallic/oxidational wear mode is observed. At this low sliding speed the rate of oxidation is insufficient to achieve complete protection of the alloys by an oxide film. Hence, there is some inter-metallic contact which results in considerable alloy damage (Figure 4.14) and consequently, the wear debris is of a metallic/oxide nature (Table 4.8 (a)).

6.3 Oxidational Wear

Relatively low wear rates (less than 10^{-12} m^3/m) are a characteristic feature of this wear mode. It is evident from Figures 4.3, 4.4, 4.5 and 4.9, that at lower ambient temperatures oxidational wear is predominant for sliding conditions below a transition load. At higher ambient temperatures (induced by external heating) the oxidation rate is sufficient to completely suppress the transitional behaviour and the wear is purely oxidational (Figure 4.10).

The wear surface topographies of the sliding members are very similar in character, consisting of numerous oxide plateaux. Due to the sliding process the surfaces have a very smooth appearance (Figures 4.15 (a), (b), (c), (d), (e)). Stott et. al. (14, 66) have reported the formation of 'glaze' oxide layers produced on alloys during wear at high temperatures. In their work the 'glaze' layer is seen to lie on top of a region either of highly compacted oxide particles above a growing steady-state oxide layer, or of alloy, deformed to varying degrees . The wear surface topographies exhibited in the present work appear to be similar to those reported by Stott et. al. However, the difference lies in the development of the protective oxide films. It is instructive to recall that in the present work the geometry of the test specimens was that of a horizontal pin on a vertical disc (Figure 3.1). Hence, the majority of the loose oxide particles formed will fall away from the sliding interface due to gravity. Therefore, very few loose oxide wear particles will be trapped on the surfaces. In the work reported by Stott et. al. a horizontal test plate was used and the sliding was not continuous but reciprocating. Under these conditions any loose wear particles which are formed cannot easily escape and can therefore be further

fragmented during sliding, giving rise to a smooth wear topography above an agglomeration of oxide particles. It is evident from Figures 4.18 that the oxide films formed are fairly homogeneous in character, with no evidence of oxide particle agglomeration.

Under conditions of mild oxidational wear the growth of the oxide film is controlled by a parabolic rate law (20). This involves the inward diffusion of oxygen ions and the outward diffusion of metal ions (64, 67). For alloys consisting of a number of elements, such as Brico 65 and 21 - 4N, the diffusion process is of a complex nature. Alloying elements of minor concentrations such as silicon can affect the diffusion rates of the major elements (iron and chromium). Figure 4.16 shows a section of an oxide plateau with the X-ray distribution maps of silicon, iron and chromium. It is clear that the concentration of silicon in the plateau is far greater than its bulk concentration (approximately 2%). Selective diffusion of silicon has therefore taken place. Svedung and Vannerberg (68) have found that under static conditions silicon has a marked effect on the oxidation of iron. The X-ray maps also shown that there is a greater amount of iron in the oxide in comparison to chromium (approximately in the same ratio as the bulk concentrations). In the case of binary alloys of iron and chromium, selective diffusion of chromium occurs (69,70). In the present investigation, the physical methods of analyses suggest that selective diffusion of silicon occurs and iron is bonded with chromium in solid solutions of the rhombohedral and spinel oxide phases (as indicated by the X-ray diffraction results).

6.3.1 Mechanism of Oxide Film Rupture

Aronov (71, 72) has attributed the destruction of the

oxide film to a fatigue process at the oxide/metal interface. The fatigue mechanism involves thermal and mechanical stresses within the oxide and at the oxide/metal boundary. Oxide elements under repeated stress subsequently develop cracks and eventually become detached as loose wear fragments. Figure 4.15 (g) shows a section of an oxide plateau, for a test specimen after wear at 400°C (disc temperature), 100N and 2 m/s. Note the cracks within the oxide, and the oxide elements which are raised above the general surface, about to be removed as wear fragments. In regions where the oxide elements have been completely detached the underlying metal can be seen. This is clearly an example where fracture has occurred at the oxide/metal interface. In Figure 4.15 (h), an element of oxide is lifted well above the general surface. Fracture appears to have occurred within the oxide itself, yielding a much thinner fragment than in the previous example.

6.3.2 Effect of Oxide film thickness on Wear

It is interesting to note that the thickness of the oxide films produced on both Brico 65 (pin) and 21 - 4N (disc), under conditions promoting mild oxidational wear are of the same order (Table 4.12). This appears to be a characteristic feature of this wear mode and the estimated disc wear rates although not determined as accurately as the pin wear rates, would indicate that the wear of both materials is of the same order of magnitude (Table 4.6).

Increased oxidation (in and out of contact) at elevated temperatures increases the equilibrium oxide film thickness (Table 4.12) which has the beneficial effect of decreased wear rates. This is clearly demonstrated by the results given in Table 4.5 (excluding the transitional behaviour at 200°C).

6.3.3 Subsurface Morphology of Brico 65

In the examination of the subsurface morphology of Brico 65, it must be appreciated that the material has a 3 phase microstructure. There is a relatively large finger-like phase and a spheroidal phase which are chromium rich and are scattered around a softer ferrite matrix (Figure 3.5).

Metallographic examination (by taper section), revealed that a homogeneous layer existed between the bakelite (mounting material) and the bulk material. The thickness of this layer (as calculated from the angle of taper) is in agreement with the measured thickness of the oxide film when the surface was directly examined using the SEM. It can therefore be concluded that the observed layer is of oxide character (Figure 4.20). The microstructure just below the oxide film appears to be similar to the bulk structure (comparing Figures 3.5 and 4.20), although in the former case there appears to be some deformation of the material due to the wear process. The X-ray distribution maps in Figures 4.20 (c) and (d) indicate that in the oxide layer the iron and chromium concentration ratio is similar to the bulk value, although there is more of a scatter in the chromium X-ray distribution in the bulk due to the presence of the phases mentioned. The concentration ratio is in agreement with that found in the wear debris.

Micro-hardness measurements indicated that the hardness of the oxide is in the range 750 - 900 VPN, but the hardness of the substrate is of the order of the bulk value of 360 VPN. According to Welsh, (4), for steels, the substrate hardens during running-in until a critical value (340 - 425 VPN) is reached at which point the necessary strength is possessed by the material to support an oxide,

so that fracture will occur within the oxide and therefore mild wear will ensue. From the above results there appears to be negligible hardening of the substrate. It is instructive to recall that for the wear tests carried out at 1 m/s there was a lengthy period of severe metallic wear, before mild oxidational wear occurred. In contrast, at the higher speeds the severe wear period was of a much shorter duration before mild oxidational wear ensued. This indicates that the rate of oxidation is as important as hardness considerations during wear. Under conditions of purely mild oxidational wear, when relatively thick films are formed, the rate of oxidation may be more important.

6.4 Transfer followed by Abrasive Wear

The experimental evidence in Chapter 4 suggest that under certain conditions of sliding (above a transition load of 67N and 44N for the non-externally heated wear tests at 2 m/s and the elevated temperature wear tests at a disc temperature of 200°C respectively, and for speeds in the range 2.25 - 3 m/s at a load of 50N)the pin material (Brico 65) is transferred to the disc (21 - 4N) during running-in, subsequently followed by the abrasion of the pin during the equilibrium wear regime. The term "Transfer followed by Abrasive Wear" therefore seems appropriate. A characteristic feature of this wear mode is the relatively high wear rates of Brico 65 in comparison to 21 - 4N (Figures 4.4, 4.6, 4.9 and Table 4.6).

The nature of the wear surface topographies of the sliding members are very dissimilar. In the case of Brico 65, a series of grooves are seen to run parallel to the direction of sliding (Figures 4.17 (a) and (b), showing deformation of the underlying material. This is consistent with the topography of an abraided surface (12, 22).

In contrast, the wear surface of 21 - 4N shows evidence of material transfer(Figures 4.17 (b) and (c)). During the running-in period, it appears that under conditions of high loads (inducing high stresses and strains), there is strong adhesion (8) at the asperity contacts of the sliding members. The stress conditions are such that fracture occurs within the pin material (examination of the wear topographies would indicate that the deformation in Brico 65 is far greater than in 21 - 4N), leaving transferred fragments adhering to the disc surface.

Examination of the wear debris and the worn specimens by X-ray diffraction (powder diffraction and glancing angle respectively) suggest that under these conditions of high strains metallurgical phase transformations occur in the subsurface regions of both Brico 65 and 21 - 4N. It is the nature of these phase transformed materials which determines the subsequent wear behaviour during the equilibrium wear regime. X-ray diffraction of the wear debris revealed that the major constituent in the debris is an austenitic type of material, with the spinel oxide phase and ferrite (or body centred cubic martensite) as the remaining constituents. The ferrite structure could be interpreted as body centred cubic martensite (45) which is encountered when austenitic steels are deformed under condtions of high stresses (46-48). Examination of the wear surfaces of Brico 65 and 21 - 4N by glancing angle X-ray diffraction tend to support the wear debris findings. In the case of Brico 65, a material of an austenitic structure type (plus the spinel oxide phase in addition to ferrite which is the bulk material), is present in the near-surface region. This is probably an unstable form of austenite which becomes more plentiful as the deformation (due to increasing load) is increased

(Figure 4.13). For 21 - 4N, a material of structure similar to ferrite is present in the surface layers. Metallographic examination further suggests that this material is indeed body centred cubic martensite (Figure 4.23). The contrasting wear topographies of the pin and the disc materials suggests that the material formed in the subsurface of 21 - 4N is much harder and more compact in structure than the phase transformed material in Brico 65.

Above the transition load of 67N, for the non-externally heated wear tests at 2 m/s, surface oxidation renders some protection of the pin material (Figure 4.21 (b)). However, the phase transformed material is evident in the subsurface of the alloy (Figure 4.21 (a)). Although there is surface oxidation the relatively high wear rates (greater than 9×10^{-12} m^3/m) for the wear tests at 200°C, above the transition load of 44N, indicate that there is little surface protection of Brico 65. In fact, the oxide is easily penetrated by the disc asperities, yielding a heavily deformed pin surface (Figures 4.17 (d) and (e)). Recalling that the elevated temperature experiments at 200°C were carried out at the same sliding speed (2 m/s) as the above 'room temperature' runs, the shifting of the transition load from 67N at 'room temperature' to 44N at 200°C indicate that the transition load at which the wear regime changes from one of purely oxidational wear to the above regime of abrasion in equilibrium is temperature dependent.

6.4.1 Subsurface Morphology of Brico 65 and 21 - 4N

From the subsurface examination of Brico 65 (by taper section) the occurrence of a phase transformed structure is evident (Figure 4.22). The structure can be interpreted as of austenitic form, using the X-ray diffraction findings. Figure 4.22 would tend to

indicate that the layer is of a patchy nature, being highly worked by the disc asperities during the wear process. There is no evidence of oxide above the layer. This shows that when the structure is well established (as it is at 200°C for loads greater than 44N) any surface oxide which is formed is not very stable. Hence the wear of the pin material for this wear regime is influenced by the behaviour of this transformed layer, rather than surface oxidation during sliding.

The micrograph in Figure 4.22 (b) shows in detail the nature of the transformed layers. It appears to consist of a series of dislocation cells, very similar to the microstructure developed by metals and some ceramics which have been highly deformed during wear, as reported by Rigney and Glaeser (22). The basis of their ideas is the plastic deformation of the near-surface regions of the material, which eventually leads to a change in the subsurface microstructure. The resulting microstructure consists of a series of dislocation cells whose sizes depend on material characteristics such as stacking fault energy, the magnitude of the applied stress and the temperature. Their ideas would therefore, seem applicable to this wear regime. However, the authors (22) have not so far developed a quantitative model to predict wear.

The X-ray distribution map in Figure 4.22 (e) indicate that there is almost a complete depletion of silicon within the transformed material. This suggests that silicon has been transferred to the disc during the wear process.

In contrast to Brico 65, the transformed material in the subsurface of 21 - 4N is of a more compact structure (Figure 4.23 (a)). The X-ray diffraction results indicate that this material has a body centred cubic structure (with the same interplanar spacings as ferrite).

However, hardness measurements show that the layer is very hard (greater than 1000 VPN). Hence this material cannot be ferrite in the normal sense.

Various workers (46-48) have found that on deformation (cold-working) the face centred cubic (f.c.c.) austenitic structure transforms to body centred cubic (b.c.c.) martensite as opposed to the body centred tetragonal martensite formed in ordinary carbon steels. The result of cold-working is a much harder and stronger alloy. This transformed material is analogous to the so called 'white or non-etching layers' formed in the subsurface of steels during sliding, as repeated by Eyre and Maynard (73).

Dumbleton and Douthett (45) have reported that additions of silicon to austenitic stainless steels improve their adhesive wear resistance. The micrograph in Figure 4.23 (b) shows a view of the transformed material, at a greater magnification. The results of the elemental concentration measurements across the layer and into the bulk of the disc material are shown in Figure 4.24. The iron concentration is at a maximum near the surface. Since the transferred silicon and chromium appear to have bonded with the disc material to form an extremely hard phase it follows that the top layers of the transferred fragments are depleted in these elements and therefore richer in iron. The surface species may, therefore, be interpreted as iron rich oxides. The silicon and chromium concentrations are at a maximum within the transformed layer. In addition, the concentration of silicon (2%) in the layer is well above the bulk concentration of silicon (.1 - .2%) in 21 - 4N. This is further evidence of material transfer. It appears that silicon has combined, during the running-in period, with the disc material to form a layer of material which

has very good wear resisting properties. The hardness of this transformed material (>1000 VPN) is much greater than the hardness of the austenitic structure (650 - 800 VPN) formed in the near-surface region of Brico 65. This results in the abrasion of the pin during the equilibrium wear regime.

We are now in a postion to provide an explantion for the shifting of the transition load from 67N at 'room temperature' to 44N at a disc temperature of 200°C and the occurrence of higher wear rates for the latter sliding conditions. The diffusion of silicon to the surface of Brico 65 increases with temperature. Furthermore, if the silicon concentration in the surface of the pin increases, this appears to promote greater transfer of material to the 21 - 4N disc. Hence, during running - in, the critical load at which transfer occurs is lowered at the higher temperature. In addition, it would appear that for the 200°C test runs the transformed phases within the subsurface of pin and disc materials are fully developed. Due to the difference in hardness and strength of these phases the abrasive wear rates of Brico 65 are higher at 200°C, in comparison to the wear rates for the purely frictionally heated experiments (at the same sliding speed).

The reader should be reminded that the rate of oxidation at the higher ambient temperatures, which promotes the formation of protective oxide films, is sufficient to completely suppress this transitional behaviour.

6.5 Friction

It is interesting to note that for all sliding conditions the coefficient of friction (μ) varies over a narrow range (0.3-0.7)

whereas the wear rates range well over two orders of magnitude. This indicates that friction is very much less sensitive to changes at and near the surface during sliding.

The reduction in μ with increased speed (Figure 4.7) can be explained in terms of the adhesion theory (8). At low sliding speeds the rate of oxidation is insufficient to prevent intermetallic contact and hence the force required to shear the asperity junctions is comparatively large. As the speed is increased the oxidation rate increases. This enhances oxide coverage of the alloys; thus reducing the adhesion of the surfaces and allowing sliding to be easier (74).

Saka et. al. (75) have reported similar variations to that found in the present work, of μ with sliding speed, for other materials.

Although three different mechanisms (oxidation, adhesion and abrasion) have given rise to the wear process, the variation of μ with ambient disc temperature (at elevated temperatures) is insignificant. In addition, it would appear from the metallographic examination of the subsurface regions of the worn specimens that near surface deformation, as described by Rigney and Hirth (18) accounts for friction at 200°C for loads above the transition. In order to use the expression developed for μ (equation 1.8) from this model, difficulties of determining the shear stress and the average strain per unit cycle would arise.

The gradual decrease in friction coefficient with load, at elevated temperatures (excluding the results at 200°C, above the transition load) may be explained if the various components giving rise to friction (12) are considered. As the normal load is increased the ploughing and roughness components are reduced since the contacting asperities become flattened under the influence of the applied load.

Hence, on the basis of the adhesion theory, adhesion is the only component giving rise to friction at relatively high loads, for these experiements.

6.6 Heat Flow Analysis and the Oxidational Wear Theory

An interesting feature borne out by the heat flow analysis is the similarity in the variation of wear rate and bulk surface temperature (T_s) with load, under all conditions of sliding. In particular, when there is an abrupt change in the wear rate (Figure 4.9) due to a change in wear regime, there is also an abrupt change in T_s (Figure 5.3). This is not surprising since higher wear rates usually indicate the occurrence of some metallic contact. Whether there is metallurgical phase transformed material in the near-surface regions or not, the absence of protective oxide films (which are low in thermal conductivity) indicate that the surface conductance is higher than would be the case if an oxide film was present. Hence, more heat is conducted into the pin (Figure 5.4). Consequently there is a sudden increase in the bulk surface pin temperature. Quinn et. al. (54, 55) have found similar variations of the wear rate and T_s with load and have attributed the transitional behaviour to changes in the oxide phases formed during wear.

The surface model (Section 5.2.2) predicts that the average contact size is constant for a given wear regime and that the number of contacting asperities beneath the pin varies linearly with load, within the same wear region. This appears to be reasonable because the hardness of the pin material (Brico 65) does not vary greatly for temperatures of up to 400°C (Figure 5.5). In addition, the results indicate that the number of contacts is speed dependent

(Figure 5.6). There seems to be some correlation of the latter with the oxide phases formed. At the higher sliding speed the spinel oxide phase was predominant whereas at the lower speed the oxide was a mixture of the rhombohedral and spinel phases.

The surface model also indicates that there is some correlation between the bulk surface temperature (T_s) and the contact temperature (T_o). The scatter in the results (Figures 5.7 and 5.8) are due to two main sources of errors; errors in the experimental measurements and more important, errors in the parameters used in the calculations, whose variations with temperature are not known to sufficient accuracy. However, the trends in the results are well indicated. If the temperature variations of K_s, K_o and ρ_o become available at a later date, the calculations can be achieved much more accurately. The calculations for the elevated temperature experiments have not been attempted in the present study, the main reason being the increased significance of 'out of contact' oxidation as the external heat input is increased. Such temperatures for the externally heated wear tests will be presumably very high, taking into account the present calculations and the high T_s values (Figure 5.3).

Childs (76) has recently inferred, from the work of Krause (77), that oxide cracking during sliding may provide more rapid transport of metal and oxygen ions to one another, so that diffusion could become irrelevant to film growth. However, the present work clearly demonstrates that oxidation during wear (at least for a pin-on-disc geometry) is a diffusion controlled process. The micrographs in Figure 4.16 (a) and (b) show the presence of silicon rich species within the oxide plateau. The concentration of silicon within the plateau is well above the bulk level of silicon (2%) within the alloy.

This provides clear evidence that oxidation during wear is a diffusion controlled mechanism.

The relatively low values for the activation energy (Q_p) deduced from the wear experiments (Section 5.3) suggest that Q_p in the case of tribo-oxidation is lower than that in the case of static oxidation. This appears to be in conflict with the idea of Quinn et.al. (54-56) that the activation energy as deduced from static oxidation experiments is applicable to oxidation during sliding. However, it should be appreciated that Brico 65 is a complex material, containing significant amounts of chromium and silicon (in addition to iron) which will affect the oxidation process. It would, therefore, be interesting if the calculations in Chapter 5 are repeated for the low alloy steels (EN8 and EN31) to see if there is any correlation between tribological and static $Q_{p's}$.

Tao (78) has deduced activation energies for tribo-oxidation, using his theoretical model, and has found that these values are significantly lower than the corresponding $Q_{p's}$ in the static case. He attributes the differences to a mechanical activation phenomena caused by the action of rubbing. In addition, Molgaard (79) has suggested that the effect of fractures and grain boundaries in oxide layers are significant and should be considered in the oxidational wear process. Fractures and grain boundaries may form surfaces along which oxygen may diffuse or the fractures in pores may be wide enough for molecular oxygen to diffuse in the fracture volumes (79).

Guy and Hren (80) point out that diffusion may result not only from the presence of a concentration gradient, but may also be influenced by an electric field, a temperature gradient or the local state of stress. Furthermore, in addition to lattice (or volume)

diffusion, significant amounts of diffusion may occur by 'short circuits' along grain boundaries or dislocations (81-83). Because the regularity of the crystal lattice of a metal is disturbed at a grain boundary and adjacent to a dislocation line, diffusion by the vacancy mechanism is greatly enhanced in these regions (80). Both the number of vacancies and their mobility may be large as a result of the local disruption of the crystalline regularity. For this reason the activiation energy is less for grain boundary diffusion than for volume diffusion. In the case of metals the activation energy for grain boundary diffusion is approximately one half that for volume diffusion (81). The importance of grain boundary diffusion will, in general, be significant at temperatures below two-thirds the melting point of the polycrystalline material (81).

In the case of oxides, Markali (84) estimated that the grain boundary area amounted to 5 - 10% of the total oxide area. According to Kofstad (81), the ratio of grain boundary to lattice diffusion coefficient is of the order of 10^5 for metals; if this ratio for oxides is of the same order then grain boundary diffusion in the latter will be highly significant.

In a tribological situation, the local stresses will be very high and the crystalline structure of the metal at and near the wear surface may be greatly disrupted. The number of dislocations and hence, the number of vacancies and their mobility will be large. The vacancy mechanism of diffusion therefore seems appropriate. By inference (80-81), the activation energy for parabolic oxidation in a tribological situation may, therefore, be considerably less than in the case of static oxidation. This may explain why the Q_p values derived directly from the wear experiments in Chapter 5 are consider-

ably lower than those deduced from static oxidation experiments. A direct comparison is not however, strictly possible since the static $Q_{p's}$ were applicable to the low alloy steels (54) and not to Brico 65. However, several attempts by the author to deduce A_p and Q_p values from static oxidation experiments have been unsuccessful. After many hours (10 hours) of oxidation the oxidative weight gain of the Brico 65 specimens were not measureable. In wear experiments the material has readily exhibited tribo-oxidation.

CHAPTER 7

CONCLUSIONS

The present investigation has shown that the mechanisms prevalent in the wear of Brico 65 sliding on 21 - 4N are:
(1) Oxidation and (2) Transfer (Adhesion) followed by Abrasion.

In the case of the purely frictionally heated wear tests a transitional wear behaviour is exhibited. Below a transition load, mild oxidational wear occurs. Above this load varying forms of metallic/oxidational wear are encountered. This transitional behaviour is also exhibited at a bulk surface disc temperature of 200°C. At higher ambient temperatures (induced by external heating) the transitional behaviour is completely suppressed and the wear is purely oxidational. This is due to the greater rate of oxidation, in and out of contact, at the higher temperatures.

X-ray diffraction analysis indicate that solid solutions of the rhombohedral and spinel oxide phases play significant roles in the oxidational wear process. Scanning electron microscopy (SEM) studies indicate that for the oxidational wear specimens, the surface topography of both Brico 65 and 21 - 4N are very similar in character, containing numerous oxide plateaux. This is a typical feature of oxidational wear. In addition, SEM shows that both alloys are protected by fairly thick oxide films which lie in the range $2\mu m \leq \xi \leq 5\mu m$ for all experimental conditions promoting oxidational wear. The equilibrium film thickness appears to be more dependent on the sliding speed and the external heat input rather than on load. For the 1 m/s experiments $\xi \simeq 2\,\mu m$ and at 2 m/s $\xi \simeq 3.25\,\mu m$; whereas for the elevated temperature experiments at disc temperatures of 300, 400

and 500°C and a sliding speed of 2 m/s, the film thickness is of the order of (5 ± 1) μm.

The experimental evidence suggest that the wear mechanism of Transfer followed by Abrasion is of most importance for the following experimental conditions: (a) above a transition load of 67N for the non-externally heated wear tests at 2 m/s, (b) wear tests in the speed range 2.25 - 3 m/s for a load of 50N, and (c) of primary importance for wear tests at 2 m/s and a disc temperature of 200°C, for loads greater than 44N. Under these conditions of sliding the pin material (Brico 65) is transferred to the disc (21 - 4N) during 'running-in', subsequently followed by the abrasion of the pin during the equilibrium wear regime. A characteristic feature of this wear mode is the relatively high wear rates of Brico 65 in comparison to 21 - 4N. SEM studies show that the wear surface topographies of the sliding members are very dissimilar. In the case of Brico 65, a series of grooves are seen to run parallel to the direction of sliding, showing deformation of the underlying material. This is consistent with the topography of an abraided surface. In contrast, the wear surface topography of 21 - 4N shows evidence of material transfer. During the 'running-in' period under conditions of high loads there is strong adhesion at the asperity contacts of the sliding members. The stress conditions are such that fracture occurs within the pin material, leaving transferred fragments adhering to the disc surface. Examination of the wear debris and worn specimens by X-ray diffraction, and subsurface studies by tapered sections show that under these conditions of high strains, metallurgical phase transformations occur in the subsurface regions of both Brico 65 and 21 - 4N. It is the nature of these phase transformed materials which determines the

subsequent wear behaviour during the equilibrium wear regime. An extremely hard compact material, which can be interpreted as body centred cubic martensite, is found to be present in the subsurface of 21 - 4N. The material present in the subsurface of Brico 65 has a structure which is austenitic in form, however, this structure is less compact and is of lower hardness than the former. The difference in strength and hardness of these materials therefore accounts for the abrasive wear of the pin during the equilibrium wear regime. The abrasive wear rates appear to depend on the amount of silicon which is transferred to the disc material, which in turn, is temperature dependent. The wear rates are approximately an order of magnitude greater for the wear tests at a disc temperature of 200°C at loads above the transition, in comparison to the purely frictionally heated experiments at the same sliding speed of 2 m/s, for loads above the transition. In the latter experiments the disc temperature was about 85°C.

In the case of friction, the friction coefficient (μ) is found to lie in the fairly narrow range $.25 \leqq \mu \leqq .7$ for all sliding conditions. For the non-externally heated wear tests, there is reduced friction at the higher sliding speeds, due to the increasing rate of oxidation. At elevated temperatures the variation of μ with disc temperature is insignificant, although there are two distinct equilibrium wear mechanisms.

An important feature borne out by the present study is the correlation between wear and heat flow. In particular, the similarities between the variations of wear rate and bulk surface temperature (T_s) with load. Sharp increases in wear rate are always accompanied by sharp increases in T_s. This is due to the change in

surface conductance which accompanies any change in wear regime. In addition, theoretical considerations show that the temperature of sliding contact (T_o) is load dependent, in a similar manner to T_s. The average contact radius is found to be approximately constant and the number of contacting asperities increases linearly with load, for a given wear regime. However, both are speed dependent.

The use of experimental and theoretically deduced surface parameters in Quinn's oxidational wear equation indicate that the oxidation constants A_p and Q_p in a tribological situation may both be different from such constants in the case of static oxidation. In particular, Q_p is found to be significantly lower in the former case. In the case of tribo-oxidation substantial 'short circuit' diffusion along grain boundaries and disloaction lines may occur. This would account for the lower activation energies. The main advantage of the method developed to deduce tribological values of A_p and Q_p is that it can be used for any sliding material combination of pin-on-disc geometry.

In conclusion, simple pin-on-disc wear experiments (allied with heat flow measurements) have provided a useful assessment of the wear behaviour of Brico 65 and 21 - 4N over a wide range of sliding conditions. It is clear to the author that the natural extension of this study is to investigate the effect of different oxidizing environments on the wear behaviour of these materials.

APPENDIX 1

Evaluation of τ_{max} for a Hollow Circular Shaft in Pure Shear.

Timoshenko (34) shows that the total resisting torque (T) about the axis of a circular shaft is given by the expression

$$T = G\theta \int_A r^2 \, dA = G\theta J \quad \ldots (1a)$$

where $J = \int_A r^2 dA$ is defined as the polar moment of inertia of the circular section, G is the shear modulus of the shaft material and is the angle of twist per unit length of the shaft. The element of area dA is given by $dA = r dr d\alpha$ where

$$\frac{d_i}{2} \leq r \leq \frac{d_o}{2} \quad \text{and} \quad 0 \leq \alpha \leq 2$$

where d_i and d_o are the internal and external shaft diameters respectively. Hence

$$J = \int_A r^2 \, dA = \int_0^2 \int_{\frac{d_i}{2}}^{d_o/2} r^2 \, r \, dr \, d\alpha$$

$$= \left\{ \int_0^{2\pi} d\alpha \right\} \left\{ \int_{d_i/2}^{d_o/2} r^3 dr \right\} = 2\pi \left[r^4/4 \right]_{d_i/2}^{d_o/2}$$

$$J = \frac{\pi}{32} (d_o^4 - d_i^4) \quad \ldots (1b)$$

Substituting in (1a) :

$$T = \frac{\pi}{32} G\theta \, (d_o^4 - d_i^4) \quad \ldots (1c)$$

or $$\theta = \frac{32T}{\pi G (d_o^4 - d_i^4)}$$

The maximum shear stress is given by [34]

$$\tau_{max} = Gr_o\theta = G\frac{d_o}{2}\theta$$

$$\tau_{max} = \frac{16T\, d_o}{\pi(d_o^4 - d_i^4)} \qquad \ldots(1d)$$

APPENDIX 2

Evaluation of σ_x for a Hollow Circular Shaft subjected to pure Bending.

Timoshenko (34) shows that in the case of pure bending the normal stress (σ_x) is given by

$$\sigma_x = \frac{My}{I} \qquad \ldots(2a)$$

where M is the bending moment, y is the distance of an element from the neutral axis and $I = \int_A y2\ dA$ is the moment of inertia of the cross-section with respect to the neutral axis. The element of area dA is given by

$$dA = r\ dr\ d\theta$$

where $\frac{d_i}{2} \leqq r \leqq \frac{d_o}{2}$ and $0 \leqq \theta \leqq 2\pi$ are plane polar co-ordinates. Hence $y = r \sin\theta$

$$\therefore I = \int_0^{2\pi} \int_{\frac{d_i}{2}}^{\frac{d_o}{2}} r^2 \sin^2\theta\ r\ dr\ d\theta$$

$$= \left\{ \int_0^{2\pi} \sin^2\theta\ d\theta \right\} \left\{ \int_{d_i/2}^{d_o/2} r^3 dr \right\}$$

$$= \left\{ \int_0^{2\pi} \tfrac{1}{2}(1 - \cos 2\theta)\ d\theta \right\} \left\{ \int_{d_i/2}^{d_o/2} r^3 dr \right\}$$

$$= \frac{\pi}{4} \left\{ \left(\frac{d_o}{2}\right)^4 - \left(\frac{d_i}{2}\right)^4 \right\}$$

$$\therefore I = \frac{\pi}{64}(d_o^4 - d_i^4) \quad \ldots (2c)$$

From equation (2a) the maximum bending stress is

$$\sigma_{max} = \frac{M}{I} y_{max} = \frac{Md_o}{2I} \quad \ldots (2d)$$

Substituting for I from (2c)

$$\sigma_{max} = \frac{32\ Md_o}{\pi(d_o^4 - d_i^4)} \quad \ldots . (2e)$$

APPENDIX 3

Maximum Temperature rise due to a Stationary Source in a Semi-infinite Solid.

The steady state temperature at the point (x,y,z) in the semi-infinite solid $z < 0$ with no flow of heat over the surface $z = o$, due to heat supplied at the rate q per unit time per unit area over the square $-1 < x < 1$, $-1 < y < 1$, $z < 0$ as given by Jaeger (27) is

$$\frac{q}{2\pi K} \int_{-1}^{1} \int_{-1}^{1} \left[(x - x^*)^2 + (y - y^*)^2 + z^2 \right]^{-\frac{1}{2}} dx^* dy^*$$

where K is the thermal conductivity and the product dx^*dy^* is an element of area of the source.

The maximum temperature occurs at the centre of the source (i.e. $x = y = z = 0$) (27) and is given by

$$\Delta T_{max} = \frac{q}{2\pi K} \int_{-1}^{1} \int_{-1}^{1} \left((x^*)^2 + (y^*)^2 \right)^{-\frac{1}{2}} dx^* dy^* \quad \ldots (3a)$$

For a circular source given by

$0 \leqq r^* \leqq 1$ and $0 \leqq \theta^* \leqq 2\pi$

$$(x^*)^2 + (y^*)^2 = (r^*)^2 \quad \ldots(3b)$$

$$\therefore \quad \Delta T_{max} = \frac{q}{2\pi K} \int_0^{2\pi} \int_0^1 \left((r^*)^2 \right)^{-\frac{1}{2}} r^* \, dr^* \, d\theta^*$$

$$\frac{q}{2\pi K} \int_0^{2\pi} \int_0^1 dr^* \, d\theta^* = \frac{q}{2\pi K} \left\{ \int_0^{2\pi} d\theta^* \right\} \times \left\{ \int_0^1 dr^* \right\}$$

$$\Delta T_{max} = \frac{q}{2\pi K} \times 2\pi 1 = \frac{ql}{K} \quad \ldots(3d)$$

For a pin-on-disc geometry of N circular asperity contacts of average radius 'a' the contact area is $N\pi a^2$. Hence if heat is supplied at a rate H_1 to the pin, the heat flux is $q = H_1/N\pi a^2$

$$\Delta T_{max} = \frac{H_1 a}{N\pi a^2 K} = \frac{H_1}{N\pi a K} \quad \ldots(3e)$$

This expression is equivalent to the second term in equation (5.11).

The above discussion assumes that there is no oxide film at the surface. If, in fact, there is an oxide film then the third term in (5.11) represents the temperature drop across such a film. The first term in the expression is simply the general surface temperature (T_s), below the surface irregularities. Hence the contact temperature is given by

$$T_o = T_s + \frac{H_1}{N\pi K a} + \frac{H_1 \xi}{N\pi K_o a} \quad \ldots(3f)$$

REFERENCES

1. CASE AWARD project description 1978.

2. Lobley G.R. A metallurgical examination of exhaust valve sinkage, Materials Lab. report (Perkins Engines Ltd) 1977.

3. Le J.M. The calculation of exhaust valve and seat temperature distribution, Research Engineering report (Perkings Engines Ltd) 1977.

4. Welsh N.C. The dry wear of steels, Parts I and II, Phil. Trans. Roy. Soc. (1965) A257, p31.

5. Welsh N.C. Frictional heating and its influence on the wear of steel, J. Appl. Phys. (1957) vol. 28, p960.

6. Wright K.H.K. The abrasive wear resistance of human dental tissues, Wear (1969) vol. 14 p263.

7. Archard J.F. Contact and rubbing of flat surfaces, J. Appl. Phys. (1953) vol. 24 p981.

8. Bowden F.P. and Tabor D. The friction and lubrication of solids, Parts I and II (1954), Clarendon Press, Oxford.

9. Archard J.F. and Hirst W. The wear of metals under unlubricated conditions, Proc. Roy. Soc. (1956) A236. p397.

10. Burwell J.T. and Strang C.D. Metallic wear, Proc. Roy. Soc. (1952) vol. 212 p470.

11. Burwell J.T. Survey of possible wear mechanisms, Wear (1957) vol. 1, p119.

12. Rabinowicz E. The friction and wear of materials (1965) John Wiley and Sons, New York.

13. Quinn T.F.J. The classifications, laws, mechanisms and theories of wear; Fundamentals of Tribology (1980) MIT Press, Cambridge, Massachusetts, p447.

14. Stott F.H., Lin D.S. and Wood G.C. The structure and mechanism of formation of the "glaze" oxide layers produced on nickel-based alloys during wear at high temperatures, Corr, Sci. (1973) vol.13 p449.

15. Tabor D. The hardness of metals (1951), Oxford University Press.

16. Dokos S.J. Sliding friction under extreme pressures, J. Appl. Mech. (1946) vol.13 A148.

17. Rabinowicz E. Direction of the friction force, Nature (1957) vol. 179, p1073.

18. Rigney D.A. and Hirth J.P. Plastic deformation and sliding friction of metals, Wear (1979) vol.53, p345.

19. Archard J.F. Single contacts and multiple encounters, J. Appl. Phys. (1961) vol.32, p1420.

20. Quinn T.F.J. Oxidational wear, Wear (1971) vol. 18, p418.

21. Suh N.P. The delamination theory of wear, Wear (1973) vol.25,p111.

22. Rigney D.A. and Glaeser W.A. The significance of near surface microstructure in the wear process, Wear (1978) vol.46, p241.

23. Engel P.A. Impact wear of materials (1978), New York. Elsevier Scientific Pub. Co

24. Archard J.F. The temperature of rubbing surfaces, Wear (1959) vol.2, p438.

25. Quinn T.F.J. The effect of hot-spot temperatures on the unlubricated wear of steel, Trans ASLE (1967) vol. 10, p158.

26. Blok H. Theoretical study of temperature rise of surfaces of actual contact under oiliness lubricating conditions, Inst. Mech. Eng. (General discussion on lubrication) (1937) vol.2, p222.

27. Jaeger J.C. Moving sources of heat and the temperature at sliding contacts, Proc. Roy. Soc. N.S.W. (1942) vol.56, p203.

28. Shore H. Thermoelectric measurement of cutting tool temperature, J. Wash, Acad. Sci. vol.15 (1925), p85.

29. Herbert E.G. The measurement of cutting temperatures, Proc. Inst. Mech. Engrs. (1926) vol.1 p289.

30. Furey M.J. Surface temperatures in sliding contact, ASLE Trans. (1964) vol.7, p133.

31. Rowson D.M. and Quinn T.F.J. Frictional heating and the oxidational theory of wear, J. Appl. Phys. D (1980) vol.13 p209.

32. Fenner catalogues on power transmission.

33. Shigley J. Mechanical engineering design, MacGraw Hill, 3rd Ed. (1977).

34. Timoshenko S. and Young D.H. Elements of strength of materials, Van Nostrand Co. Inc. (1968).

35. Timken catalogues on tapered roller bearings.

36. Enots catalogues on pneumatic valves and cylinders.

37. Cobb E.C. and Saunders O.A. Heat transfer from a rotating disc, Proc, Roy. Soc. (1956) A236, p343.

38. Sankaran S. and Rabinowicz E. Effect of the rate of repeat traversal on adhesive wear, Wear (1979) vol. 56, p227.

39. Quinn T.F.J. X-rays, electrons and crystalline materials, Butterworths (1968), London.

40. Quinn T.F.J. The application of modern physical techniques to tribology, Butterworths (1971), London.

41. Isherwood B.J. and Quinn T.F.J. The application of glancing angle X-ray diffraction to the study of low temperature oxidation of iron chromium alloys, Brit. J. Appl. Phys. (1967) vol.18, p717.

42. Francis J.M. The relationship between lattice parameter and chemical constitution of spinel oxide phases formed during the oxidation of austenitic steels, J. Appl. Chem. (1966) vol.16, p264.

43. A.S.T.M. index to the powder diffraction file (1963).

44. A.S.T.M. powder diffraction data file.

45. Dumbleton J.H. and Douthett J.A. The unlubricated adhesive wear resistance of metastable austenitic stainless steels containing silicon, Wear (1977) vol.42, p305.

46. Allen P.M. Temper items - Types 201, 301, 304 and 300, Armco Steel Corporation, Ohio (1968).

47. Funke P. et. al. The influence of austenite stability on the behaviour of stainless chromium-nickel steels during cold working, DEW Dtsch. Edelstablwerke Tech. Ber. (1969) vol.9,p370.

48. Butakova E.D. et. al. Influence of chromium and nickel on the mechanical properties of martensitic transformation of Fe-Ni-Cr alloys during deformation, Fiz. Met. Metalloved (1971) 31 (3).p574.

49. Tamura I. et.al. Strength and ductility of austenitic iron alloys accompanying strain-induced martensitic transformation, ASM 2nd. Int. Conf. on the strength of metals and alloys, Pacific Grove, California (1970).

50. Quinn T.F.J. The application of X-ray diffraction techniques to the study of wear, Advances in X-ray analysis (1967) vol.10,p310, Plenun Press New York.

51. Grosberg P. and Molgaard J. Aspects of the wear of spinning travellers: the division of heat at rubbing surfaces, Proc.Inst. Mech. Engrs. (1966/67) vol.181. Pt 3L. p16.

52. Quinn T.F.J. The division of heat and surface temperatures at sliding steel interfaces and their relation to oxidational wear, Trans. ASLE (1978) vol. 21, p78.

53. Quinn T.F.J. An experimental study of the thermal aspects of sliding contacts and their relation to the unlubricated wear of steel, Prox. Inst. Mech. Engrs. (1978/69) vol.183, Pt3P, p129.

54. Quinn T.F.J. et. al. Application of the oxidational theory of mild wear to the sliding wear of low alloy steel, Wear (1980) vol.65 p1.

55. Quinn T.F.J. et.al. Developments in the oxidational theory of mild wear, Tribology International (1980) 13(4), p153.

56. Quinn T.F.J. and Sullivan J.L. A review of oxidational wear, Proc. ASME Conf. on wear of materials (1977) p110. St. Louis U.S.A.

57. Holm R. Calculation of the temperature development in a contact heated in the contact surface, and application to the problem of of the temperature rise in a sliding contact, J. Appl. Phys. (1945) vol.19, p361.

58. Holm R. Temperature development in a heated contact with application to sliding contacts, J. Appl. Mech. (1952) vol.19 p369.

59. Molgaard J. and Smeltzer W.W. Thermal conductivity of magnetite and hematite, J. Appl. Phys. (1971) vol.42, p3644.

60. ASM Committee on engine valves, Metals handbook vol.1, p326.

61. Chemical Rubber Co., Handbook of chemistry and physics, 44th Ed.

62. Davies M.H. et.al. Oxidation of high purity iron in dry oxygen, Ibid (1951) vol.3, p889.

63. Caplan D. and Cohen M. The effect of cold work on the oxidation of iron from 100 to 650^{o}C, Corr. Sci (1966) vol.6 p321.

64. Oudar J. Physics and Chemistry of surfaces, Blackie (1975).

65. Athwal S.S. Private communication (1981/82).

66. Stott F.H. and Wood G.C. The influence of oxides in the friction and wear of alloys, Tribology International (1978) vol.11, p221.

67. Kubaschewski O. and Hopkins B.E. Oxidation of metals and alloys, Butterworths (1953), London.

68. Svedung I. and Vannerberg N.G. The influence of silicon on the oxidation properties of iron, Corr.Sci. (1974) vol.14, p391.

69. Wulf G.L. et.al. Theoretical analysis of alloy oxidation with reference to Fe-Cr alloys, Corr.Sci. (1969) vol.9, p739.

70. Taylor D.E. et.al. The fretting wear of an austenitic stainless steel in air and CO_2 at elevated temperatures, Wear (1979) vol.56, p9.

71. Aronov V. Formation and destruction kinetics of transformed structures of metals in friction, Wear (1976) vol.38, p305.

72. Aronov V. Kinetic characteristics of the transformation and failure of the surface layers of metals under dry friction, Wear (1977) vol.41, p205.

73. Eyre T.S. and Maynard D. Surface aspects of unlubricated metal-to-metal wear, Wear (1971) vol.18,p301.

74. Wilson J.E. et.al. The development of wear-protective oxides and their influence on sliding friction, Proc.Roy. Soc. (1980) A369, p557.

75. Saka N. et.al. Wear of metals at high sliding speeds, Wear (1977) vol.44, p109.

76. Childs T.H.C. The sliding wear mechanisms of metals, mainly steels, Tribology International (1980). Vol. 13, P285.

77. Krause H. Tribochemical reactions in the friction and wearing process of iron, Wear (1971) vol.18, p403.

78. Tao F.F. A study of oxidation phenomena in corrosive wear, Trans. ASLE (1969) vol.12, p97.

79. Molgaard J. A discussion of oxidation, oxide thickness and oxide transfer in wear , Wear (1976),vol.40,p277.

80. Guy A.G. and Hren J.J. Elements of physical metallurgy, Addison-Wesley (1974). Reading, Massachusetts U.S.A.

81. Kofstad P. High temperature oxidation of metals, Wiley and Sons (1966) New York.

82. Smeltzer W.W. et.al. Oxidation of metals by short circuits and lattice diffusion of oxygen, Act. Met. (1961) vol.9, p880.

83. Hart E.W. The role of dislocations in bulk diffusion, Act. Met. (1957) vol.5, p597.

84. Markali J. 5th Int. Congr. Electron Microscopy Academic Press New York (1962).